Université de Strasbourg

École Doctorale de Sciences Chimiques – ED222

Institut de Science et d'Ingénierie Supramoléculaires (ISIS) – UMR 7006

Thèse

présentée par **Guido MASELLA**

sostenue le 6 décembre 2019

pour obtenir le grade de: **Docteur de l'Université de Strasbourg**

Discipline/Spécialité: **Physique**

Exotic Quantum Phenomena in Cold Atomic Gases

Numerical Approaches

THÈSE dirigée par:

Pr. PUPILLO Guido	Professeur, Université de Strasbourg

RAPPORTEURS:

Pr. ERCOLESSI Elisa	Professeur, Università di Bologna
Pr. SCARDICCHIO Antonello	Professeur, Abdus Salam ICTP

AUTRES MEMBRES DU JURY:

Dr. GENET Cyriaque	Directeur de Recherche, ISIS

This page would be intentionally left blank if we would not wish to inform about that.

Université de Strasbourg

EDSC École Doctorale des Sciences Chimiques

Guido Masella

Exotic Quantum Phenomena in Cold Atomic Gases

Résumé L'objectif principal de cette thèse est l'étude des propriétés à basse énergie et température de systèmes fortement corrélés de bosons interagissant via des potentiels à portée longue et étendue, et pertinentes pour la réalisation expérimentale avec des gaz atomiques froids. Cette étude est réalisée à l'aide d'une combinaison de techniques numériques, comme le Path Integral Montecarlo et de techniques analytiques. Le principal résultat de mon travail est la démonstration de l'existence d'une phase supersolide à bandes et d'une rare transition entre différents supersolides dans un modèle à interaction finie de bosons de coer dur sur un réseau carré. J'étudie également les scénarios hors d'équilibre de tels modèles via des quenches de température simulées. Enfin, j'étudie comment la restauration de l'extensibilité énergétique dans des systèmes en interaction à longue portée peut avoir une incidence profonde sur les propriétés de basse énergie dans la limite thermodynamique.

Mots clés: Systèmes à N corps quantiques, Physique de la matière condensée Atomes froids, Mèthodes numériques, Supersolidité, Interactions à longue portée, Quantum Monte Carlo

Abstract The central aim of this thesis is the study of the low-energy and low-temperature properties of strongly correlated systems of bosonic particles interacting via finite- and long-range potentials, and relevant to experimental realization with cold atomic gases. This study is carried out with a combination of state-of-the-art numerical techniques such as Path Integral Monte Carlo and analytical techniques. The main result of my work is the demonstration of the existence of a stripe supersolid phase and of a rare transition between isotropic and anisotropic supersolids in a finite-range interacting model of hard-bosons on a square lattice. I also investigate the out-of-equilibrium scenarios of such models via simulated temperature quenches. Finally, I investigate how restoring energy extensivity in long-range interacting systems can have a profound incidence on the low-energy properties in the thermodynamic limit.

Keywords: Quantum Many-Body Systems, Condensed Matter Physics, Numerical Methods, Supersolids, Long-Range Interactions, Quantum Monte Carlo

"With magic, you can turn a frog into a prince. With science, you can turn a frog into a Ph.D and you still have the frog you started with."

— Terry Pratchett, Science of Discoworld

To my mother Maria Teresa and my father Sergio. I could not have wished for anything better than the teachings you gave me. Thanks for always supporting me all these years.
To my grandfathers Guido and Giuseppe.

Acknowledgements

Foremost, I would like to express my sincere gratitude to my Ph. D. advisor, Prof. Guido Pupillo for the continuous support of my Ph. D. study and research, for his motivation, enthusiasm, and immense knowledge.
Besides by advisor, I would like to thank the rest of my thesis committee: Prof. Elisa Ercolessi, Prof. Alessandro Scardicchio and Dr. Cyriaque Genet.
My sincere thanks also goes to Dr. David Hagenmuller for his encouragement, insightful comments and his immense patience in reading the first drafts of this manuscript.
A special thanks goes also to Thomas Botzung for having shared with me not only the immense amount of bureaucracy during the doctorate, but above all passion and frustration for numerical algorithms and for the study of long-range interacting systems.
I thank my fellow colleagues of the Quantum Matter Theory group here in Strasbourg: Dr. Andreas Geissler, Dr. Johannes Schachenmayer, Dr. Stefan Shultz, Dr. Nora Sándor, and David Wellnitz.
I am grateful to Prof. Nikolay Prokof'ev for the enlightening discussions during his time visiting Strasbourg and during the writing of part of this work.
Another special mention goes to Dr. Fabio Mezzacapo and Dr. Adriano Angelone for the useful teachings and support at the start of my Ph. D. but also for all the effort and work they put in our collaborations.
Last but not the least I would like to thank my family: my parents Sergio and Maria Teresa for giving me birth at the first place and for supporting me throughout my life. I would be never grateful enough for all the love and support my grandfather Guido gave me. I express my thanks to my sister

Claudia and my brother Jacopo Pio for the special relationship we have, for the moments of fun and all their support.
I also would like to thank my friends in the University of Strasbourg: Sayali, David, Rogéria, Federico and Renata for making Strasbourg a place worth living in.
Finally thank you Filipa. Thank you for the keen interest in seeing this work completed successfully and on time. Thank you for being there for me, for the moments of happiness together, for your immense patience and invaluable support. You are special to me.

Résumé de la Thése en Fraçais

Introduction

Au cours des deux dernières décennies, les gaz atomiques froids se sont révélés être un cadre utile pour l'exploration d'une riche variété de propriétés et de phénomènes quantiques à plusieurs corps [1]. Grâce au développement des technologies laser et à la compréhension profonde des interactions atome-lumière, il est aujourd'hui possible de concevoir des expériences avec des atomes confinés sur des réseaux optiques et de manipuler les interactions interatomiques avec un niveau d'accordabilité sans précédent [2]. Ces caractéristiques font des systèmes atomiques froids les meilleurs candidats pour réaliser un *simulateur quantique*, c'est-à-dire un système conçu pour simuler le comportement des Hamiltoniens de systèmes fortement corrélés de matiére condensée. Suite à ces progrès remarquables, la compréhension théorique de problèmes difficiles en physique de la matière condensée a été renforcée avec une nouvelle génération de théories et d'idées orientées vers la perspective de faciliter la compréhension des données expérimentales (autant que possible), et de fournir un guide utile pour le développement futur de la technologie des simulateurs quantiques.

Poussé par ces avancées et en particulier par des expériences avec des atomes ayant des fortes interactions magnétiques, des molécules polaires, des atomes excités dans des états de Rydberg, des ions et des atomes neutres couplés à des modes photoniques, l'étude des effets des interactions à longue distance sur les phases quantiques des systèmes à plusieurs corps est devenu un sujet populaire de recherche.

En raison du manque de solutions analytiques et des difficultés à traiter

même numériquement le grand nombre de degrés de liberté, ces systèmes présentent des défis théoriques majeurs qui peuvent être partiellement résolus en utilisant des méthodes numériques de pointe. Pour l'étude des systèmes quantiques à plusieurs corps de bosons non frustrés, les méthodes de Monte Carlo quantique (Quantum Monte Carlo) (QMC) [3], et en particulier les méthodes Monte Carlo de intégrale de chemin (path integral Monte Carlo) (PIMC) [4] avec les *updates* du "*Worm*" [5], fournissent un outil très puissant et polyvalent permettant, en principe, d'effectuer des simulations numériquement exactes. D'autre part, les algorithmes de density matrix renormalization group (DMRG) [6] peuvent fournir une précision sans précédent pour les simulations numériques de bosons et de fermions limités à des systèmes unidimensionnels. Cependant, les interactions à longue portée représentent un défi majeur dans les deux cas car elles peuvent générer une prolifération d'états à faible énergie, dont le nombre augmente de manière exponentielle avec la taille du système, ce qui entraîne généralement des problèmes essentiellement insolubles (par exemple dans le cas de structures dites "escalier du diable").

Ici, en nous appuyant sur ces méthodes autant que possible, nous présentons une étude de phénomènes quantiques exotiques dans des modèles ayant un intérêt direct pour des expériences avec des gaz atomiques froids. La *supersolidité*, c'est-à-dire la coexistence de la *superfluidité* et d'une structure cristalline, est un exemple frappant (voir par exemple [7]). Cette phase exotique et insaisissable a été prédite dans une pléthore de modèles théoriques mais n'a jamais été observée expérimentalement à l'équilibre (une observation récente d'une phase supersolide métastable est donnée dans [8]). Il est donc primordial d'étudier plus en detail cette phase dans des systèmes présentant un intérêt direct pour les réalisations expérimentales.

Résultats et discussions

Dans la première partie de ce travail, après une brève introduction des concepts de *superfluidité* et de *supersolidité*, nous discutons la mise en œuvre originale de l'algorithme "Worm", une technique numérique PIMC idéale pour simuler des modèles de particules bosoniques non frustrées sur un ré-

seau. La méthode standard d'intégrale de chemin permet de ramener un problème quantique à d dimensions à un problème classique à $d+1$ dimensions (la dimension ajoutée étant le *temps imaginaire*). Les moyennes thermodynamiques d'observables physiques pertinentes sont obtenues en calculant la moyenne sur toutes les configurations possibles du système généré via les méthodes de la chaine de Markov Monte Carlo. Nous discutons ici de l'efficacité de notre implémentation dans le cas de modèles avec interactions aux sauts à longue portée, et nous montrons comment l'estimation des observables cruciales pour la compréhension de ce modèle (c'est-à-dire la densité superfluide [9]) est affectée par rapport au cas des modèles à courte portée.

Dans une seconde partie de cette thèse, nous étudions un modèle de Bose-Hubbard étendu de particules bosoniques confinées sur un réseau bidimensionnel et interagissant via un interaction repoussante à portée étendue (extended-range repulsive interactions (ERI). Les interactions de ce type présentent un intérêt immédiat pour les expériences utilisant des atomes habillés de Rydberg ; à des densités suffisamment élevées, les ERI sont caractérisés par la mise en amas, qui est une caractéristique liée à la supersolidité dans un espace continu bidimensionnel, et à la supersolidité et (super)vitrosité sur un réseau triangulaire [10]. Dans le modèle étudié dans cette thèse, les particules interagissent jusqu'à une distance $r_c = 2\sqrt{2}$ Par souci de simplicité, nous nous référerons à ce modèle en tant que Modèle I. Dans ce modèle, une particule peut sauter entre des sites voisins avec une amplitude t tout en satisfaisant la contrainte de cœur dur (une seule particule est autorisée sur chaque site).

La démonstration du comportement des bandes dans les condensats de Bose-Einstein en présence de couplage spin-orbite a récemment suscité un vif intérêt, mais également la formation de gouttelettes dans les nuages d'atomes magnétiques dipolaires en raison de la concurrence des fluctuations quantiques et des interactions à courte et longue portée. Des résultats numériques exacts ont en outre démontré théoriquement que des interactions dipolaires anisotropes pour des particules confinées en deux dimensions peuvent générer des bandes tout en préservant la superfluidité [11, 12], ce qui correspond à une réalisation possible de la supersolidité sous la forme de bandes [13, 7].

Cette dernière a une longue histoire en matière condensée, où elle a été introduite pour la première fois en tant que phase dite de *superstripe*. En effet, les structures métalliques non homogènes présentant une symétrie spatiale brisée semblaient alors favoriser la supraconductivité [14]. Bien que l'origine microscopique d'une telle phase fasse encore l'objet de débats, il est clair qu'un rôle important est joué par la combinaison des interactions fortes et du potentiel du réseau. Dans ce contexte, les principaux défis à relever consistent à proposer et à comprendre les mécanismes sous-jacents à la formation de (super)bandes dans les géométries de réseau présentant un intérêt expérimental, et à faire des prédictions théoriques exactes dans le régime des interactions fortes. Nous étudions ici les phases de l'état fondamental (EF) du modèle I en fonction de la force d'interaction V/t. Nous trouvons plusieurs nouveaux phénomènes. Pour des interactions suffisamment fortes, l'EF est un cristal à bandes (stripe crystal) (SC) isolant hautement anisotrope, émergeant de l'auto assemblage en amas dans l'EF classique correspondant. Pour une force d'interaction intermédiaire, nous trouvons une transition de phase quantique inattendue d'un état supersolide à un autre état supersolide, séparant un état supersolide isotrope (isotropic supersolid) (IS) d'un état supersolide anisotrope à bande (anisotropic stripe supersolid) (SS). Dans cet état, la superfluidité se produit principalement le long de bandes horizontales, tandis que l'ordre diagonal à grande distance se trouve dans la direction perpendiculaire - ce qui rappelle la phase dite *superstripe* trouvée dans les supraconducteurs sur réseau [14].

Nous étudions aussi systématiquement les scénarios hors d'équilibre (HE) du Modèle I. Au moyen de la même approche de PIMC, nous déséquilibrons le système avec des "quench" simulés à basse température (T), et nous analysons les modifications que cette procédure peut induire sur les phases d'équilibre calculées. Nos principales conclusions sont les suivantes : i) Contrairement aux supersolides isotropes et anisotropes trouvés pour $2.6 \lesssim V/t \lesssim 4.0$ et $4.0 \lesssim V/t \lesssim 4.45$ respectivement, un "quench" à basse température conduit à des états supersolides largement isotropes pour $3.8 \lesssim V/t \lesssim 4.2$, ainsi q'un état solide normal HE pour $lesssim V/t \lesssim 5.5$. Remarquablement, ces états HE

Fig. 1. : Diagramme de phase schématique du modèle I en fonction de la force d'interaction V/t. Chaque région colorée dans la partie inférieure de la figure correspond à une phase d'équilibre de EF : à savoir, un superfluide (superfluide (SF), cyan), un supersolide isotrope (IS, orange), un supersolide à bandes (SS, vert) et un cristal à bandes (SC, rose). Les dessins sont des croquis de la structure cristalline (le cas échéant) de chaque phase à l'équilibre. Les schémas de remplissage dans la partie supérieure du diagramme montrent les résultats dans la limite thermodynamique des "quench" de température simulées jusqu'à la température cible $T/t = 1/20$. Les régions où le "quench" conduit à des états supersolides, solides et vitreux sont désignées par des motifs de remplissage horizontaux, diagonaux ou en points.

sont également trouvés pour les valeurs de V/t pour lesquelles les phases à l'équilibre sont plutôt anisotropes. ii) De la même manière qu'une étude précédente du même modèle quantique sur le réseau triangulaire [10] (bien qu'elle soit plus petite que r_c), nous trouvons que la contrepartie HE du cristal à l'équilibre à grand V/t est un verre normal, et non un verre superfluide ou un *superglass*. iii) Dans la plage de paramètres étudiés, aucune preuve de comportement de *superglass* n'est obtenue. L'existence d'un tel état, qui a été prédite pour le réseau triangulaire, dépend essentiellement de l'interaction entre la géométrie du réseau, la densité de particules, et l'extension r_c de la partie plate du potentiel inter-particules.

Dans certains cas, des techniques numériques telles que celles introduites dans ce travail permettent, au prix d'une énorme puissance de calcul, de résoudre de façon "brute-force" les modèles à longue portée. Dans la dernière partie de ce travail, nous montrons des exemples de ces systèmes. Nous considérons tout d'abord un modèle de bosons de cœur dur sur un réseau unidimensionnel avec des interactions se comportant en loi de puissance en fonction de la distance r entre deux particules $\sim 1/r^{\alpha}$ (Modèle II). Nous montrons en particulier comment les propriétés de ces systèmes sont radicalement modifiées lors de l'application de la "prescription de Kac" [15], qui restaure l'extensivité de l'énergie du système. En l'absence de cette prescription, les calculs numériques effectués avec la méthode DMRG nous ont permis d'étendre

la conclusion précédente de la Ref. [16] dans le cas $\alpha = 1$ pour l'ensemble de ce qu'on appelle le régime des *fortes* interactions à longue portée $(0 < \alpha \leq 1)$.

Conclusion générale

Dans cette thèse, nous prédisons et étudions de nombreux phénomènes et phases exotiques apparaissant dans différents modèles de systèmes à plusieurs corps fortement corrélés. Nous mettons en lumière des états supersolides anisotropes et des transitions de phase quantiques entre différents types de supersolides dans un modèle de Bose-Hubbard étendu avec les ERI. Nous explorons les états HE du même modèle en soulignant les différences entre ces phases et les phases d'EF. Dans un modèle unidimensionnel de bosons de cœur dur avec des interactions à longue portée, nous discutons des différents scénarios physiques obtenus en appliquant ou non la "prescription de Kac" [15] dans le cas du régime des fortes interactions à longue-portée, tout en étudiant la validité de la théorie des liquides de Luttinger dans les deux cas. Pour tous les modèles étudiés, nous discutons les réalisations expérimentales possibles, et en particulier les expériences mettant en jeu des gaz atomiques froids et des atomes de Rydberg.

Contents

Preface

I started working as a Ph. D. student in the group of Prof. Guido Pupillo almost three years ago, in February 2017. During this period I have investigated different physical problems in many-body systems with long--range interactions including supersolidity and superfluidity in lattice bosonic models, Rydberg atoms, ultracold neutral plasmas and finally many-body localization. In particular I've utilized advanced numerical techniques such as Quantum Monte Carlo methods and Path Integral Monte Carlo methods working on different implementations of the so-called *worm* algorithm in the canonical ensemble. Together with Dr. Adriano Angelone I've also worked on refining an existing grand canonical implementation of the same algorithm. This implementation of the algorithm was used to derive most of the results presented in Chapters 1 and 2 in collaboration with also Prof. Nikolay V. Prokof'ev and Dr. Fabio Mezzacapo. I also implemented and used different exact or approximate numerical techniques including *exact diagonalization* and *density matrix renormalization group* methods.

In the following I detail my contribution to the different publications I have authored and co-authored during my Ph. D.

- G. Masella, A. Angelone, F. Mezzacapo, G. Pupillo, and N. V. Prokof'ev. "Supersolid Stripe Crystal from Finite-Range Interactions on a Lattice". In: *Phys. Rev. Lett.* 123.4 (July 26, 2019), p. 045301. DOI: 10.1103/PhysRevLett.123.045301. As first author I was responsible of all the numerical simulations, and results presented in this paper, in its supplemental material and in Chapter 1 . I contributed extensively to the writing of the published paper.

- A. Angelone, T. Ying, F. Mezzacapo, G. Masella, M. Dalmonte, and G. Pupillo. "Non-Equilibrium Scenarios in Cluster-Forming Quantum Lattice Models". Submitted to: *Phys. Rev.A* (2019). arXiv: 1606.04267. In this work I contributed extensively to the numerical simulations in collaboration with Dr. Angelone, and also to discussion and writing of the cited paper. Results are reported in Chapter 2 .

- T. Botzung, D. Hagenmüller, G. Masella, J. Dubail, N. Defenu, A. Trombettoni, and G. Pupillo. "Effects of Energy Extensivity on the Quantum Phases of Long-Range Interacting Systems". Submitted to: *Phys. Rev. Lett.* (2019). arXiv: 1909.12105. My contribution to this work, which is presented in Chapter 3 and Appendix B , consists of a preliminary Quantum Monte Carlo study of the correlation functions the long-rage interacting system presented. This study brought to light the first questions about (non-)extensivity and the problem of defining the thermodynamic limit for the model. Answers to these questions are provided in the paper using by Thomas Botzung and Dr. David Hagenmüller using different techniques. I have also contributed to discussion and writing of the paper.

- M. Mizoguchi, Y. Zhang, M. Kunimi, A. Tanaka, S. Takeda, N. Takei, V. Bharti, K. Koyasu, T. Kishimoto, D. Jaksch, A. Glaetzle, M. Kiffner, G. Masella, G. Pupillo, M. Weidemüller, and K. Ohmori. "Ultrafast Creation of Overlapping Rydberg Electrons in an Atomic BEC and Mott-Insulator Lattice". Submitted to: *Science* (2019). arXiv: 1910.05292. This work, is an experimental study of the ionization processes in a system of ultracold atomic gases excited to Rydberg states. I contributed to the studies of the dynamics of the ionization in the case of the atomic system being initially in a Mott insulator state.

Introduction

The behavior of large and complex aggregations of elementary particles, it turns out, is not to be understood in terms of a simple extrapolation of the properties of a few particles. Instead, at each level of complexity entirely new properties appear, and the understanding of the new behaviors requires research which I think is as fundamental in its nature as any other

— P. W. Anderson [21]

Condensed matter physics is the study of systems of many particles in a *condensed* phase, i.e. solid or liquid. At low temperature the physics of many particle systems is governed by quantum mechanics, and macroscopic properties can in principle all be derived from the solutions of the Schrödinger equation. However, solving Schrödinger equation exactly usually turns out to be an intractable task. Even a classical computer made by all of the atoms in our universe would not be powerful enough to handle the solutions of the Schrödinger equation for the typically large number of particles in condensed matter systems ($\sim 10^{23}$). And even if such an exact solution were available, it would be extremely complex to understand how it determines the macroscopic behaviour and in particular the *emergent phenomena* of such large collection of particles. For these reasons the study of many-body systems often relies in practice on incomplete and approximate numerical and theoretical descriptions, in order to extract the macroscopic properties.

At sufficiently high temperatures, matter is in a gaseous phase which is one of the simplest many-body systems. Gases are referred to as weakly correlated systems because the motion of an atom in a gas hardly depends on

the positions and motion of the other ones. For this reason one can in general describe the properties of gases in terms of single-particle theories. As the temperature is lowered, the motion of the atoms becomes more and more correlated and, eventually, they solidify into crystalline structure whose excitations, called *phonons*, correspond to the collective motion of many of them. A crystal is one of the simplest examples of strongly-correlated states. The formation of solids and crystalline structures is associated with the breaking of the continuous translational symmetry typical of free space. The resulting spatial modulation of the density $\rho(\mathbf{r})$ can be described as $\rho(\mathbf{r}) = \rho(\mathbf{r} + \mathbf{R})$ for any vector $\mathbf{R}$ of the *Bravais lattice*. The appearance of these periodic modulations, or *long-range diagonal order*, are also manifested in Fourier space by peaks in the static structure factor at the vectors $\mathbf{K}$ of the reciprocal lattice for which $\mathbf{K} \cdot \mathbf{R} = 2\pi n$ where n is an integer.

In the beginning of the 20th century, many new states of matter have been found thanks to the development of low-temperature technologies. An example is *superconductivity*, i.e. the loss of electrical resistance and the appearance of anomalous magnetic behaviours at very low temperature in metals. The basic theory of superconductivity is due to Bardeen, Cooper, and Schrieffer (BCS theory [22]), and explains most of the properties of this state in terms of a *superfluid*, which consists of a dissipation-free flow of electron pairs called *Cooper pairs*. As of today, the study of strongly-correlated matter remains a very active field of research.

Below we briefly introduce from an historical point of view the *superfluid* and *supersolid* state of matter which we encountered often during the studies presented in the remainder of this thesis.

Superfluidity is a rather general property of bosonic, interacting systems at low temperature. It was first discovered in ^{4}He in 1937 by Kapitsa in Moscow, and almost simultaneously by Allen and Misener in Cambridge[1]. At that time

[1]See Refs. [23, 24, 25] for in-depth reviews and books about superfluidity.

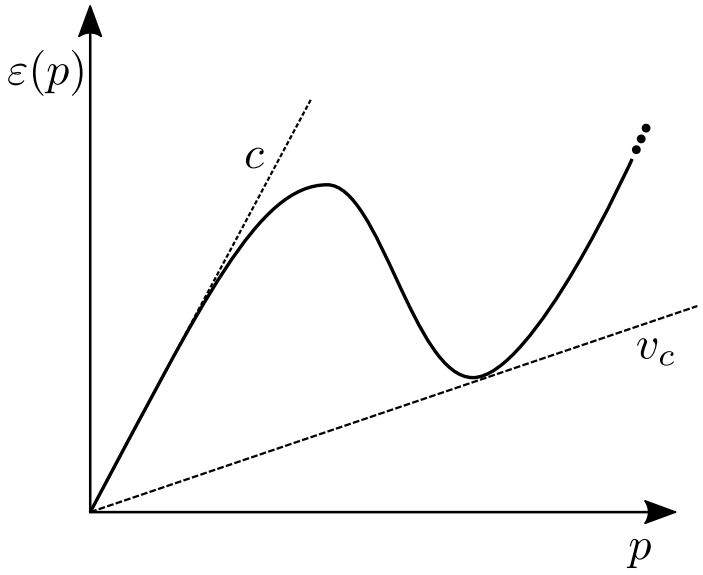

Figure 0.1.: Sketch of the excitation spectrum of ^{4}He showing the line $\epsilon(p) = v_c p$ (dashed) corresponding to limit velocity of a superfluid. Here $v_c = \min_p (\epsilon(p)/p)$.

Helium was known to liquefy at temperatures lower than 4 K and was discovered to undergo a phase transition if cooled below the so-called *λ-point* ($T_\lambda = 2.17\,\mathrm{K}$). Above the λ-point the fluid referred to as He-I behaves like a normal, viscous fluid. For temperatures below T_λ, in the phase referred to as He-II, the viscosity of the fluid drops to values experimentally compatible with zero. This property of matter can be characterized by a dissipation-free flow referred to as a *superflow*.

While the atoms or molecules in He-I move in a random manner as in normal classical liquids, they move coherently in He-II forming a *macroscopic* wave of matter. This idea is at the basis of the first theory of superfluidity introduced by Fritz London [26], who connected this phenomenon in ^{4}He (a bosonic isotope of Helium) to Bose-Einstein condensation, a phenomenon which consists in the macroscopic occupation of a single (single-particle-like) state.

The modern understanding of superfluidity stems from Landau's theory of the *two fluids*. In this theory superfluids are constituted of two separate fluids: *normal component*, which is made of *quasiparticles*, namely *phonons*, *rotons*, and a *superfluid component*. The superfluid component carries no entropy and moves without dissipation while the normal one is viscous and carries a non-zero entropy. One of the first achievements of this theory is the prediction of the excitation spectrum showed schematically in Fig. 0.1. It comes from two different contributions, one linear, due to phonons, and another quadratic due to rotons[2]. In the framework of Landau's *two fluids* theory, the emergence of superfluidity can be understood by considering an object moving at a velocity v inside the superfluid. The only way such an object can lose energy to the fluid is by exciting some collective modes but, thanks to the peculiar form of the spectrum, there exists a limit velocity v_c up to which no modes can be excited (see Fig. 0.1). For this reason such object can propagate inside the fluid without dissipation [27].

Considering a slowly rotating bucket filled with ^{4}He, another prediction of Landau's theory is that only the normal part of the fluid is allowed to rotate while the superfluid part stays at rest. This prediction has been later confirmed by Andronikashvili by using a torsional oscillator [28] which allowed him to determine the two fluid fractions by measuring the change in the moment of inertia across the transition point.

A useful concept to further describe the onset of superfluidity in three-dimensional systems is the concept of *off-diagonal long-range order*, originally introduced by Oliver Penrose. Off-diagonal long-range order is associated to the spontaneous symmetry breaking of the gauge invariance symmetry ($U(1)$) associated to the emergence of a macroscopic wave function, and to the macroscopic occupation of the single-particle ground state called Bose-Einstein condensation [29, 24].

More precisely, one can consider the one particle density matrix defined as $\rho_1(\mathbf{r}-\mathbf{r}') \equiv \left\langle \hat{\psi}^\dagger(\mathbf{r})\hat{\psi}(\mathbf{r}') \right\rangle$ where $\hat{\psi}^\dagger$ and $\hat{\psi}^\dagger$ are the field operators for bosonic

[2] the exact form of the roton excitation spectrum was given by Feynman and Cohen

particles. Its Fourier transform is the momentum distribution $n_{\mathbf{k}} \equiv \left\langle \hat{\psi}(\mathbf{k})^{\dagger} \hat{\psi}(\mathbf{k}) \right\rangle$ where $\hat{\psi}(\mathbf{k})^{\dagger}$ and $\hat{\psi}(\mathbf{k})$ create and annihilate a bosonic particle with momentum $\mathbf{k}$.

In a Bose-Einstein condensate, one state, e.g., $\mathbf{k} = 0$, becomes macroscopically occupied so that $n_{\mathbf{k}} = N_0 \delta(\mathbf{k}) + f(\mathbf{k})$ where N_0 is of the order of the total number (N) of particles in the system and f is a smooth function of $\mathbf{k}$. In terms of the one-body density matrix, this condition implies that $\lim_{|\mathbf{r}-\mathbf{r}'|\to\infty} \rho_1(\mathbf{r}-\mathbf{r}') = \frac{N_0}{\mathcal{V}}$ with $\mathcal{V}$ the total volume of the system. This is the formal definition of *off-diagonal long-range order*.

It is worth mentioning that although the relation between Bose-Einstein condensation and superfluidity is straightforward in three-dimensions, in general one never equates to nor even entails the other. In ^{4}He, e.g., the condensed fraction, i.e., N_0/N, is $\sim 10\%$ while the superfluid fraction approaches unity as the temperature approaches the absolute zero. The possibility of having superfluidity without condensation is dramatically demonstrated in two dimensional systems at finite temperature where Bose-Einstein condensation is replaced by quasi off-diagonal long-range order[1].

As the name *supersolid* or *superfluid solid* suggests, a supersolid phase is a "paradoxical" state of matter which displays both the features of a solid and of a superfluid. Having a correct picture of the coexistence of these two phases is difficult. Counterintuitively, supersolids allow dissipation-free flow of their own constituents but not of external objects, and act in this regard as *normal* solids. Formally a supersolid is defined by the coexistence of diagonal and off-diagonal long-range orders. While superfluid phases have been observed and identified in different systems comprising, e.g., ^{4} He and ultracold atomic systems, supersolids have remained elusive for over 50 years and have been observed only recently in dipolar quantum gases.

The search for supersolid phases started in *1969*, with the theoretical predictions of Andreev and Lifshitz, and Chester [30, 31]. The proposed mech-

anism for the formation of a supersolid consisted in the Bose-Einstein condensation and therefore superfluidity of a *repulsively* interacting gas of point defects in solids, i.e. vacancies and dislocations. These proposals were also based on the fact that point defects, which may be present in the ground state of quantum many-body systems (e.g. ^{4}He), were predicted to have a high mobility at low temperature.

Following the proposal of Andreev and Lifshitz, and Chester, the experimental investigation focused on solid ^{4}He, the most quantum solid in nature.

Inspired by the experiments of Goodkind [32], in 2004 Kim and Chan performed an experiment which provided a controversial evidence of supersolidity in ^{4}He[33, 34]. In this experiment [33] the idea was to use a torsional oscillator similar to the one used in 1948 to measure the rotational inertia of superfluid Helium [28]. At temperatures $T < 200\,\mathrm{mK}$, Kim and Chan observed a rapid change of the torsional oscillator period, and connected it to a change in the moment of inertia of solid ^{4}He (a part of it was not moving anymore with the rest). They estimated the superfluid component to be $\sim 1\%$.

The experiment performed by Kim and Chan at the Pennsylvania State University raised more questions than answers: was the observed drop in the period of the torsional oscillator due to a change of the moment of inertia, and ultimately to superflow inside the solid helium, or it was due to some other effect?

In the years following the experiment of Kim and Chan, numerical simulation based on unbiased quantum Monte Carlo methods [35, 36, 37, 38] proved that a *perfect* crystal of ^{4}He, i.e. without vacancies and interstitials, could not support a supersolid phase due to the absence of off-diagonal long-range order. Moreover it was shown [39] that, due to both the finite energy gaps for the formation of vacancies and interstitials, and to the prediction of strongly attractive (not repulsive) interactions among the vacancies, the mechanism of Andreev and Lifshitz was unlikely to be relevant for perfect ^{4}He crystals.

After the theoretical predictions ruling out supersolidity in ^{4}He, and the observation [40] of the change of the shear modulus in bulk solid ^{4}He, an effect that could have explained their previous observations, Kim and Chan

reported [41] in 2012 about a new and improved version of their original experiment. Here they didn't observe any change in the moment of inertia which could suggest the presence of superflow inside solid ^{4}He.

If solid ^{4}He is not an answer to the search for supersolidity, in what other places one should look at?

Since the first realization in 1995 of a Bose-Einstein condensate [42] which was awarded by a Nobel prize in 2001 [43], ultracold quantum gases have proven to be a unique framework for the exploration of a rich variety of many-body quantum phenomena. Quantum gases are very dilute system however their properties and behaviours are governed almost exclusively by the interactions. Thanks to the recent impressive scientific and technological advances is this field, it is nowadays possible to engineer systems with different and tunable interactions. The short-range quasi contact-like interactions usually occurring in these systems can be tuned and controlled taking advantage of the so-called Fano-Feshbach resonances[3]. Furthermore dipolar interactions [48] can be engineered in systems with strongly interacting magnetic atoms [49, 50, 51, 52, 53], polar molecules [54, 55], Rydberg-excited atoms [56, 57] or light-induced dipoles [58, 59, 60].

Interesting alternatives to dipole-dipole interactions are the unscreened Coulomb interaction appearing in systems of trapped ions [61, 62, 63, 64], the natural long-range interactions between neutral atoms coupled to photonic modes [65, 66, 67, 68, 69, 70] and the extended range interactions of Rydberg-dressed atoms [71, 72, 73, 74, 75].

Driven by the availability of such versatile platforms, new mechanisms for the formation of the supersolid phase have been proposed as alternatives to the Andreev-Lifschitz one. In the case of system with dipolar interactions in free space, while the mechanism for the stabilization of the supersolid phase

[3] see [44] or Refs. [45, 46, 47] for the case of optical (Rydberg) Feshbach resonances

has been identified[4] no unbiased numerical prediction is, as of today, available. For dipolar systems of particles confined on optical lattices numerical proofs of the existence of the supersolid phase have been produced [83, 84, 85].

Moreover, systems interacting via soft-shoulder extended range potentials, e.g., Rydberg-dressed atoms[5], have been predicted to support supersolidity in two dimensional systems in free space [71, 86, 87, 88], on a triangular lattice [89, 10] and finally, as shown in the results presented in Chapter 1 , on a square lattice.

Recently, supersolidity has been experimentally observed in degenerate quantum gases exploiting spin-orbit coupling[90], cavity-mediated long-range interactions [91], in 2017 while this year (2019) three new experiments with strongly magnetic atoms of Dysprosium and Erbium[6] reported observations of supersolidity [92, 8, 93, 94].

Outline of the results

The central aim of this thesis is the study of the low-energy and low-temperature properties of strongly-correlated systems of bosonic particles interacting via finite- and long-range potentials.

In Chapters 1 and 2 I present the results for a model of strongly correlated hardcore bosons on a two dimensional square lattice, interacting via a finite-range potential mimicking the Rydberg-dressed interaction on a lattice. The main goal of the study presented in Chapters 1 and 2 is to study the equilibrium phases and the out-of-equilibrium states such model for a particular choice of the interaction radius which will allow to show how complexity

[4] See [76, 77] for reviews, [78, 79] regarding the prediction of the present of roton-like spectrum in dipolar systems, [80, 81, 82] for numerical study of the roton instability and the formation of droplets.

[5] See Appendix C for the detailed description.

[6] Dysprosium (Dy) and Erbium (Er) are respectively the second and the third most magnetic atomic species known, thanks to the magnetic moment in the ground state being $10\mu_B$ for Dy and $9\mu_B$ for Er, where μ_B is the Bohr magneton.

arise in the phase diagram due to the inclusion in the hamiltonian of features typical of long-range interacting systems.

In Chapter 1 , I present the study of the ground state (equilibrium) phase diagram finding: (i) For sufficiently strong interactions, the ground state is a highly anisotropic, insulating stripe crystal. For intermediate interaction strength I find a surprising (ii) supersolid-supersolid quantum phase transition separating an isotropic supersolid state from (iii) a highly anisotropic one. In the latter, superfluidity occurs only along one direction while diagonal long-range order is found in the perpendicular one. I address this phase to as *superstripe* phase due to the analogies with a similar phase found in lattice-based superconductor [14].

In Chapter 2 , I present the investigation of the out-of-equilibrium scenarios of the same model presented in Chapter 1 via simulated temperature quenches. I find that (iv), as opposed to the isotropic and anisotropic supersolid ground states of the equilibrium study, low-temperature quenches leads to isotropic out-of-equilibrium solid and supersolid states. (v) Similar to a previous study performed on a triangular lattice [10], the out-of-equilibrium counterpart of the equilibrium crystal at large interaction strengths is a normal glass. (vi) In contrast to [10], no evidence of a superglass (i.e., coexistence of glassy and superfluid behaviour) is found.

In Chapter 3 , I show the results concerning a study of a truly long-range interacting model which consists of hard-core bosonic particles on a one-dimensional lattice-ring geometry with L sites interacting via interactions which algebraically decay with the distance r, e.g., as $1/r^{\alpha}$) This study is performed in the so called *strong* long-range regime occurring when $\alpha \leq d$ (here $d = 1$). One can show that this model feature non-extensive energy. Extensivity can be restored by the so called Kac's prescription. The main goal is to understand how the properties of long-range interacting systems are modified when energy extensivity is restored. We find that (vii) in the absence of Kac's rescaling, the ground state consists of an insulating gapped phase for the whole range $0 < \alpha \leq 1$. In stark contrast with this results we find (viii) that Kac's rescaling leads to a metallic phase for the same values of the exponent α, and

(ix) we demonstrate that this phase is incompatible with a conventional Luttinger Liquid.

1

Supersolid stripe crystal from finite-range interactions on a lattice

The effects of long-range interactions on quantum phases of many-body lattice systems is a hot topic of research [95, 96, 97, 48, 77], which is driven by outstanding advances in precision experiments with strongly interacting magnetic atoms [49, 50, 51, 52, 53], polar molecules [54, 55], Rydberg-excited atoms [56, 57], ions [61, 62, 63, 64], and neutral atoms coupled to photonic modes [65, 66, 67, 68, 98, 70]. For bosonic particles, exact numerical results from quantum Monte-Carlo methods can in principle predict thermodynamic properties of any unfrustrated model, where frustration is defined as the impossibility of simultaneously satisfying a minimum energy condition for all the term of the Hamiltonian. However, long-range interactions in combination with confinement to periodic potentials present a unique challenge as they generate a proliferation of metastable low-energy states, whose number exponentially increases with the system size [99, 100], even in the absence of external frustration. This usually results in, e.g., devil's staircase-type structures that are essentially intractable [101, 102, 83, 84].

Much interest was recently generated by the demonstration of stripe behavior in spin-orbit-coupled Bose-Einstein condensates [103, 104, 105, 106,

90] as well as droplet formation in clouds of dipolar magnetic atoms in the mean-field regime [107, 108, 109], due to a competition of quantum fluctuations, short- and long-range interactions [108, 110, 80]. Exact numerical results have further demonstrated theoretically that anisotropic dipolar interactions for particles confined to two dimensions (2D) can generate stripe behavior while preserving superfluidity [11, 12], corresponding to a possible realization of so-called stripe supersolidity [13, 7]. The latter has a long history in quantum condensed matter, where it was first introduced as *superstripe* phase, in that non-homogeneous metallic structures with broken spatial symmetry were found to favor superconductivity [14]. While the microscopic origin of such a phase is still a subject of debate, it is clear that a key role is played by a combination of strong interactions and the lattice potential. In this context, key open challenges are to propose and understand basic mechanisms for (super)stripe formation on lattice geometries of experimental interest and to provide exact theoretical predictions in the regime of strong interactions.

This chapter is devoted to showing the complexity that emerges within long-range interacting systems by studying simple and numerically tractable model, which features many of the ingredients of a generic long-range model. We will do this by studing the low temperature phase diagram of an ensemble of bosonic particles confined to a square lattice geometry and interacting via a finite-range potential, interpolating between nearest-neighbors and long-range physics. In §1.1, we introduce the model and the methods used, shortly commenting on the construction of the ground state in the classical limit, defined as the limit of vanishing tunnelling amplitude with respect to all the other couplings in the system. In §1.2, we utilize exact quantum Monte Carlo simulation to study the phase diagram of this system as a function of the interaction strength, and identifying several novel features: (i) For sufficiently strong interactions, the quantum ground state is a highly anisotropic, insulating stripe crystal that emerges due to cluster self-assembling in the corresponding classical ground state. For intermediate interaction strength, we find a surprising (ii) supersolid-supersolid quantum phase transition that separates an isotropic supersolid state from (iii) a highly anisotropic stripe

state. In the latter, superfluidity mostly occurs along horizontal (vertical) stripes and is not suppressed at the supersolid-supersolid transition, while diagonal long-range order is found in the perpendicular direction – reminescent of the so-called *superstripe* phase found in lattice-based superconductors [14]. §1.2.2 contains a brief discussion on the numerical complexity arising in these model that can be seen in increased difficulty to obtain reilable equilibration of the Monte Carlo simulations due to proliferation of low-energy metastable states as the range of the interaction increases. The effects of variations in density and interaction range on the many body phases found in §1.2 will be discussed in §1.3. In particular, for a choice of density $\rho = 1/6$, we demonstrate the existence of a stripe crystal for large values of interaction strength, and of a quantum phase transition from an isotropic supersolid to a homogeneous supersolid. We conclude the chapter with some final remarks and outlooks in §1.4.

1.1 Model, methods and clusters in the classical limit

We consider the following extended Hubbard Hamiltonian for bosonic particles confined to a two-dimensional square lattice.

$$\mathcal{H} = -t \sum_{\langle i,j \rangle} \left(b_i^\dagger b_j + \text{h.c.} \right) + V \sum_{i<j; r_{ij} \leq r_c} n_i n_j, \tag{1.1}$$

where the hard-core boson operators satisfy the commutation relation

$$\left[b_i, b_j^\dagger \right] = \delta_{ij} (1 - 2 b_i^\dagger b_i) \tag{1.2}$$

and the occupation number per site is restricted to $n_j = 0$ or 1, with $n_j = b_j^\dagger b_j$[1]. In the following the nearest-neighbor hopping energy t and the lattice spacing constant a are taken as units of energy and length, respectively. While the first term of Eq. (1.1) represents hopping of particles between nearest-neighbor pairs of sites (denoted by $\langle \cdots \rangle$) with amplitude t, the last term of

[1] The hard-core boson constraint and the commutation relation Eq. (1.2) can be also realized by treating the hard-core bosons as soft-core ones with infinite on site repulsion $U \sum_i \frac{n_i(n_i-1)}{2}$ with $U \to \infty$

represents the soft-shoulder interaction between bosons with strength V, r_{ij} is the distance between sites i and j, with r_c the interaction potential cutoff.

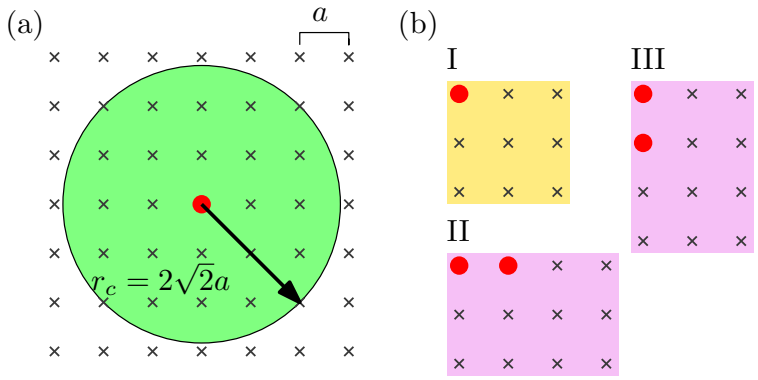

Figure 1.1.: Sketch of the interaction potential chosen in our work on a square lattice of spacing a [panel (a)]. The shaded region indicates the interaction range, which extends up to the critical radius $r_c = 2\sqrt{2}a$. In the large-V limit, the ground state of model Eq. (1.1) at our chosen density $\rho = 5/36$ can be found by tiling the lattice with clusters of type I, II and III [panel (a)]. Crosses and full red circles refer to empty and occupied lattice sites, respectively.

In classical physics, this interaction is of interest for soft-matter models of, e.g., colloids [111, 112, 113]. In quantum physics, similar interactions can be engineered in clouds of cold Rydberg atoms, by weakly-admixing a Rydberg state to the ground state using laser light [71, 72, 73, 87, 114, 74, 75]. Such interaction is described in detail in Appendix C .

Here, we choose $r_c = 2\sqrt{2}a$ for which in the classical limit $V/t \to \infty$ each particle tries to establish an avoided square region of total area $16a^2$ [see Fig. 1.1(a)]. For density $\rho = 1/9$ this is indeed possible and the system can arrange into an optimal configuration characterized by zero potential energy by covering the lattice with clusters of type I, see Fig. 1.1(b). However, this is not possible for higher densities, and the ground state shall be contructed as the solution of a tiling problem, where tiles are constituted by clusters of particles and holes that are effectively bound together by the repulsive interactions. The number of such clusters, or tiles, increases with increasing particle density. Fig. 1.1(b) shows the three clusters I, II, and III (i.e., the tiles) that appear at low energy for densities $1/9 < \rho < 1/6$. Similarly to the 1D case [115,

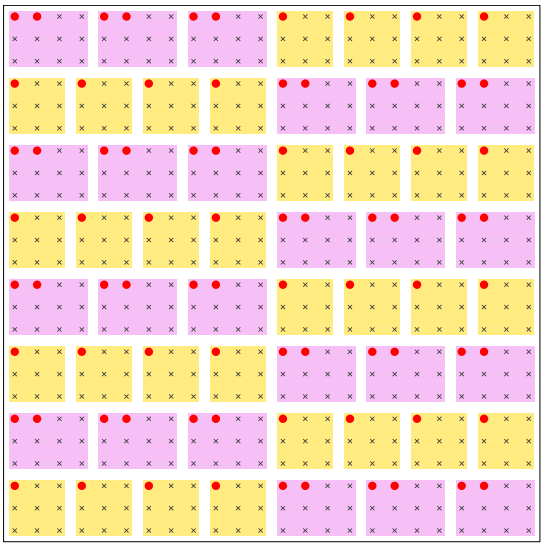

Figure 1.2.: Example of a single configuration of the ground state of the model Eq. (1.1) in the *classical* limit defined by $V/t \to \infty$. The configuration is obtained using only tiles of types I and II of Fig. 1.1 Crosses and full red circles refer to empty and occupied lattice sites, respectively.

116], the classical ground state can then be built from the exponentially large number of permutations of clusters I-III. This large degeneracy is characteristic of long-range interactions and can in principle constitute an obstacle to the solution of the quantum problem. In the following, we determine the effects of quantum fluctuations on this highly degenerate classical ground state by computing the quantum phase diagram for model Eq. (1.1), for an example density $\rho = 5/36$. Our focus is the determination of quantum phases and phase transitions in this system.

Figure 1.2 shows a single example configuration of the classical ground state obtained for the target density $\rho = 5/36$. This configuration results from the perfect tiling of the systems with cluster of types I and II and from the minimization of the energy $E = VN_{II}$, where N_{II} is he number of clusters of type *II*.

We study Hamiltonian Eq. (1.1) by means of path integral Quantum Monte Carlo simulations based on the worm algorithm [5]. This technique, presented in detail in Appendix A , is numerically exact for unfrustrated bosonic models, giving access to accurate estimates of fundamental observables such

as, e.g., the superfluid fraction ρ_s/ρ, the static structure factor $S(\mathbf{k})$ and the single-particle equal time Green's function $G(\mathbf{r})$, which can be written as:

$$\frac{\rho_s}{\rho} = \frac{1}{4t\beta\rho}\left\langle W_x^2 + W_y^2\right\rangle, \tag{1.3}$$

$$S(\mathbf{k}) = \frac{1}{N^2}\sum_{ij}\left\langle e^{-i\mathbf{k}\cdot\mathbf{r}_{ij}} n_i n_j\right\rangle, \tag{1.4}$$

$$G(\mathbf{r}) = \frac{1}{N}\left\langle \sum_i b_i^\dagger b_{i+\mathbf{r}}\right\rangle. \tag{1.5}$$

They measure superfluidity, diagonal long-range, and off-diagonal long-range orders, respectively. We recall that diagonal long-range order is associated with breaking of the discrete translational symmetry (e.g., crystallization) while off-diagonal long-range order to spontaneous breaking of the $U(1)$ or gauge symmetry (e.g., Bose-Einstein condensation). In Eq. (1.3), $\beta = 1/(k_B T)$ is the inverse temperature, with k_B the Boltzmann constant (set to unity); W_x (W_y) is the winding number along the x (y) direction, $\mathbf{k}$ is a lattice wave vector and $\langle \dots \rangle$ stands for statistical averaging. Calculations are performed on lattices of size $N = L \times L$, with L as large as $L = 96$ and temperatures as low as $T/t = 1/96$. We find that for $T/t \leq 1/20$ results are essentially indistinguishable from the extrapolated ground state ones.

1.2 Quantum phases: Results

The main results are presented in Figs. 1.3 and 1.4. Fig. 1.3(a) and Fig. 1.3(b) show estimates of the structure factor $S(\mathbf{k})$ and the superfluid fraction ρ_s/ρ (left ordinate axis) together with the ratio between the superfluid responses $\rho_x/\rho_y \equiv \left\langle W_x^2\right\rangle / \left\langle W_y^2\right\rangle$ along the horizontal and vertical directions (right ordinate axis) as a function of V/t, for $T/t = 1/20$ and $N = 96 \times 96$, respectively. Examples of finite-size scalings [Fig. 1.4] clarify that the chosen system size is large enough to provide an accurate description of the various observables in the thermodynamic limit, as results obtained for $L = 96$ essentially coincide with the extrapolated estimates. The combination of $S(\mathbf{k})$, ρ_s/ρ, and their anisotropies allows for the determination of the quantum phases.

We find that for weak interaction strengths $V/t \lesssim 2.6$ the ground state is a homogeneus superfluid (SF) with $\rho_s/\rho > 0$, $\rho_x \simeq \rho_y$, and $S(\mathbf{k}) = 0$. For

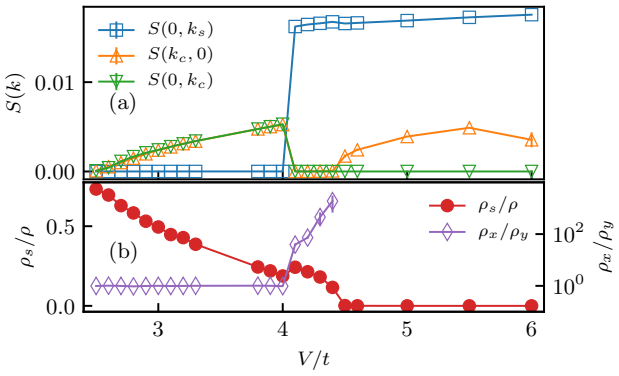

Figure 1.3.: Panel (a): Structure factor $S(\mathbf{k})$ as a function of V/t for values of lattice wave vector $\mathbf{k} = (k_c, 0)$ (up-pointing triangles), $(0, k_c)$ (down-pointing triangles), $(0, k_s)$ (squares) characteristic of the isotropic supersolid (IS), stripe crystal (SC), and anisotropic stripe supersolid (SS) ordered phase, respectively (see text). Here $k_c = 2\pi \times 7/24$ and $k_s = 2\pi \times 1/3$. Panel (b): Superfluid fraction ρ_s/ρ (circles), and ratio between the superfluid responses ρ_x/ρ_y along the x horizontal and y vertical axis (diamonds). Data is shown for $L = 96$ and $T/t = 1/20$.

$2.6 \lesssim V/t \lesssim 4.45$, however, both the superfluid fraction and the structure factor are finite, indicating the presence of a supersolid ground state. Surprisingly, in this range of interaction strength we find two distinct supersolids. Specifically, an isotropic supersolid (IS) and an anisotropic stripe supersolid (SS) occur for $2.6 \lesssim V/t \lesssim 4.0$ and $4.0 \lesssim V/t \lesssim 4.45$, respectively. Within the IS phase, $S(\mathbf{k})$ [Fig. 1.3(a)] takes its maximum value for $\mathbf{k} = (0, \pm k_c)$ and $(\pm k_c, 0)$ (down- and up-pointing triangles, respectively) with $k_c = 2\pi \times 7/24$; in IS the superfluid response is isotropic [Fig. 1.3(b), diamonds].

In contrast, in the SS phase the diagonal long-range order is found along one direction only (i.e., the y direction in the figure), being drastically suppressed along the perpendicular one; in addition, the maximum of the structure factor is found for $\mathbf{k} = (0, \pm k_s)$, with $k_s = 2\pi \times 1/3 \neq k_c$, while $S(0, \pm k_c) = S(\pm k_c, 0) = 0$ [Fig. 1.3(a), triangles]. Here, the superfluid response becomes strongly anisotropic with $\rho_x \gg \rho_y$, signalling the formation of superfluid stripes along the x-axis. This corresponds to a transition to a self-assembled array of essentially one-dimensional superfluids, which, unexpectedly, have larger superfluid density near the phase boundary: ρ_s/ρ initially increases

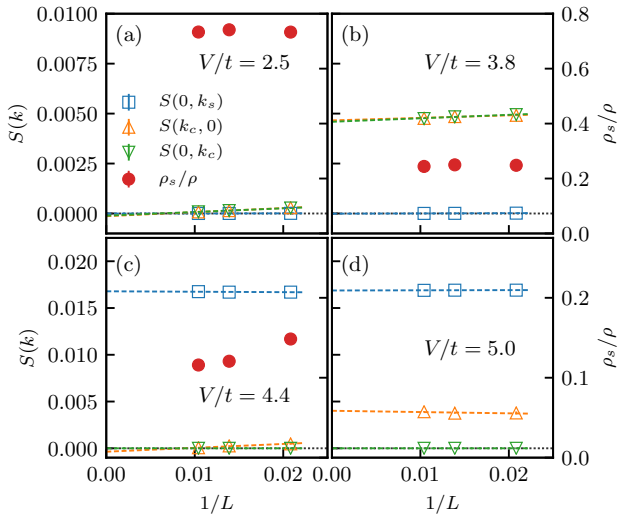

Figure 1.4.: Finite-size scaling of the structure factor $S(\mathbf{k})$ (empty symbols) and the superfluid fraction ρ_s/ρ (full circles) for $V/t = 2.5$ [panel (a)], $V/t = 3.7$ [panel (b)], 4.4 [panel (c)], and 5.0 [panel (d)]. Different empty symbols refer to $S(\mathbf{k})$ for values of lattice wave vector $\mathbf{k} = (k_c, 0)$ (up-pointing triangles), $(0, k_c)$ (down-pointing triangles), $(0, k_s)$ (squares) (see text). Data is whown for $T/t = 1/20$.

within the SS phase, before decreasing again, with increasing V/t.

Finally, for $V/t \gtrsim 4.45$ the system loses its superfluid character and, although the maximum value of $S(\mathbf{k})$ still occurs for $\mathbf{k} = (0, \pm k_s)$, secondary peaks emerge at $\mathbf{k} = (\pm k_c, 0)$. These latter peaks imply both crystallization along the stripe direction as well as the emergence of weak correlations between particles across different stripes (see below). The resulting ground state is a normal (non supefluid) crystal.

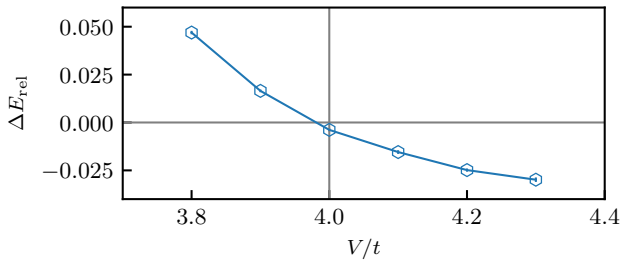

Figure 1.5.: Relative energy difference ΔE_{rel} between the SS and IS phases as a function of V/t. The SS has lower energy where ΔE_{rel} is negative. Data is shown for $L = 96$ and $T/t = 1/20$.

We find that different metastable states with entirely different quantum orders compete in the region of intermediate strengths of interactions $V/t \gtrsim 3.0$. In order to determine the ground state we perform two sets of simulations: namely, starting from the equilibrium configuration at $V_1/t = 3.7$ ($V_2/t = 5.0$) a careful annealing in the interaction strength is performed with annealing step $0 < \Delta V_1/t \leq 0.1$ ($-0.1 \leq \Delta V_2/t < 0$). When the desired target value of V/t is reached the calculation leading to a lower energy E is taken as the ground state. Figure 1.5 shows the relative energy difference $\Delta E_{rel} = (E_2 - E_1)/E_1$ as a function of V/t. The change in sign at $V/t \simeq 4.0$ signals the phase transition between the IS and SS phases. The corresponding sudden changes in crystalline order, measured by discontinuities of the structure factors in Fig. 1.3(a), are consistent with a first order phase transition between the two supersolids.

The formation of stripes remains favored for larger V/t: hence, the phase transition from the SS to the stripe crystal phase at $V/t \simeq 4.45$ is resolved by monitoring the vanishing of superfluidity fraction.

1.2.1 Phase diagram and Green's functions

The ground state phase diagram of model Eq. (1.1) is summarized in Fig. 1.6. The demonstration of the existence of novel superfluid and insulating stripe crystals, as well as an exotic supersolid-supersolid quantum phase transitions due to classical cluster formation in a rather general model with a simple isotropic interaction are the main results of this work. Further insight into the discussed ground states can be obtained from the density maps in Figs. 1.6(b) to 1.6(e) and the corresponding Green's function G_x (G_y) along the x (y) axis [Fig. 1.7].

As expected, for small V/t (where the system is a homogeneous SF) the average occupation number at each site equals the density ρ [Fig. 1.6(b)]. Similarly, the Green's functions are equal in the x and y directions at all distances (i.e., $G_x \simeq G_y$), within the statistical error bars. They become nearly flat at large distances, which is consistent with the presence of off-diagonal (quasi) long-range order [Fig. 1.7(a)]. We note that the algebraic rather than flat decay of the Green's function is consistent with the predicions of the Mermin-

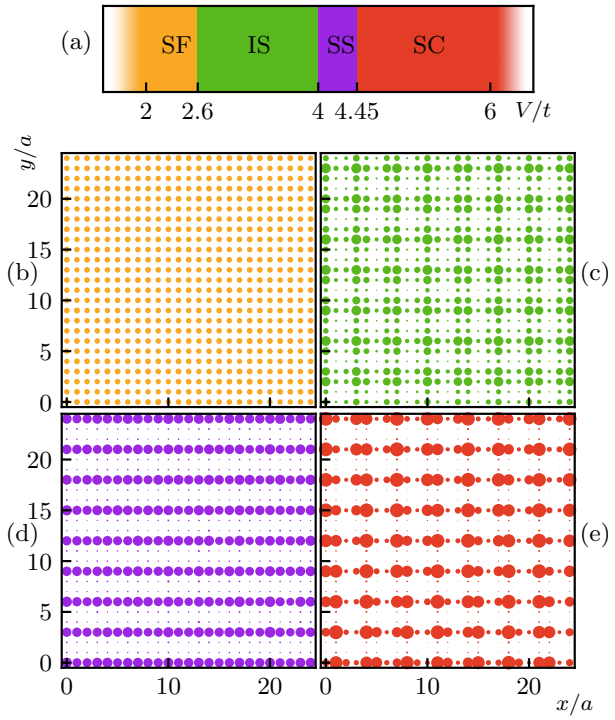

Figure 1.6.: Ground state phase diagram of model Eq. (1.1) as a function of the interaction strength V/t [Panel (a)]. For increasing values of V/t the ground state is a superfluid (SF), an IS, an SS and SC (see text). Panels (b), (c), (d), and (e) show site-density maps of a portion of the system for representative interaction strengths at which the ground state is a SF ($V/t = 2.5$), IS ($V/t = 3.7$), SS ($V/t = 4.3$), and SC ($V/t = 6.0$), respectively. The size of the dots is proportional to the occupation of the corresponding sites.

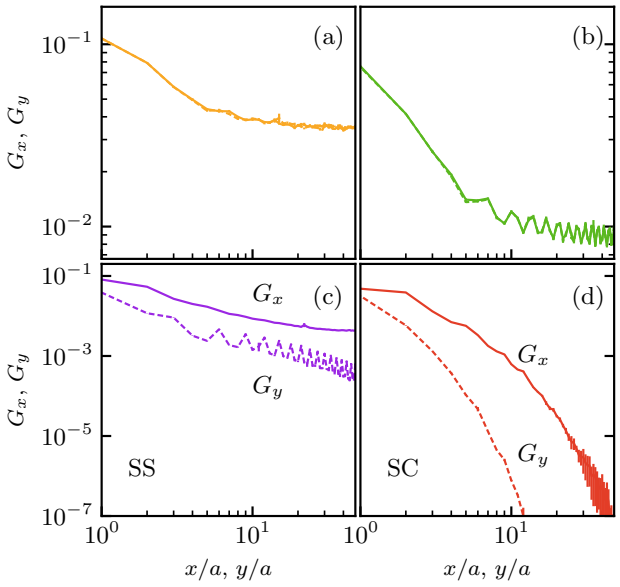

Figure 1.7.: Green's functions G_x and G_y along the x (solid lines) and y (dashed lines) directions, respectively, in the SF, IS, SS, and SC. Here $L = 96$, $T/t = 1/20$ and the values of V/t are the same as those in Figs. 1.6(b) to 1.6(e).

Wagner theorem which excludes the presence of true off-diagonal long-range order for a two-dimensional system at $T/t \neq 0$ [117, 118]. In the IS phase [Fig. 1.6(c)] the isotropic ordered structure formed by clusters of particles coexists with quantum exchanges and superfluidity. Here, $G_{x,y}$ displays a weak power-law decay, indicating off-diagonal quasi-long-range order, accompanied by oscillations [Fig. 1.7(b)], which we find to have a periodicity consistent with particle exchanges between different clusters, thus confirming the underlying classical structure. When stripes are formed in the SF phase, Fig. 1.6(d), no density modulations appear along their direction (i.e., the horizontal one). G_x is found to decay as a power-law [Fig. 1.7(c)], consistent with the measured finite superfluidity along the stripe direction. Long exchange cycles of identical particles take place almost exclusively along the stripes, being strongly suppressed in the perpendicular direction. The overall picture here is that of a 2D quantum system of quasi 1D superfluids (i.e. the stripes). In the SC phase the emergence of a nearly classical cluster-crystalline structure is evident [Fig. 1.6(e)]. Here long-range quantum exchanges are completely suppressed and clusters (and particles) can only slightly fluctu-

ate around their equilibrium position due to zero point motion, implying an exponential decay of the Green's functions in Fig. 1.7(d), albeit with different slopes in the x and y directions.

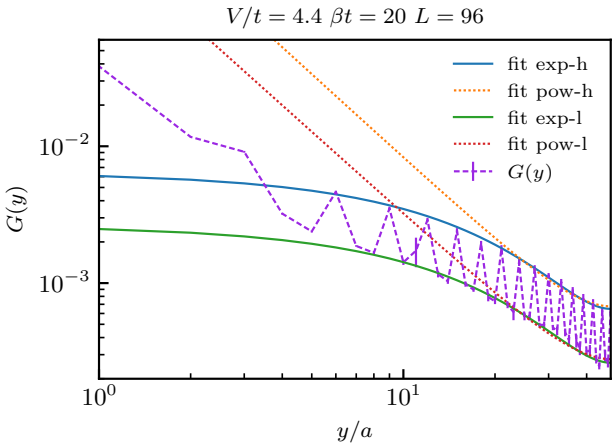

Figure 1.8.: Comparison of power-law (`pow`) and exponential (`exp`) fit of the Green's function $G_y \equiv G(0, r)$ in the SS phase for $V/t = 4.3$, $T/t = 1/20$ and $L = 96$. The fit is performed separately on the highest (`-h`) and lowest (`-l`) points of the oscillation.

In Fig. 1.8 we determine the long distance behavior of the Green's function G_y in the SS phases by fitting the it with exponentially and algebraically decaying function of the type:

$$\texttt{pow}: G_y(x) = \frac{b}{2}\left[\frac{1}{x^a} + \frac{1}{(L-x)^a}\right] \tag{1.6}$$

$$\texttt{exp}: G_y(x) = \frac{d}{2}\left[\exp\{-cx\} + \exp\{-c(L-x)\}\right] \tag{1.7}$$

The oscillations found in the Green's function plotted in Fig. 1.8 are due to the crystalline structure of the SS phase along the y-axis. In order to include the effect of the oscillations we fit two different datasets derived from the same Green's function data: one derived taking all the integer distances non multiple of 3 (lower points) and one taking all the points for which the integer distance r is multiple of 3 (higher points). The comparison of the reduced chi-squared (χ^2/dof where dof is the number of degrees of freedom of the fit) obtained by fitting the two different long-distance behaviors on the two different datasets available is shown in Table 1.1. It demonstrates an exponential decay that is dominant over the algebraic decay. In light of the results

summarized in Table 1.1 and in Fig. 1.8, given that the correlations between stripes decay exponentially with the distance, the SS phase can be described as an array of (quasi) one-dimensional superfluid stripes or tubes.

We find that the phases above are robust for density variations within the range $1/9 < \rho < 1/6$, where clusters I-III appear at low energy for large V/t. In §1.3 we demonstrate that they also persist for $\rho = 1/6$, where only clusters of type II and III exist for strong interactions, albeit with a different cluster periodicity (i.e. different k_c).

Function	Dataset	χ^2/dof (closer to 1 is better)
Exponential	High	0.91897
	Low	1.42404
Power-law	High	1.70635
	Low	2.38805

Table 1.1.: Reduced chi-squared (χ^2) for the exponential and power-law fits of Fig. 1.8. The exponential function used fits both dataframes better than the power-law function used.

1.2.2 Equilibration and metastable states

Finally, to exemplify possible out-of-equilibrium scenarios that can emerge with imperfect annealing (i.e., failure to equilibrate an annealing step or improper choice of the annealing step), Fig. 1.9 shows a density snapshot obtained when the system is driven away from equilibrium via a temperature quench. Here the target temperature is $T/t = 1/20$ for a value of V/t at which the equilibrium phase is a SS. The resulting snapshot is isotropic rather than anisotropic with a crystalline structure similar to Fig. 1.6(c), where diagonal long-range order is found for characteristic wave vectors $\mathbf{k} = (0, \pm k^*)$ and $(\pm k^*, 0)$ with $k^* \neq k_c, k_s$, and the value of ρ_s/ρ is much smaller than the equilibrium one.

Increasing r_c or smoothening the edges of the interactions can effectively result in the inclusion of more sites in the interaction volume. This can change

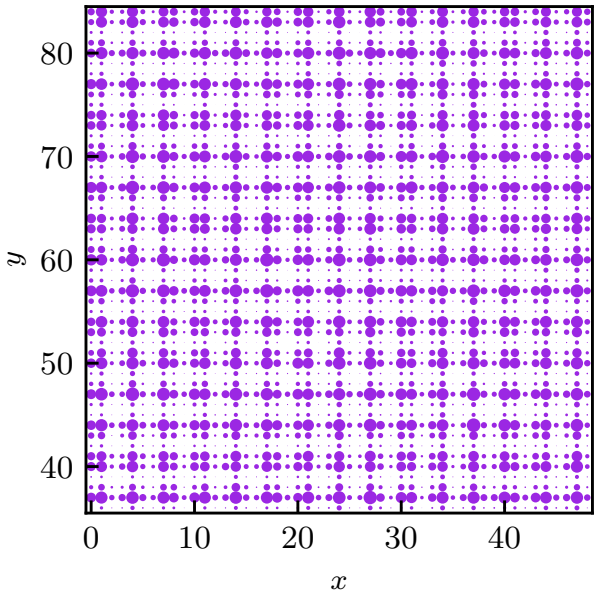

Figure 1.9.: Out-of-equilibrium density snapshot for a system with $L = 96$, $V/t = 4.1$ after a quench down to target temperature $T/t = 1/20$. For this choice of parameters the corresponding equilibrium phase is a SS. The size of the dots is proportional to the averaged occupation of the corresponding sites.

the number and type of clusters that appear at low-energy, and thus the resulting crystal structures. For example, for a larger $r_c = 3a$ and $\rho = 1/7$ the strong-coupling phase is a SC not oriented in the x or y-directions. In these cases, we find that annealing can become increasingly difficult as equilibration is often dominated by the presence of many metastable states, typical of long-range models [99, 100]. A detailed investigation of metastability for model Eq. (1.1) is presented in Chapter 2 .

1.3 Stability against density and potential shape variations

The numerical results presented in §1.2 are obtained for a specific choice of density $\rho = 5/36$ and for a soft-shoulder interaction potential with range $r_c = 2\sqrt{2}$. Below we show that the main quantum phases and phase transitions found in §1.2 are robust for density variations within the range $1/9 < \rho \leq 1/6$, where clusters of type II and III (in addition to type I) fully determine the

crystalline structure for large interaction strengths V/t, consistent with the discussion in §1.2. This is explicitly shown below for the limiting case $\rho = 1/6$.

Variations of Hamiltonian terms such as the interaction range r_c or shape can in principle lead to different crystalline phases at strong coupling (i.e. $V/t \gg 1$) with respect to the stripe crystal found before. Below we discuss the crystalline phases occurring by increasing r_c or by considering a smooth interaction potential instead of the step-like potential as the one already considered.

1.3.1 Quantum phases for density $\rho = 1/6$

The phases of Eq. (1.1) for $\rho = 5/36$ are representative of densities in the range $1/9 < \rho < 1/6$, where the clusters of type I, II and III in Fig. 1.1 dominate the dynamics for a large ratio V/t. Here, we investigate the case $\rho = 1/6$, corresponding to the smallest density increase for which the classical tiling problem has a different structure, as only the clusters of type II and III occur for large V/t. Calculations are performed for system sizes up to $N = 96 \times 96$ and temperatures as low as $T/t = 1/20$.

The main results are presented in Fig. 1.10, where, following the definitions found in §1.2, the structure factor $S(\mathbf{k})$ [Fig. 1.10(a)], the superfluid fraction ρ_s/ρ [Fig. 1.10(b) left ordinate axis], and the ratio between the superfluid responses ρ_x/ρ_y [Fig. 1.10(b) right ordinate axis] are plotted as a function of V/t, for $T/t = 1/20$ and $N = 96 \times 96$.

For large enough interaction strengths $V/t > 3.9$, we find a SC with no superfluidity, similar to the case treated in §1.2. However, the peaks in $S(\mathbf{k})$ occur here for $\mathbf{k} = (0, \pm k_s)$ and $\mathbf{k} = (k_{sc}, 0)$, with $k_s = 2\pi/3$ and $k_{sc} = 2\pi/4$, respectively. The crystalline order appearing on the x-axis is thus slightly different from that of the previously-found SC phase because $k_{sc} \neq k_c = 2\pi \times 7/24$.

Similarly to the case $\rho = 5/36$, by decreasing the interaction strength we first find an anisotropic stripe supersolid (SS) and then an isotropic supersolid (IS) phase. The latter phases occur for interaction strengths $3.0 \lesssim V/t \lesssim 3.9$ and $V/t \lesssim 3$, respectively. The peaks in the structure factor within the IS phase are at $\mathbf{k} = (\pm k_c, 0)$ and $\mathbf{k} = (0, \pm k_c)$, identical to the case $\rho = 5/36$

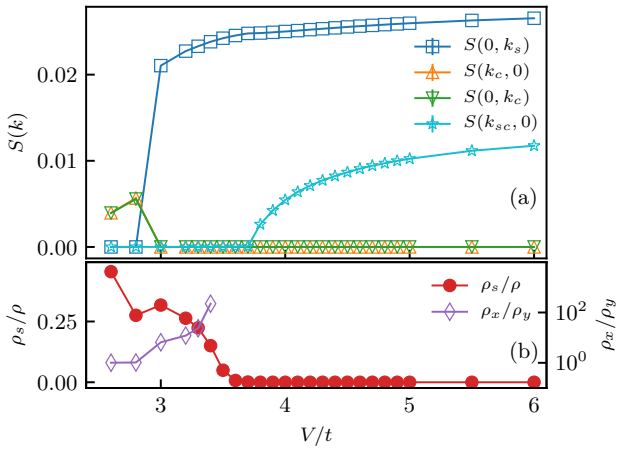

Figure 1.10.: Panel (a): Structure factor $S(\mathbf{k})$ as a function of V/t for values of lattice wave vector $\mathbf{k} = (k_c, 0)$ (up-pointing triangles), $(0, k_c)$ (down-pointing triangles), $(0, k_s)$ (squares), $(k_{sc}, 0)$ (stars) characteristic of the IS, SS, and SC ordered phase, respectively (see text). Here $k_c = 2\pi \times 7/24$ and $k_s = 2\pi \times 1/3$. Panel (b): Superfluid fraction ρ_s/ρ (circles), and ratio between the superfluid responses ρ_x/ρ_y along the x horizontal and y vertical axis (diamonds). Data taken from calculations with $N = 96 \times 96$, $\rho = 1/6$, and $T/t = 1/20$.

discussed in the §1.2.

Further insight can be obtained from the density maps in Fig. 1.11. In particular, Fig. 1.11(c) shows that for large V/t in the classical regime the ground state corresponds to a perfect crystalline tiling of the surface with just one single kind of clusters (i.e., cluster II in the $x-$direction in the figure). This results in a SC that is qualitatively similar to the one of §1.2, albeit with a slightly different periodicity in the x-direction, as discussed above. By decreasing V/t, a melting of this crystalline phase gives way to the SS and then IS phases.

In conclusion, we find that the main results discussed in §1.2, namely the appearance of an anisotropic (stripe) supersolid and a transition between two different supersolids (IS and SS), are robust against different choices of density in the range $1/9 < \rho \leq 1/6$, as long as the strong-coupling low-energy physics is dominated by clusters of the type II and III in Fig. 1.1, as expected. Further increasing densities with $\rho > 1/6$ introduces different kinds of clusters in the classical ground state that alter both the strong-coupling stripe

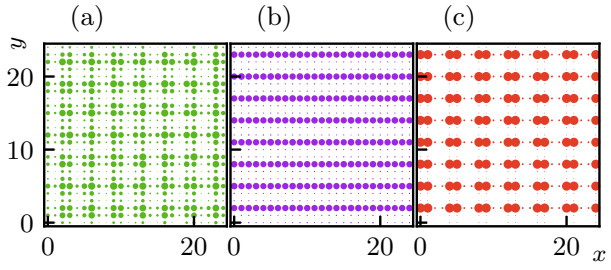

Figure 1.11.: Site-density maps of a portion of the system for representative interaction strengths at witch the ground state is a IS ($V/t = 2.8$) [panel (a)], SS ($V/t = 3.2$) [panel (b)], and SC ($V/t = 6.0$) [panel (a)]. The size of the dots is proportional to the occupation number of the corresponding lattice site. The data is taken from calculations at $T/t = 1/20$, $\rho = 1/6$, and $N = 96 \times 96$.

crystalline structure, and the ensuing supersolid phases for intermediate values of V/t. The corresponding quantum phases have then to be investigated on a case-by-case basis, for each density.

1.3.2 Effects of the interaction range and shape on the crystal phases of Eq. (1.1)

Varying the interaction range r_c in Eq. (1.1) can change the number and shape of relevant clusters in the large V/t limit. As a consequence, the many-body ground state can change from the predictions of §1.2. As an example, Fig. 1.12(b) shows a site-density map of a normal (not superfluid) crystalline phase appearing at $V/t = 6$ for a choice of interaction range $r_c = 3.0$ and density $\rho = 1/7$. The stripe crystal structure is now found to point in a diagonal direction. Further increasing r_c to large values $r_c/a \gg 1$ progressively reduces the stripe anisotropy, in favor of a triangular cluster crystal, similar to the continuous case [87].

Similar effects can be obtained by considering a smoother potential, instead of the stepwise potential of Eq. (1.1). As an example, Fig. 1.13 shows results for a potential of the type $V/[1 + (r/r_c)^\alpha]$, for different values of α and $V/t \gg 1$. For $\alpha \to \infty$ the shape of this interaction approximates well the one in Eq. (1.1). We find that for $\alpha \gtrsim 10$ stripe order is favoured along the x-direction (y-direction) for $V/t \gg 1$, similar to the discussion for Eq. (1.1).

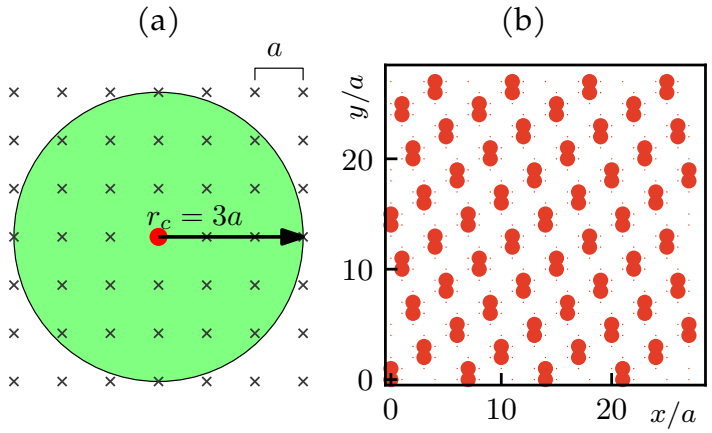

Figure 1.12.: Panel (a): Interaction volume corresponding to the model Eq. (1.1) with the cutoff radius of the interaction being $r_c = 3.0$. Panel (b): Side-density map of a system with $N = 28 \times 28$ showing a possible anisotropic crystalline structure forming for the choice $r_c = 3.0$. The size of the dots is proportional to the occupation number of the corresponding lattice site. The data is taken from calculations at $T/t = 1/20$ and $V/t = 6.0$ at the fixed density $\rho = 1/7$.

For $\alpha \lesssim 10$, however, the stripes progressively give way to a more isotropic, triangular crystalline structure. In particular, for $\alpha = 6$ (relevant for Rydberg-dressed atoms [74, 75]) the density map [Fig. 1.13(c)] and structure factor [Fig. 1.13(f)] indicate a triangular crystal structure that is essentially isotropic in the x and y directions. This can be qualitatively explained by considering that lower values of α effectively include more sites to the edges of the interaction volume for each particle, different from the case of §1.2. We note that for the case of smooth potentials as in Rydberg-dressed gases anisotropy can be re-introduced in the interactions by considering anisotropic Rydberg states (e.g., excited Rydberg p-type states instead of s states, as in [75, 119, 120]).

We find that strong metastable effects are often obtained in the numerical simulations for the situations discussed above in the intermediate regime of interactions $V/t \gtrsim 1$. The phase diagram thus has to be investigated on a case-by-case basis.

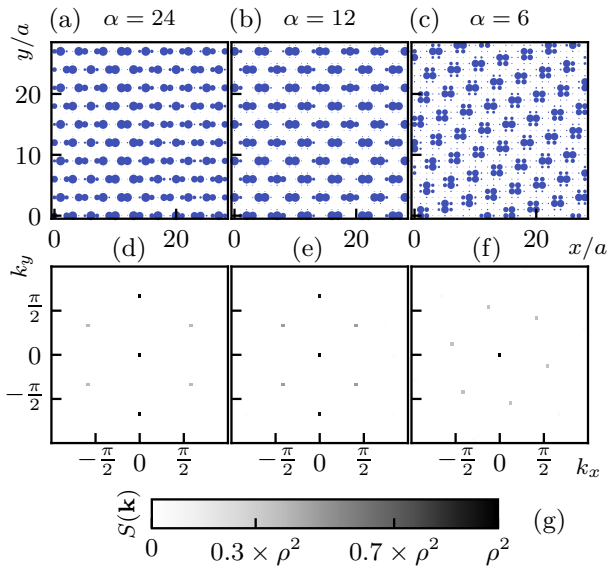

Figure 1.13.: Panels (a) to (c): site-density maps of a 48 × 48 system for different values of α. The size of each dot is proportional to the average occupation of the corresponding site. Calculation are performed at $T/t = 1/20$, $\rho = 5/36$, and $V/t = 10, 10, 12$ respectively. Panels (d) to (f): Heat map plot for the structure factor $S(\mathbf{k})$ for the same calculations as panels (a) to (c). The intensity-color scale is shown in panel (g).

1.4 Conclusion

We have demonstrated that stripe supersolid and crystals may be realized in the ground state of bosonic, frustration-free cluster-forming Hamiltonians. In particular, for intermediate interaction strength the competition between quantum fluctuations and classical cluster formation gives rise to a novel supersolid-supersolid transition between an isotropic cluster supersolid and an anisotropic stripe supersolid. These results illustrate the complexity of determining the quantum phase diagrams of systems with long-range interacting systems, in a regime numerics is still feasible. Intriguing out-of-equilibrium scenarios may also emerge and are the subject of the next chapter Chapter 2 . Our predictions could be of direct interest for experiments with cold Rydberg-dressed atoms in an optical lattice [121, 122]. More generally, they constitute a step towards the understanding of how long-range interactions can affect the properties of ultracold gases.

The results presented in this chapter are subject of the following publication: G. Masella, A. Angelone, F. Mezzacapo, G. Pupillo, and N. V. Prokof'ev. "Supersolid Stripe Crystal from Finite-Range Interactions on a Lattice". In: *Phys. Rev. Lett.* 123.4 (July 26, 2019), p. 045301. DOI: 10.1103/PhysRevLett.123.045301

2

Non-equilibrium scenarios in cluster-forming quantum lattice models

The search for ordered or disordered exotic states of matter is a very active field of investigation in condensed matter physics [7, 123, 124]. The interactions between the individual constituents of a given system play a fundamental role in this context, being intrinsically related to the physical mechanisms responsible for the stabilization of different (possibly novel) physical scenarios. Usually, intriguing equilibrium or out-of-equilibrium properties emerge in the presence of frustration, i.e., the impossibility of simultaneously satisfying a minimum energy condition for all terms of the Hamiltonian (see, e.g., [125, 126]). The latter may arise, for example, from competing interactions, polidispersity[1] and/or from the presence of peculiar substrates, i.e., lattices.

Recently, a large class of purely repulsive, isotropic extended-range interactions, whose relevance ranges from classical soft-matter systems [111, 112, 113] to cold Rydberg-atom experiments [56, 74, 75, 48, 57, 127, 128], has elicited considerable theoretical interest. Indeed, these potentials offer the possibility to explore a variety of equilibrium and out-of-equilibrium phe-

[1] Polydispersity is defined as the presence in the system of particles with different sizes, shape, or mass.

nomena in realistic models where frustration, in the forms discussed above, is not included. The main features of (pair-wise) extended-range interactions are a plateau which extends up to inter-particle distances of the order of a given critical radius r_c and a tail quickly approaching zero for $r > r_c$. In the classical limit, where quantum tunneling becomes negligible with respect to all the other couplings in the system, systems with extended-range interactions at high enough particle density ρ are characterized, by a so-called cluster crystalline ground state where crystalline sites are occupied by self-assembled aggregates of particles (i.e., clusters). Classical cluster crystals have been shown to possess peculiar equilibrium dynamical properties resembling those of glass-forming liquids, while still retaining structural order [129]. For these systems, out-of-equilibrium glassy scenarios where disorder coexists with clusterization have also been predicted [130, 131]. Furthermore, when quantum effects are taken into account, clusterization may lead to anomalous Luttinger-liquid behavior[2] in one spatial dimension [115, 116, 132, 133], as well as to the coexistence of diagonal long range order and superfluidity (i.e., supersolidity) in 2D free-space [71, 86, 87, 88] or on a triangular lattice [10]. Here, superfluidity may also be concomitant to glassiness in a so-called out-of-equilibrium superglass.

In order to gain insights into the novel physical phenomena related to clusterization, as well as into the interplay of the latter with quantum effects, system geometry, and interaction radius r_c, it is of crucial interest to extend the investigation to different lattices and choices of relevant parameters. In this context, a previous chapter of this thesis (Chapter 1) has been devoted to the study of the ground state phase diagram of a cluster-forming model of hard-core bosons with extended-range interactions on a square lattice. For such a model the ground state is a superfluid (stripe crystal) for sufficiently small (large) interaction strength V. Surprisingly, for intermediate values

[2] In Ref.[115], for the case of spinless fermions interacting via a finite-range pair-wise interaction on a 1D lattice, a new *cluster* Luttinger liquid phase is predicted. In this phase, contrary to a regular Luttinger liquid, the granularity in the liquid is given not by individual particles, but rather by *clusters* of particles.

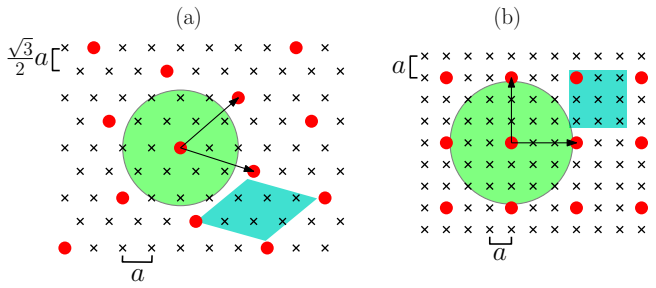

Figure 2.1.: Single-particle crystalline ground states of the extended Bose-Hubbard Hamiltonian in Eq. (2.1) on a triangular lattice for $r_c = 2a$ and $\rho = 1/7$ [panel (a)], and on a square lattice for $r_c = 2\sqrt{2}a$ and $\rho = 1/9$ [panel (b)]. Black crosses represents lattice sites while red dots occupied sites. Green circles highlight the range of the interaction around an occupied site, black arrows are the vectors generating the crystalline structure, and cyan regions indicate the primitive cells of the crystals.

of V a first order phase transition occurs between two different supersolids: an isotropic one, emerging from the superfluid when V is increased, and an anisotropic stripe supersolid emerging from the partial quantum melting of the large-V crystal when V is decreased. Here, since the large-V crystal is itself anisotropic, decreasing the interaction strengths leads to the formation of anisotropic superfluid exchanges.

As mentioned in Chapter 1 , the study of the ground state phases iscussed above required extensive calculations and careful temperature and interaction annealings[3] due to the presence of many competing out-of-equilibrium states. The nature of the latter, as well as their similarities and differences with respect to the equilibrium phases, are the focus of this chapter. We present a systematic study of the out-of-equilibrium scenarios of the model studied in Chapter 1 and it is organized as follows: in §2.1 we describe the Hamiltonian model of interest in detail with particular attention to its cluster-forming regimes and, briefly, the numerical methods adopted to carry out our in-

[3] Annealings consists here in the slow cooling of the system or in slowly changing the interaction strength V/t in the simulations starting from a state where equilibration is easy. This technique can be useful, if the step at which T/t or V/t is changed is sufficiently small and if equilibration is reached at every step, in removing internal defect in the systems that prevent proper crystallization and equilibration in some parameter ranges.

vestigation. By means of Path Integral Monte Carlo approach, we drive the system out of equilibrium via simulated low-temperature (T) quenches, analyzing the changes that this procedure induces on the equilibrium phases. The main findings, illustrated and discussed in §2.2, are: (i) As opposed to the isotropic and anisotropic supersolid equilibrium ground states, low temperature quenches leads to isotropic out-of-equilibrium (super)solid state. Remarkably, these are also found for values of V at which the equilibrium phases are instead anisotropic. (ii) The out-of-equilibrium counterpart of the equilibrium crystal at large V is a normal glass, similarly to what happens in a previous study of the same (albeith with smaller r_c) quantum model on a triangular lattice [10], as well as in the classical counterpart of the same model in free space [130]. (iii) No evidence of superglassy behavior is obtained in the investigated parameter range. The occurrence of such a state, which has been predicted for the triangular lattice, crucially depends on the interplay between lattice geometry, particle density and inter-particle interactions. Finally in §2.3 we outline the conclusions of our work.

2.1 Model and Methods

We investigate a model of monodisperse hard-core bosonic particles described by the Hamiltonian

$$H = -t \sum_{\langle ij \rangle} \left(b_i^\dagger b_j + \text{h.c.} \right) + V \sum_{i<j:r_{ij} \leq r_c} n_i n_j \tag{2.1}$$

Particles are confined on a square lattice of $N = L \times L$ sites and lattice constant a with periodic boundary conditions. Here t is the hopping coefficient between nearest-neighbor sites, b_i and $b_i^\dagger$ are annihilation and creation operators for hard-core bosons on site i, respectively, $n_i = b_i^\dagger b_i$, V is the interaction strength and r_{ij} is the distance between sites i and j. In the following, a and t will be taken as units of length and energy, respectively.

For $r_c = a$, i.e. nearest-neighbor potential, the phase diagram of the model contains superfluid, solid, and insulating phases [134], while supersolid states can be stabilized adding longer-ranged density-density interactions ($r_c > a$) [13, 135]. In the latter regime, which correspond to the case studied here, cluster formation also takes place in the system.

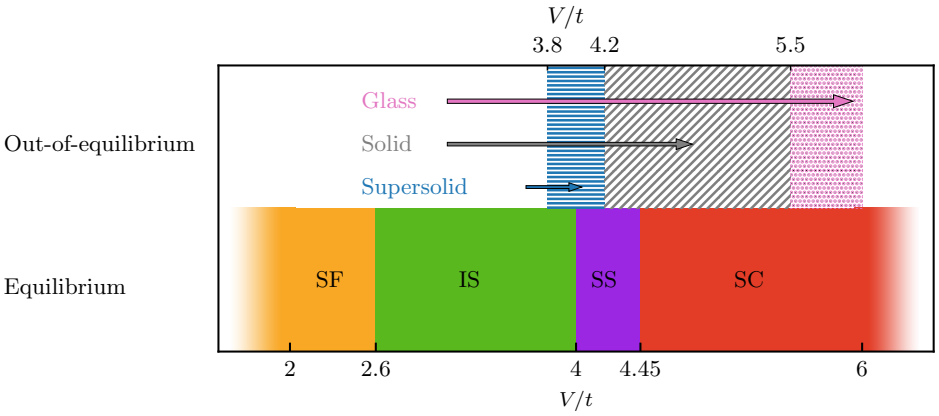

Figure 2.2.: Schematic phase diagram of Eq. (2.1) as a function of the interaction strength V/t. Each colored region in the lower part of the figure corresponds to a ground state equilibrium phase: namely, a superfluid (SF), an anisotropic stripe supersolid (SS), a anisotropic stripe supersolid (SS) and a stripe crystal (SC). The drawings are sketches of the crystalline structure (where present) of each equilibrium phase. The filling patterns in the upper part of the diagram identify the out-of-equilibrium states reached via simulated temperature quenching at target temperature $T/t = 1/20$. The regions where quenching leads to out-of-equilibrium supersolid, solid and glassy states are denoted by horizontal, diagonal or dot filling patterns, respectively.

For low enough particle density ρ, the classical (i.e., $V/t \to \infty$) ground state is a zero-energy single-particle crystal, where the inter-particle spacing is larger than the interaction radius. The maximum density ρ_c for which such a crystal exists is determined by r_c and the lattice geometry. As an example, while in the study of Eq. (2.1) on the triangular lattice [10] the choice $r_c = 2a$ results in a critical density $\rho_c^{\mathrm{tr}} = 1/7$, in the equilibrium study performed in Chapter 1 , on the other hand, a square lattice geometry with $r_c = 2\sqrt{2}a$ leads to a critical density $\rho_c^{\mathrm{sq}} = 1/9$. The single-particle crystalline structures corresponding to these densities are shown in Figs. 2.1(b) and 2.1(c), respectively.

For $\rho \gtrsim \rho_c$, a single-particle solid has a higher potential energy than a solid in which particles group up in tightly packed clusters. Indeed, the latter can arrange themselves far enough from each other to be noninteracting (i.e., outside of their mutual interaction radius). A larger value of ρ results in the

formation of larger clusters. For instance, on the triangular lattice the chosen value of $\rho = 13/36 \sim 2.5\rho_c^{\mathrm{tr}}$ led in [10] to clusters of 3 4 particles on average, while on the square lattice case (Chapter 1), for $\rho = 5/36 \sim 1.25\rho_c^{\mathrm{sq}}$, the largest clusters contain two particles.

When the system is driven away from thermal equilibrium, cluster formation can cause effective polidispersity[4], which in turn plays a fundamental role in the appearance of (super)glassy states [10]. This phenomenon is favored by large cluster sizes, as well as (sufficiently) strong interactions, which prevent particles from delocalizing between different clusters, as well as entire clusters from spatially rearranging to establish an ordered (crystalline) structure.

In this chapter we analyze the out-of-equilibrium physics of Eq. (2.1) for the same parameter range investigated in Chapter 1 . The model shows a rich ground state phase diagram, characterized by, e.g., competing supersolid phases. Understanding how temperature quenching may alter this scenario is one of the main objectives of the present study. Furthermore here, due to the presence of significantly smaller clusters of the ones appearing in Ref. [10], and for this reason frustration effects should be significantly weaker than those occurring in the same triangular lattice case. This would allow to determine, for instance, to which extent various out-of-equilibrium phenomena depend on clusterization.

We study the model Eq. (2.1) by means of Path Integral Quantum Monte Carlo simulations using Worm updates [5]. This technique, presented in detail in Appendix A , yields numerically exact results for unfrustrated bosonic systems and allows to accurately estimate observables such as the superfluid fraction ρ_s/ρ and the static structure factor $S(\mathbf{k})$, already defined in Eq. (1.3) , which measure superfluidity and crystalline order, respectively. Finally, we determine the single-particle Green Function defined as

$$G(\mathbf{r}) = \frac{1}{N}\sum_i \langle b_i^\dagger b_{i+\mathbf{r}}\rangle, \tag{2.2}$$

[4]Here, because of cluster formation, and to the presence of different types of clusters, the system can be seen as polydisperse (i.e., composed of particles of different size, shape or mass)

associated to the presence of off-diagonal (quasi) long-range order in our two-dimensional system.

Edwards-Anderson parameter Originally introduced in the mean field theory of spin glasses [126, 136], the Edwards-Anderson order parameter is the natural order parameter for a disordered phase. Here we define its renormalized version in terms of the boson number density as

$$Q_{\mathrm{EA}} = \frac{1}{Q^0_{\mathrm{EA}}} \sum_i \langle n_i - \rho \rangle^2 \tag{2.3}$$

whereas the normalization $Q^0_{\mathrm{EA}} = N\rho(1-\rho)$ is the value obtained for a fully localized state. By construction $Q_{\mathrm{EA}} = 0$ in every homogeneous phase while, any type of correlation between the site densities will lead to a non zero value of Q_{EA}. For this reason a finite value of Q_{EA} diagnoses the presence of a disordered (i.e., glassy) phase only in the absence of any kind of long-range diagonal order (e.g. $\max_{\mathbf{k}} S(\mathbf{k}) = 0$. [5]

We perform large-scale simulations with up to $N = 96 \times 96$ sites and temperatures between $T/t = 1$ and $T/t = 1/20$, the latter being the temperature investigated in the equilibrium case of Chapter 1 nd there yielding essentially ground state ($T = 0$) results. To gain insights into the out-of-equilibrium scenarios, we perform simulated temperature quenches: starting from a high-temperature configuration, we drive the system out-of-equilibrium by running low-temperature simulations without performing annealing steps in T as done in Chapter 1 .

2.2 Results

Equilibrium phases For clarity, we begin our discussion by summarizing the ground state phase diagram of model Eq. (2.1) (we refer the reader to Ref. [17] for an exhaustive discussion). The ground state (lower part of Fig. 2.2) is a superfluid (SF) at weak interactions, and an isotropic supersolid (IS) at $V/t = 2.6$. The system then undergoes a first-order transition at $V/t = 4.0$ to a supersolid state with anisotropic stripe crystalline structure and superfluid

[5] The interested reader can find an early use of the Edwards-Anderson order parameter in quantum Monte Carlo simulations in Ref. [137]

response, i.e., a anisotropic stripe supersolid (SS). Finally, superfluidity is lost at $V/t = 4.45$, and the ground state becomes a stripe crystal (SC).

Driving the system away from thermal equilibrium results in the out-of-equilibrium phase diagram shown in the upper part of Fig. 2.2, obtained via analysis of the relevant observables shown in Fig. 2.3, and Fig. 2.4 and discussed below. In the strongly interacting regime, i.e., $V/t > 5.5$, and for temperatures $T/t < 1/5$, the simulated quenches stabilize out-of-equilibrium states where diagonal long range order vanishes in the thermodynamic limit. As signaled by the finite value of Q_{EA} (see Fig. 2.3), concomitant to the absence of superfluidity, the resulting states are normal glasses. Conversely, following our quenches at $T/t = 1/20$ in the intermediate-V/t region (i.e., $3.8 \leq V/t \leq 4.6$) the system retains long range order, reaching out-of-equilibrium states with crystalline structures different from those obtained at equilibrium [see Fig. 2.4(d)]. These results allow to identify a variety of crystalline states in the out-of-equilibrium phase diagram. For $V/t < 4.2$ the system displays superfluid behavior [see Fig. 2.4(c)]. The latter coexists with diagonal long range order down to $V/t = 3.8$, pointing out the occurrence of out-of-equilibrium supersolid states in this parameter region. For $V/t < 3.8$ the system equilibrates to an IS and a SF for $V/t > 2.6$ and $V/t < 2.6$, respectively, rendering our quenching process ineffective. Remarkably, the out-of-equilibrium supersolids display features considerably different from their equilibrium counterparts. Specifically, both superfluid responses and crystalline order are essentially isotropic even when the corresponding equilibrium supersolids are strongly anisotropic.

For both high and intermediate interaction strengths V/t, we determine the level of equilibration of each simulated quench by performing it in several (i.e., $\gtrsim 30$) independent realizations, differing in both the initial configuration and in the thermalization seed of the quantum Monte Carlo (QMC) simulation. If our quench protocol is not sufficient to drive the system away from thermal equilibrium, essentially all the realizations will converge to the equilibrium state, since the details of the QMC stochastic dynamics in configuration space do not matter in this case. On the other hand, where the

out-of-equilibrium driving succeeds most of the realizations fail to equilibrate, with their initial conditions becoming crucial in determining the state reached by each simulation. A typical example of the latter behavior is shown in Fig. 2.3(a), where the mean value of an observable (in this case, the maximum value of the structure factor $S_{\mathrm{max}}^{(R)}$) strongly depends on the realization.

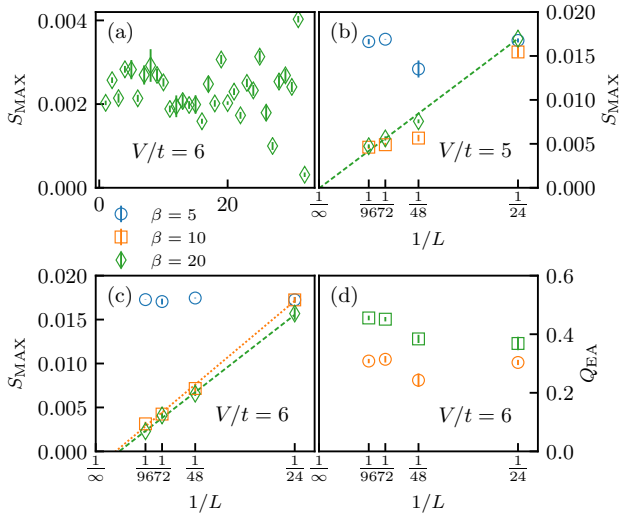

Figure 2.3.: Results for finite-temperature simulated quenches performed at $V/t = 5.0$ and $V/t = 6.0$. Panel (a): maximum value of the structure factor $S_{\mathrm{max}}^{(R)}$ as a function of the realization index for $L = 96$, $T/t = 1/20$, and $V/t = 6.0$. Panel (b): realization-averaged value of S_{max} as a function of the inverse system size for $V/t = 5.0$. Panel (c): same as for panel (b) for $V/t = 6.0$. Panel (d): Edwards-Anderson parameter Q_{EA} as a function of the inverse system size for $V/t = 6.0$. In panels (b) to (d) triangles, squares and circles correspond to $T/t = 1/5, 1/10, 1/20$, respectively. The dashed lines correspond to linear fits in $N^{-1/2}$, shown when estimates for the two largest sizes are not identical within numerical uncertainty.

Figures 2.3(b) to 2.3(d) show the scaling, as a function of the system size, of the realization-averaged maximum peak of the structure factor $S_{\mathrm{max}} = \max_{\mathbf{k}} S(\mathbf{k})$ and of the Edwards-Anderson order parameter Q_{EA} after quenching to different target temperatures for $V/t = 5.0$ [Fig. 2.3(b)] and $V/t = 6.0$ [Figs. 2.3(c) and 2.3(d)]. For these values of V/t, the observed out-of-equilibrium states are non-superfluid. We find equilibration to a stripe solid for $T/t = 1/5$ (triangles). A decrease of the target temperature results in fail-

ure to equilibrate the vast majority of realizations, which converge to states where diagonal long range order is suppressed with respect to the equilibrium scenario. For $V/t = 5.0$, $S_{\max}$ remains finite in the thermodynamic limit for $T/t = 1/10$ (filled squares) and $T/t = 1/20$ (filled circles), signaling an out-of-equilibrium crystal. Conversely, crystalline order is lost for $V/t = 6.0$ and $T/t = 1/10$ (empty squares) and $T/t = 1/20$ (empty circles). For these temperatures, Q_{EA} remains finite [Fig. 2.3(d)], signaling the emergence of glassy behavior.

Figure 2.4 shows a detailed comparison of the superfluid and crystalline order parameters for the out-of-equilibrium and equilibrium cases (full and empty symbols, respectively) as a function of V/t. Supersolid behavior occurs, after quenching, for $3.8 \leq V/t < 4.2$, i.e., in an interaction strength window smaller than that for which supersolidity is found at equilibrium. In particular, superfluidity vanishes in the thermodynamic limit for $V/t \geq 4.2$ (diamonds in Fig. 2.4(b)). More importantly, the features of these supersolid out-of-equilibrium states may be both quantitatively and qualitatively different from the equilibrium ones, whose order parameters are denoted for clarity by $\rho_s^{\mathrm{eq}}/\rho$ and $S_{\max}^{\mathrm{eq}}$, respectively. As expected, for small $V/t \lesssim 4$ our quenching protocol does not significantly alter the values of ρ_s/ρ and $S_{\max}$ with respect to $\rho_s^{\mathrm{eq}}/\rho$ and $S_{\max}^{\mathrm{eq}}$ [Figs. 2.4(c) and 2.4(d) and finite-size scaling for $V/t = 3.9$ (triangles in Figs. 2.4(a) and 2.4(b))]. For intermediate V/t, while at the transition between the IS and SS phases $S_{\max}^{\mathrm{eq}}$ (empty squares in Fig. 2.4(b)) develops strong anisotropy [17] and features a sizeable variation, $S_{\max}$ remains essentially constant (filled squares in Fig. 2.4(d)) and isotropic. Indeed, in all quench realizations the maximum peaks of the structure factor occur at realization-dependent wavevectors $\left(k_x^{(R)}, 0\right)$ and $\left(0, k_y^{(R)}\right)$ with $k_x^{(R)} \simeq k_y^{(R)}$ and $S^{(R)}\left(k_x^{(R)}, 0\right) \simeq S^{(R)}\left(0, k_y^{(R)}\right)$. Similarly, ρ_s/ρ (filled circles in Fig. 2.4(c)) takes considerably lower values than $\rho_s^{\mathrm{eq}}/\rho$ (empty circles in Fig. 2.4(c)) for $V/t \gtrsim 4.0$ and the superfluid response, as opposed to what found at equilibrium, is essentially isotropic. This clarifies the difference between the equilibrium supersolid states, which can be either isotropic or anisotropic, and the out-of-equilibrium ones, which are found to be always largely isotropic. Such

a difference persists even in the absence of superfluidity in the out-of-equilibrium states: for example, for $V/t > 4.45$ the ground state is a stripe crystal while quenching results in the appearance of substantially isotropic crystals and glasses.

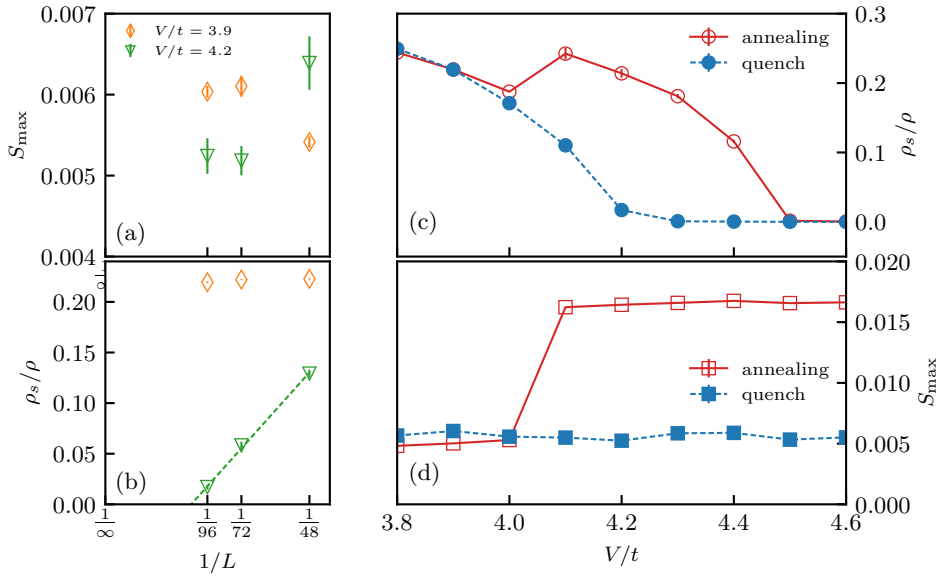

Figure 2.4.: Panels (a) and (b): scaling in the inverse size of ρ_s/ρ and $S_{\max}$ for $V/t = 3.9$ (triangles) and $V/t = 4.2$ (diamonds) at $T/t = 1/20$. Dashed lines are linear fits to the numerical data, shown when estimates for the two largest sizes are not identical within their uncertainty. Panel (c): comparison between the equilibrium superfluid fraction $\rho_s^{\mathrm{eq}}/\rho$ (empty circles) and the out-of-equilibrium one ρ_s/ρ (filled circles) as a function of the interaction strength at $T/t = 1/20$, and $L = 96$. Panel (d): comparison of the equilibrium maximum value of the structure factor $S_{\max}^{\mathrm{eq}}$ (empty squares) and the out-of-equilibrium one $S_{\max}$ (filled squares) for the same parameters of panel (c). In panels (c) and (d), solid and dashed lines are guides to the eye.

The isotropic character of the out-of-equilibrium states can also be inferred by inspection of G_x and G_y, i.e., the single-particle Green Function $G(\mathbf{r})$ along the x and y directions, respectively. For $V/t = 4.1$, G_x and G_y of the corresponding anisotropic SS ground state (triangles and circles in Fig. 2.5(a), respectively) are clearly different. Specifically, while both decay algebraically as a function of the distance, signaling quasi-off-diagonal long range order, G_y is characterized by oscillations in correspondence of the stripe periodicity.

The out-of-equilibrium $G(\mathbf{r})$, on the other hand, is essentially isotropic, i.e., $G_x \sim G_y$ (solid lines in Fig. 2.5(a) where, for simplicity, only G_y is shown).

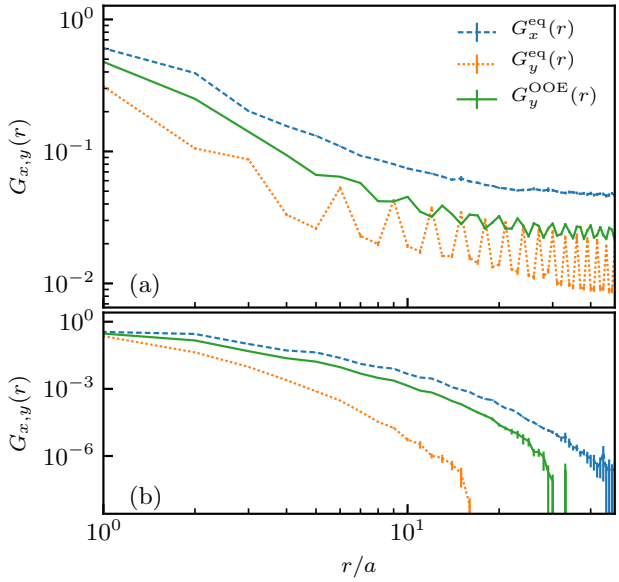

Figure 2.5.: Single-particle Green function $G(\mathbf{r})$ for $V/t = 3.9$ [panel (a)] and $V/t = 4.2$ at $T/t = 1/20$. Dashed and dotted lines refers to the equilibrium green functions $G_x^{\rm eq}(r)$ and $G_y^{\rm eq}(r)$ along the x and y direction, respectively. Solid lines denote the out-of-equilibrium $G_y(\mathbf{r})$ along the y direction. The corresponding out-of-equilibrium $G_x(\mathbf{r})$ along the x direction (not shown) is essentially identical. Figure 2.5(b): same as Fig. 2.5(b) for $V/t = 6.0$. In both panels $T/t = 1/20$ and $L = 96$.

Fig. 2.5(b) displays the same comparison for $V/t = 6.0$. Here the decay of the $G(\mathbf{r})$, both at equilibrium and out-of-equilibrium, is exponential, as expected for a nearly classical crystal and a glass, respectively. Also in this case, the equilibrium $G(\mathbf{r})$ is strongly anisotropic, while $G_x \sim G_y$ in its out-of-equilibrium counterpart.

Further insight into the out-of-equilibrium physics of our model can be gained from the averaged occupation maps in Fig. 2.6. In both cases shown in the figure [$V/t = 6.0$ in Fig. 2.6(a) and $V/t = 4.1$ in Fig. 2.6(b)] particles clusterize; for strong V/t, clusters have in general different shapes and orientations. These induce an effective polidispersity[4], ultimately resulting in glassy behavior [130]. On the other hand, for $V/t = 4.1$, where the system is supersolid, particles can "hop" between different clusters, establishing long-

range exchanges which give rise to a sizeable superfluid response. The latter is concomitant with a well defined crystalline structure.

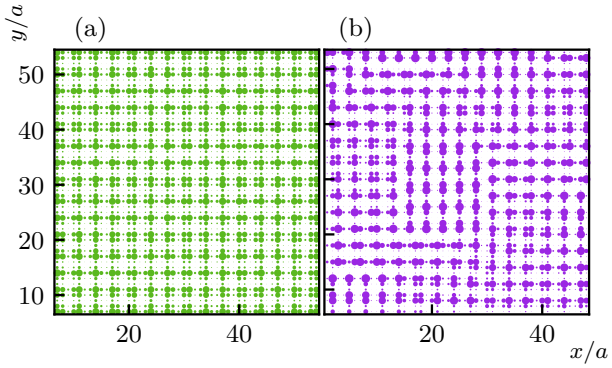

Figure 2.6.: Figure 2.6(a): portion of a site occupation map for one realization for $L = 96$, $T/t = 1/20$, and $V/t = 6.0$. Figure 2.6(b): same as panel Fig. 2.6(a) for $V/t = 4.1$. The size of the dots is proportional to the occupation of each site.

It is important to mention that no evidence of superglassy behavior (e.g., no superfluidity in glassy phases) has been found in the parameter range investigated in this work. This constitutes an important difference with the results of our recent study of model Eq. (2.1) for $r_c = 2$ on the triangular lattice [10].

A qualitative explanation can be given in terms of a simple energetic argument. Indeed, the ratio Λ between potential and kinetic energy can be used to roughly estimate particle mobility. When Λ is large (large V/t), particles and clusters formed after quenching, are strongly localized, preventing the realization of a crystalline structure. Superglassy behavior emerges as a delicate balance between localization and superfluidity, which instead takes place, at low T/t, for small Λ.

Indeed, on the triangular lattice superglasses were observed as the out-of-equilibrium counterparts of supersolids at $\Lambda \sim 9$ and $\rho_s/\rho \sim 0.1$. On the other hand, the equilibrium supersolid phases of model Eq. (2.1) on the square lattice are characterized by much smaller $\Lambda \sim 1.1\ 1.3$ and higher $\rho_s/\rho \sim 0.2$. Here the out-of-equilibrium driving leads to superfluid states where, due to larger mobility, crystalline order can be restored.

2.3 Conclusion and Outlook

In this chapter we studied the out-of-equilibrium scenarios of a model of monodispersed hard-core bosons on a square lattice with an extended-range potential of the soft-shoulder type, of interest for experiments with cold Rydberg-dressed atoms. In the parameter region of our investigation, the ground state of the model is a cluster crystal and a superfluid for strong and weak interactions respectively, and an unusual transition between an isotropic and an anisotropic supersolid state occurs for intermediate interaction strength.

Via simulated temperature quenches, we obtain a glass region for strong interactions, while for moderate values of the latter a supersolid region appears. We show that such a supersolid is qualitatively different from the ground state one, being essentially isotropic even for values of the interaction strength for which the corresponding ground state is anisotropic.

For all interaction strength values where out-of-equilibrium superfluidity remains finite, long range crystalline order is also maintained. Therefore, no evidence of superglassy behavior is found in our region of investigation, as opposed to the case of the triangular lattice [10], where the presence of such such an exotic state is demonstrated. This discrepancy can be qualitatively explained in terms of the strong difference in the potential to kinetic energy ratio, which takes significantly different values on the two mentioned lattice geometries. In particular, this quantity is considerably smaller on the square lattice, signaling increased particle mobility. The latter suppresses particle and cluster localization, which is an essential ingredient for the onset of glassy physics.

3

Energy extensivity in quantum long-range interacting systems

In Chapter 1 and in Chapter 2 we presented the study of a model with finite-range interactions which interpolates between nearest-neighbor and long-range couplings while remaining numerically tractable. In these previous chapters we studied the ground state phase diagram and the out-of-equilibrium scenarios emerging from this model while, at the same time, we unveiled the complexity arising due to the proliferation of low-energy metastable states in long-range interacting systems.

Typical long-range models are characterized by an interaction potential which decays algebraically, as $1/r^{\alpha}$, with the distance (r) between the constituents. For d-dimensional systems, the so called *strong* long-range regime is achieved when the power-law exponent of the interaction is such that $\alpha \leq d$. This regime is typically associated to unusual thermodynamic properties such as a non-extensive energy $E \sim \mathcal{V}^{2-\frac{\alpha}{d}}$ leading to an ill-defined thermodynamic limit [138]. Furthermore, the total energy cannot be obtained by summing up the energies of different subsystems as is usually the case for short-range interactions [139, 140]. This non-additivity appears as a fundamental property of long-range models and leads to exotic behaviors including the breaking of ergodicity, the existence of slow relaxation processes, and the nonequivalence of statistical ensembles [141, 142, 96, 143].

A typical and still actively studied long-range quantum model has been introduced by Schulz and consists of one-dimensional (1D) fermions in free-space interacting via a $1/r^{\alpha=1}$ (unscreened) Coulomb potential, with r the distance separating two particles. In [144], Schulz showed using bosonization techniques that the ground state of this system is a peculiar metal resembling a classical Wigner crystal, with very slow decay of the charge correlations associated to the plasmon mode [144, 145]. This result was confirmed numerically using density matrix renormalization group (DMRG) [146] and variational Monte Carlo methods [147, 148, 149]. In the presence of a lattice at commensurate fillings, it was shown that while the metallic behavior is surprisingly enhanced as compared to short-range interactions for small system size, the ground state ultimately enters an insulating phase in the thermodynamic limit [150, 16, 151, 152].

Here we investigate how restoring energy extensivity in a long-range interacting model affects its fundamental physical properties. Energy extensivity can be typically restored by rescaling the interaction potential with an appropriate volume-dependent factor Λ, which is known as Kac's prescription [15]. The latter is systematically used to study the thermodynamic properties of classical spin models with long-range interactions [153, 154, 155, 156, 157], where the dynamical properties with and without Kac's rescaling are the same provided the respective time scales t_{res} and t satisfy $t = t_{\text{res}}/\sqrt{\Lambda}$ [158, 159]. However, it can be shown that the latter statement does not hold true in quantum systems. It is an open and interesting question to investigate what other properties such as ground state phases can be fundamentally modified by Kac's rescaling.

This chapter is devoted to the study of a one-dimensional periodic chain of hard-core bosons in the strong long-range interacting regime both in the presence and absence of Kac's prescription. In §3.1, we introduce the model and the methods used in this study, namely the Density Matrix Renormalization Group (DMRG) and the Luttinger liquid theory. In §3.2, we discuss the results, and show that the main findings of Ref. [16], obtained in the absence of Kac's rescaling and for $\alpha = 1$ can be extended to the whole range

$0 \leq \alpha \leq 1$. Here the ground state consists of an insulating gapped phase in the thermodynamic limit. However, in striking contrast with these results, Kac's prescription leads to a metallic phase for any finite strength of the interaction for every $0 \leq \alpha \leq 1$ in the thermodynamic limit. By computing the Luttinger parameters from the single-particle correlation function, from the structure factor, and from the charge gap and the charge stiffness, we demonstrate that, surprisingly, this metallic phase is incompatible with a conventional Luttinger liquid description. Restoring extensivity thought the Kac's prescription is further shown to eliminate the plasmon modes while preserving the long-range character of the potential, and with it inherent properties of the strong long-range regime, such as non-additivity. Finally, a conclusion is drawn in §3.3.

The work presented in this chapter is the product of a collaboration with Thomas Botzung[1], David Hagenmuller[1] and all the co-authors of the publication: T. Botzung, D. Hagenmüller, G. Masella, J. Dubail, N. Defenu, A. Trombettoni, and G. Pupillo. "Effects of Energy Extensivity on the Quantum Phases of Long-Range Interacting Systems". Submitted to: Phys. Rev. Lett. *(2019). arXiv: 1909.12105, currently submitted for review to Physical Review Letters.*

3.1 Model and methods

We consider the Hamiltonian

$$H = -t \sum_{i=1}^{L} \left(b_i^\dagger b_{i+1} + \text{h.c.} \right) + \sum_{i>j} V_{i-j}^{(\alpha)} n_i n_j, \tag{3.1}$$

where the operator b_i ($b_i^\dagger$) annihilates (creates) a hard-core boson on site $i = 1, \cdots, L$ satisfying the commutation relations

$$\left[b_i, b_j^\dagger \right] = \delta_{ij}(1 - 2n_i) \tag{3.2}$$

where $n_i = a_i^\dagger a_i$ is the local density which, due to Eq. (3.2), can only be 1 or 0. The interaction potential reads

$$V_{i-j}^{(\alpha)} = \frac{V}{\Lambda_\alpha(L) r_{ij}^\alpha} \qquad V > 0, \tag{3.3}$$

[1] Institut de Sciences et d'Ingenierie Supramoleculaires and University of Strasbourg

where the distance r_{ij}

$$r_{ij} = \frac{La}{\pi} \sin\left(\frac{\pi}{L}|i-j|\right) \tag{3.4}$$

corresponds to the chord distance as depicted in Fig. 3.1 (we assume that the sites are uniformly distributed on a ring).

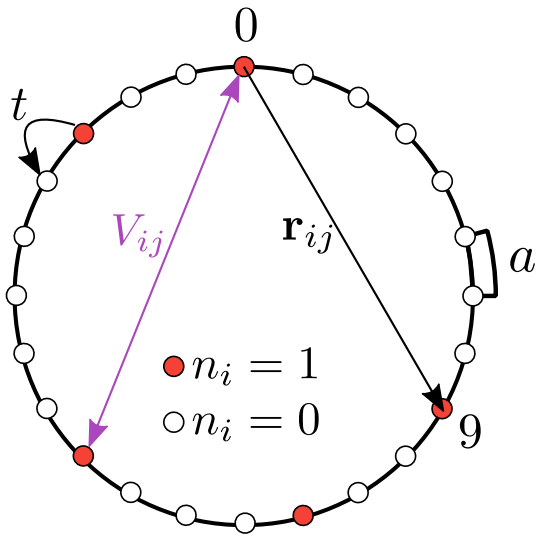

Figure 3.1.: Sketch of the model Eq. (3.1). Sites (white circles) are arranged on a ring with uniform spacing a. The distance between two sites is given by the cord distance Eq. (3.4). Bosons (red circles) can hop to nearest neighboring site with hopping amplitude t. The maximum occupation number is $n_i = 1$ due to the hard-core constraint.

In the following, the nearest neighbor hopping t and lattice spacing a are taken as unit of energy and space, respectively (with $a \equiv t \equiv 1$). Kac's rescaling of the interaction potential is included via the function

$$\Lambda_\alpha(L) = \begin{cases} 1 & \alpha > 1 \\ L^{1-\alpha} & \alpha < 1 \\ \log(L) & \alpha = 1. \end{cases} \tag{3.5}$$

Mapping to other models We note that such a model of hard-core bosonic particles can be mapped onto a XXZ Heisenberg model for spin-1/2 particles with long range couplings by directly mapping the spin operators S_i^+, S_i^-, and S_i^z to the bosonic annihilation and creation operators via the relations [160]

$$S_i^+ = b_i,\ S_i^- = b_i^\dagger,\ S_z = \frac{1}{2} - b_i^\dagger b_i \tag{3.6}$$

which result, by substituting Eq. (3.6) into Eq. (3.2), in the known commutation relations for spin-1/2 operators

$$\left[S_i^+,\, S_j^-\right] = 2\delta_{ij}S_i^z,\ \left[S_i^\pm, S_j^z\right] = \mp\delta_{ij}S_i^\pm \tag{3.7}$$

and in the Hamiltonian

$$\mathcal{H}_{XXZ} = J^x \sum_{\langle ij\rangle} \left(S_i^+ S_j^- + S_i^- S_j^+\right) + J^z \sum i < j \frac{1}{r_{ij}^\alpha} S_i^z S_j^z, \quad J^x = -2t,\, J_{ij}^z = V_{ij} \tag{3.8}$$

We also note that such model can be mapped into a model of spinless fermions via Jordan-Wigner transformations (see e.g., Refs. [161] for an example of such mapping).

Methods and techniques The study of the ground state properties of Eq. (3.1) presented in §3.2 is performed via a combination of numerical and analytical tools including *Luttinger liquid theory* and the DMRG. Our DMRG implementation is based on the publicly available `ITensor C++ library` [162]. Calculations are performed for large system sizes ($L \gtrsim 200$ sites) both with and without Kac's rescaling.

3.2 Results

In Fig. 3.2, for a choice of $\alpha = 1$ and for different interaction strengths V/t, we compute the single-particle charge gap defined in terms of the ground state energies E_0 for states with N, $N-1$, and $N+1$ particles.

$$\Delta = (E_0(N+1) - E_0(N)) - (E_0(N) - E_0(N-1)) \tag{3.9}$$

The situation without Kac's rescaling [$\Lambda_1(L) = 1$, Figs. 3.2(a) and 3.2(b)] has been already investigated in Ref. [16], and features a non-extensive energy. In this case, we find that the gap $\Delta(L \gg 1) \neq 0$ for any $V > 0$, which indicates an insulating phase in the thermodynamic limit consistently with the conclusion of Ref. [16]. These results are drastically modified when using the Kac's prescription. By rescaling the interaction potential [$\Lambda_1(L) = \log(L)$, Figs. 3.2(c) and 3.2(d)], we find that while extensivity is clearly restored, $\Delta \sim 1/L$ for all $V > 0$. This result indicates a metallic behavior in the thermodynamic limit

observed in the whole range $0 \leq \alpha \leq 1$ (not shown). This constitutes the main result of this chapter.

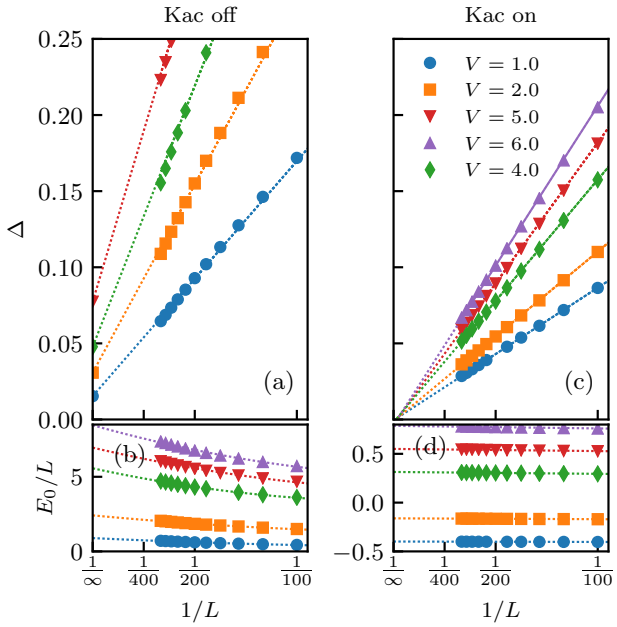

Figure 3.2.: Finite-size scaling of the single-particle gap Δ computed with DMRG at half-filling $\langle n_i \rangle = 0.5$, for $\alpha = 1$ and different interaction strengths V (in units of the hopping energy t). While an insulating phase ($\Delta \neq 0$) is found without Kac's rescaling panels (a) and (b), the latter leads to a metallic phase ($\Delta = 0$) in the thermodynamic limit panels (c) and (d). Extrapolation for $L \to \infty$ is obtained by fitting the numerical data with $\Delta(L) = b + \frac{c}{L} + \frac{d}{L^2}$ (dotted lines). The finite-size scaling of the ground state energy per particle is shown in panels (c) and (d).

In order to understand the physical origin of the significant difference between the extensive and non-extensive models, we investigate the low-energy properties of Eq. (3.1) using the Luttinger liquid theory. A convenient bosonic representation of H in terms of the continuous variable $x \equiv ja$ can be obtained by treating the interaction potential as a perturbation [163]

$$H = \frac{1}{2\pi} \int dx \, uK \, (\pi \Pi)^2 + \frac{u}{K} \nabla^2 \phi - \frac{g}{\pi a^2} \cos(4\phi) \,, \tag{3.10}$$

where $\Pi(x)$ and $\phi(x)$ and are canonically conjugate bosonic fields depending on the long wavelength fluctuations of the fermion density. The so-called

Luttinger parameters u and K are related by [16] Appendix B

$$\begin{aligned} uK &= v_{\mathrm{F}} \\ \frac{u}{K} &= v_{\mathrm{F}} + \frac{1}{\pi}\sum_{r=1}^{L} V_r^{(\alpha)}\left[1-\cos\left(2k_{\mathrm{F}}r\right)\right] \end{aligned} \tag{3.11}$$

where v_{F} denotes the Fermi velocity and k_{F} the Fermi wave vector. The first two (quadratic) terms of Eq. (3.10) describe how the properties of the non-interacting Luttinger liquid are renormalized by the interactions. In particular, K determines the decay of the single-particle correlation function $\langle a_i^\dagger a_j\rangle \sim r_{ij}^{-1/(2K)}$. The third term in Eq. (3.10) stems from scattering processes across the Fermi surface where the particle momentum is conserved up to a reciprocal lattice vector. It is usually denoted as umklapp term and scales with the strength

$$g = \sum_{r=1}^{L} V_r^{(\alpha)} \cos\left(2k_{\mathrm{F}}r\right). \tag{3.12}$$

For a finite g, it is possible to show using a renormalization-group study [163] of the Hamiltonian Eq. (3.10) that the system goes from an insulating to a metallic phase as K is increased above a critical value K_c. At half-filling, and neglecting multiple umklapp scattering [164], the critical value is $K_c = 0.5$. Note that in the case of a nearest-neighbor interaction $\alpha \to \infty$, such a metal-insulator transition occurs at $V = 2t$ [165].

We consider a half-filled band $\langle n_i\rangle = 0.5$, which provides $k_{\mathrm{F}} = \pi/2$ and $v_{\mathrm{F}} = 2$. In the absence of Kac's rescaling, the first sum $\sum_r V_r^{(\alpha)}$ entering Eq. (3.11) diverges in the thermodynamic limit $\sim \log(L)$ for $\alpha = 1$ and $\sim L^{1-\alpha}/(1-\alpha)$ for $0 \le \alpha < 1$. The second sum $\sum_r V_r^{(\alpha)} \cos\left(2k_{\mathrm{F}}r\right)$ entering Eqs. (3.11) and (3.12) is bounded due to the alternating sign. Therefore, while the umklapp scattering strength g remains finite, the Luttinger parameter $K \to 0$ for $0 < \alpha \le 1$ and $V > 0$ in the thermodynamic limit, consistently with an insulating phase.

We find that rescaling the interaction potential with the factor $\Lambda_\alpha(L) = \log(L)$ for $\alpha = 1$ and $\Lambda_\alpha(L) = L^{1-\alpha}$ for $\alpha < 1$ strongly affects the competition between K and g. In this case, the long-wavelength divergence is removed since $\lim_{L\to\infty}\sum_r V_r^{(\alpha)} = V$ for $\alpha = 1$ and $\lim_{L\to\infty}\sum_r V_r^{(\alpha)} = V/(1-\alpha)$ for $\alpha < 1$. This suggests a metallic phase for $0 < \alpha \le 1$, since K remains fi-

nite and $g \to 0$ for any finite $V > 0$ in the thermodynamic limit as seen from Eqs. (3.11) and (3.12)).

The above arguments cannot be used in the case $\alpha = 0$ since the series $\sum_r V_r^{(\alpha)} \cos(2k_F r)$ does not have a unique limit for $L \to \infty$. Nevertheless, this particular case can be solved exactly using a mean-field approach. This leads to a free fermion (metallic) phase with charge correlations $\langle a_i^\dagger a_j \rangle \sim r_{ij}^{-1/2}$, regardless of the presence or absence of Kac's rescaling Appendix B . This phase was referred to as a strange metal in Ref. [152], since a finite gap $\Delta = V$ is found for $L \to \infty$ in the absence of Kac's rescaling. Upon restoring a well-defined thermodynamic limit ($V \to V/L$), we find that the gap $\Delta \sim (V + 2\pi t)/L \to 0$ for $L \to \infty$ consistently with a metallic phase.

In order to gain further insights, we first compute the Luttinger parameter K by fitting the correlation function $\langle a_i^\dagger a_j \rangle$, and represent it in Fig. 3.3 for different V and $\alpha = 0.5$. We observe two opposite trends depending on whether Kac's rescaling is present or not. In the latter case [Fig. 3.3(a)], K decreases when increasing L and lies below the critical value $K_c = 0.5$ for $L \to \infty$, which indicates an insulating phase. The case with Kac's rescaling is shown in Fig. 3.3(b), where a finite K is found for all V in the thermodynamic limit.

We then compute the charge stiffness [163]

$$D = \pi L \left| \frac{\partial^2 E_0(\Phi)}{\partial \Phi^2} \right|_{\Phi=0}, \tag{3.13}$$

which is proportional to the Drude weight [167] and therefore provides valuable information on the metallic or insulating properties of the system. Moreover, it also gives a direct measure of the umklapp scattering strength. A large D corresponds to a good metal, while an insulating phase features $D = 0$. The charge stiffness is computed numerically from the ground state energy E_0 by threading a flux Φ through the circular chain, and represented in Fig. 3.4 as a function of $1/L^2$ for $\alpha = 0.5$. In the absence of Kac's rescaling [Fig. 3.4(a)], D decreases when increasing L for any finite V. The latter drives the system towards an insulating phase ($D \to 0$) in the thermodynamic limit. In contrast, D increases with L in the presence of Kac's rescaling [Fig. 3.4(b)], which confirms the existence of a metallic behavior. In the thermodynamic limit,

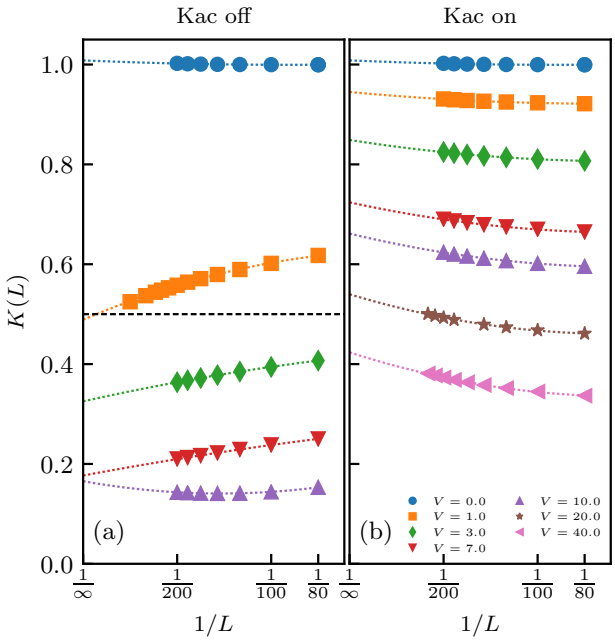

Figure 3.3.: Luttinger parameter K computed numerically at half-filling for $\alpha = 0.5$ and different V, by fitting the correlation function $\langle a_i^\dagger a_j \rangle$ derived in Ref. [166]. The critical value $K_c = 0.5$ indicating the metal-insulator transition with nearest neighbor interaction is displayed as a black dashed line. In the absence of Kac's rescaling [panel (a)], K decreases when increasing L, lying below the critical line for $L \to \infty$ (insulating phase). In contrast, K increases with L in the presence of Kac's rescaling [panel (b)], and remains finite even for very large V (metallic phase). Extrapolation in the thermodynamic limit is obtained by fitting the data with the same function as in Fig. 3.2 (dotted lines).

we find that $D \approx v_F$ even for very large V, in surprisingly good agreement with the Luttinger liquid prediction $D = uK$ and Eq. (3.11). Note that we have performed a full numerical study showing that the conclusions drawn from Figs. 3.3 and 3.4 can be unambiguously extended to the whole range $0 \leq \alpha \leq 1$.

Now that we have demonstrated the metallic character of the ground state, we check the validity of the Luttinger liquid theory in Fig. 3.5 by computing the parameter K for $L \to \infty$ and $\alpha = 0.5$ in three different ways: From the single-particle correlation function $\langle a_i^\dagger a_j \rangle$ (see above), from the static structure

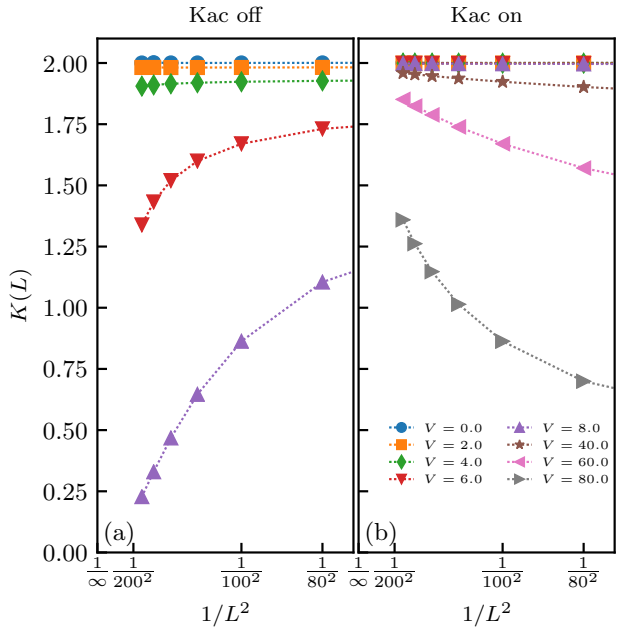

Figure 3.4.: Charge stiffness D computed numerically from Eq. (3.13) at half-filling, as a function of $1/L^2$ for $\alpha = 0.5$ and different V. The magnetic flux Φ is implemented via the twisted boundary condition $c_1 = e^{i\Phi} c_{L+1}$ [164]. Two opposite trends are observed depending on whether Kac's rescaling is present (panel (b)) or not (panel (a)). While $D \to 0$ for $L \to \infty$ in the latter case (insulator), D remains finite in the former case (metal).

factor

$$S(q) = \frac{1}{L} \sum_{i,j} e^{\mathrm{i}q|i-j|} \left(\langle n_i n_j \rangle - \langle n_i \rangle \langle n_j \rangle \right) \tag{3.14}$$

as $K = LS(q = 2\pi/L)$, and from the relations $\pi \frac{u}{K} = \frac{\partial \Delta}{\partial (1/L)}$ and $uK = D$ stemming from the Luttinger liquid theory [163]. In the absence of Kac's rescaling [Fig. 3.5(a)], a discrepancy between the values of K extracted from the two correlation functions (labeled K_{1p} and K_{2p} in the figure) is observed, which indicates the breakdown of the Luttinger liquid theory related to the opening of a gap (insulating phase). The agreement obtained for small V is attributed to the metal-like character at finite L consistently with the data shown in Fig. 3.3. In the presence of Kac's rescaling [Fig. 3.5(b)], K_{1p} and K_{2p} match well up to very large V, while they match neither the formula $K = 1/\sqrt{1 + V/[\pi v_F (1-\alpha)]}$ (dotted line) stemming from Eq. (3.11) nor K

obtained from Δ and D (labeled $K_{\Delta/\mathrm{D}}$ in the figure). We find that this discrepancy holds in the entire range $0 \leq \alpha \leq 1$ (see inset), implying a breakdown of Luttinger liquid theory in the strong long-range regime. For $\alpha > 0$, this breakdown is only partial since numerics indicate that both $K_{\Delta/\mathrm{D}}$ and $K_{1\mathrm{p},2\mathrm{p}}$ maintain the functional form

$$K = \frac{1}{\sqrt{1 + \gamma V/(\pi v_{\mathrm{F}})}} \tag{3.15}$$

with γ finite for all V [see Fig. 3.5(b)]. This is, however, not true for $\alpha = 0$ which can be solved analytically Appendix B . In this case, the free fermion result $K_{1\mathrm{p},2\mathrm{p}} = 1$ for all V extracted from the correlation functions differs significantly from the functional form Eq. (3.15) ($\gamma = 0$). Interestingly, we find that $K_{\Delta/\mathrm{D}}$ is correctly described by Eq. (3.15) with $\gamma = 1$, which corresponds exactly to the analytic prediction obtained from Eq. (3.11). Note that in the short-range case $\alpha \gg 1$, all methods predict the same K as expected from the Luttinger liquid theory (see inset). The demonstration of this gapless, criticalAppendix B metallic phase that does not fall into the conventional Luttinger liquid theory is a central result of this work. While here we focused on the case of half-filling, this phase appears in fact for all densities.

In the supplemental material, we show that the long-wavelength excitations of this metallic phase have a linear dispersion, similar to a Luttinger liquid with short-range interactions. This can be readily shown by considering the continuous Hamiltonian Eq. (3.10) with interaction potential $V^{(\alpha)}(x) = V/\left(x^2 + a^2\right)^{\alpha/2}$. The diagonalization of this Hamiltonian in Fourier space provides the plasmon dispersion relation $\omega(q) = v_{\mathrm{F}} q \sqrt{1 + V^{(\alpha)}(q)/(\pi v_{\mathrm{F}})}$. Kac's rescaling eliminates the long-wavelength divergence of the Fourier component $V^{(\alpha)}(q \to 0)$ and therefore leads to the dispersion relation of a metal with short-range interactions $\omega(q) \sim v_{\mathrm{F}} q$. Note that since the algebraic character of the interaction potential is preserved when using the Kac's prescription, the latter is thus "weaker" than Thomas-Fermi screening which turns the long-range interaction into a short-range one.

3.3 Conclusion

In this chapter we have shown that the low-energy properties of one-dimensional hard-core bosonic particles interacting via a long-range potential are fundamentally modified when restoring energy extensivity and thus a well-defined thermodynamic limit. When energy extensivity is restored, we find an unusual metallic phase that is not described by the Luttinger liquid theory. Since the linear excitation spectrum of this phase is also present for higher-dimensional systems ($d > 1$) in the case $\alpha = 1$, investigating the properties of such an unconventional liquid with restored energy extensivity in higher dimension [168] is an interesting prospect.

Such study could be of interest for systems in which interactions are naturally long-range and extensive, such as of cold and ultracold atoms with cavity-mediated long range interactions [68]. For instance, the case $\alpha = 0$ can be typically obtained when the spatial extent of the atomic cloud is much smaller than the cavity wavelength [169].

We also note that the Kac's prescription Eq. (3.5) in not the only way to restore energy extensivity in the model Eq. (3.1). An alternative Kac's prescription indeed consists in dividing the whole Hamiltonian Eq. (3.1) by $\Lambda_\alpha(L)$. In this case, the behaviors of the correlation function and of the charge stiffness are not affected by such a global rescaling, and are therefore those of an insulator. However, the charge gap vanishes in the thermodynamic limit since the energy of the ground state E_0 is simply replaced by E_0/L, and the system exhibits an hybrid insulating/metallic behavior.

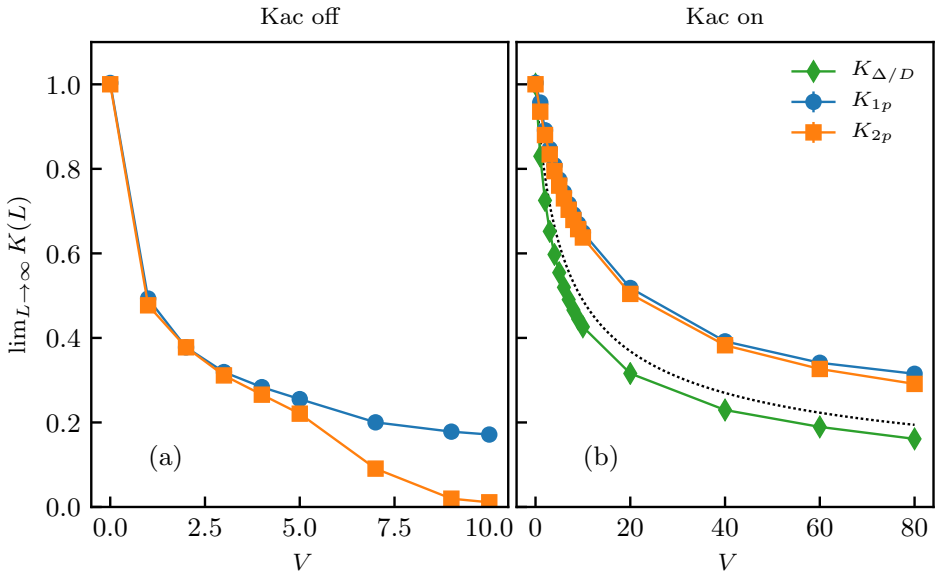

Figure 3.5.: Luttinger parameter K extrapolated in the thermodynamic limit versus V at half-filling and for $\alpha = 0.5$, without (panel (a)) and with (panel (b)) Kac's rescaling. K is computed in 3 different ways: From the single-particle correlations (K_{1p}), the structure factor (K_{2p}), and from the gap and the charge stiffness ($K_{\Delta/D}$). The formula obtained from Eq. (3.11) is displayed as a dotted line. Inset: $|K_{1p} - K_{2p}|$ and $|K_{1p} - K_{\Delta/D}|$ versus α for $V = 1.5$. A discrepancy between K_{1p} and K_{2p} is observed without Kac's rescaling, which indicates the breakdown of the Luttinger liquid theory (insulator). In contrast, the property $K_{1p} = K_{2p}$ observed with Kac's rescaling even for large V suggests a metallic phase, which is not captured by the conventional Luttinger liquid theory since $K_{\Delta/D}$ does not match $K_{1p,2p}$ for $\alpha < 1$. In the short-range case $\alpha \gg 1$, one recovers $K_{1p,2p} = K_{\Delta/D}$ in agreement with the standard Luttinger liquid theory.

4

Conclusions and Outlooks

In this Ph. D. work I investigated the emergence of exotic phenomena in strongly-correlated models of direct experimental interest in ultracold atomic gases. I have focused this study on many-body systems of bosonic particles interacting via finite- and long-range potentials using state-of-the-art numerical techniques described in Appendix A .

In the first chapter we studied a frustration-free cluster-forming model of hard-core bosonic particles interacting via a finite-range potential. We have demonstrated that stripe supersolid and crystals may be realized in the ground state of such model. In particular we demonstrated the presence, at intermediate interaction strengths, of a novel supersolid-to-supersolid transition between isotropic and anisotropic supersolids. This transition is understood in terms of the competition between quantum fluctuations and classical cluster formation. These results illustrate the complexity of determining the quantum phase diagrams of systems with long-range interacting systems in a regime where numerical simulations are still feasible. Our predictions, which include the presence of different kind of supersolids, could be of direct interest for experiments with cold Rydberg-dressed atoms in an optical lattice [121, 122]. They could also provide useful insights on the microscopic origin of the so-called superstripe phase found in lattice-based superconductors [14]. More generally, they constitute a step towards the understanding of how long-range

interactions can affect the properties of ultracold gases.

In the second chapter we studied the out-of-equilibrium scenarios of the same model investigated in Chapter 1 . This study has been carried out via simulated temperature quenches evidencing a glassy phase for strong interactions, in the same range of parameter where the corresponding equilibrium state is a normal stripe crystal. For intermediate interactions we demonstrated the presence of a metastable isotropic supersolid state which appears to be qualitatively different from the anisotropic one found in the ground state. In stark contrast with a previous study on the triangular lattice [10], no evidence of a superglass phase is found in our region of investigation. We instead demonstrated that for all interaction strength values where the out-of-equilibrium states are found to be superfluid, long range crystalline order is also present. We understood the discrepancy with the triangular lattice case in terms of the strong difference in the potential to kinetic energy ratio, which takes significantly different values on the two mentioned lattice geometries. In particular, this quantity is considerably smaller on the square lattice, signaling increased particle mobility. The latter suppresses particle and cluster localization, which is an essential ingredient for the onset of glassy physics. The physics described in this chapter should be directly relevant for experiments with ultracold Rydberg-dressed atoms confined to optical lattices [121, 122]. We hope that these results will provide new insights on the presence or absence of metastable supersolid, superglassy and glassy phases.

In the last chapter of this thesis we have investigated how the properties of long-range interacting systems are fundamentally modified when restoring energy extensivity and consequently a well-defined thermodynamic limit. We have focused our study on a one-dimensional model of hard-core bosonic particles with interactions decaying as a power-law of the distance $1/r^{\alpha}$. We found, using combination of numerical and analytical techniques, that in place of a gapped insulating phase in the absence of Kac's rescaling, the ground

state of the energy extensive, i.e. rescaled, model is an unusual metallic phase that is not described by the Luttinger liquid theory. As we shown also in Appendix B , the latter provides the correct functional behaviour for $\alpha > 0$ while it fully breaks down in the case $\alpha = 0$. Interesting prospects include the investigation of such unconventional metallic phase in higher-dimensional systems [168], and the experimental study in systems where interactions are naturally long-range and extensive, such as of cold and ultracold atoms with cavity-mediated long range interactions [68, 169].

During my Ph. D., I have collaborated with the experimental group of Prof. Kenji Ohmori[1] in the analysis of their observations regarding the ionization dynamics of ultracold Rydberg atoms. In this work, which is not featured in this thesis, we demonstrate the first step toward the realization of arrays of ultracold atoms in optical lattice excited to states where single electron wave functions spatially overlap. Such a system may be an ideal platform to simulate exotic electronic many-body phenomena in the condensed phase. In the experiment the team of Prof. Ohmori excite high-lying electronic (Rydberg) states in an atomic Mott insulator with a coherent ultrashort lasr pulse. In a regime where the Rydberg orbitals of neighboring lattice sites overlap with each other, the atoms should undergo spontaneous ionization[2]. The careful analysis of the experimental results, to which I have contributed, revealed that indeed the observations of avalanche ionization, of the formation of ultracold plasma, and of the significant differences in the ionization dynamics between a Bose-Einsten condensate and a Mott insulator, signal the actual creation of exotic electronic states with overlapping wave functions.

[1] Institute for Molecular Science, National Institutes of Natural Sciences, Okazaki, Japan
[2] Penning ionization

A

Numerical Methods

This appendix constitutes a quick overview of the numerical methods used to obtain the results shown in Chapters 1 and 2 . It is structured as follow: In Appendix A.1 we discuss the basic ideas underlying Monte Carlo methods. We use these ideas in Appendix A.2 to present the so called *worm* algorithm, a Path Integral Monte Carlo method which has the remarkable property to be numerically exact for bosonic systems on a lattice.

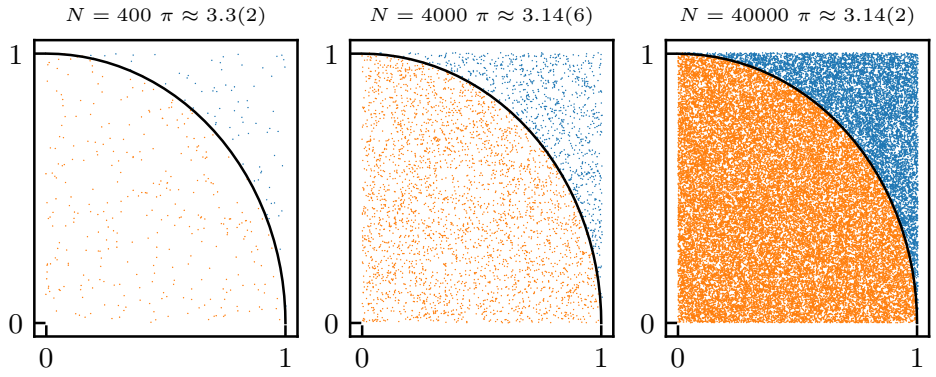

Figure A.1.: Direct sampling Monte Carlo estimation of $\pi = 3.14159\ldots$. Each point corresponds to a position sampled from an uniform distribution on the are of the square. For simplicity the evaluation is carried out only on a quarter of the area of the square and conversely of the circle. Orange points corresponds to *hits* in the circle while blue point corresponds to *misses*.

A.1 Monte Carlo methods

Monte Carlo methods are a class of computational algorithms which relies on *repeated random sampling* to provide generally approximate solutions to vast ranges of problems. These methods are usually useful in cases where analytical or numerical solutions of the problem at hand don't exist or are too difficult to implement. Numerical Monte Carlo integration of high dimensional integrals, such as appear in statistical physics and other domains, is a prime example of the strengths of this method resulting in a vast range of scientific applications.

One of the simplest examples of Monte Carlo methods consists in the estimation of the value of π via direct sampling of the ratio between the area of a square and the area of the inscribed circle. This ratio is $\pi/4$. This estimation is carried out by sampling randomly (with uniform probability distribution) a certain number N of different positions inside the square and then counting the number of times N_{hits} such points happens to hit the inscribed circle. As the number of sampled points grows the ratio between the hits and the total number of samples will approximate the ratio between the area of the circle and the square[1]. The value of π can then be estimated as

$$\pi \approx 4\frac{N_{\text{hits}}}{N}. \tag{A.1}$$

This method is referred to as *direct sampling* because of the way samples are directly generated from a probability distribution. Examples of estimations of π can be seen in Fig. A.1.

In the following we will encounter another sampling method known as *Markov Chain Monte Carlo* sampling. To simply illustrate the method we shall apply it to the problem of the evaluation of π. Starting from the center of the square we proceed moving in steps of random length and random direction, if the end position of each step is inside the circle we count it as a *hit*, otherwise as a *miss*. As we proceed moving randomly inside the square area, we can encounter cases where the sampled step would end up outside the square

[1] Jacob's Bernoulli law of large numbers.

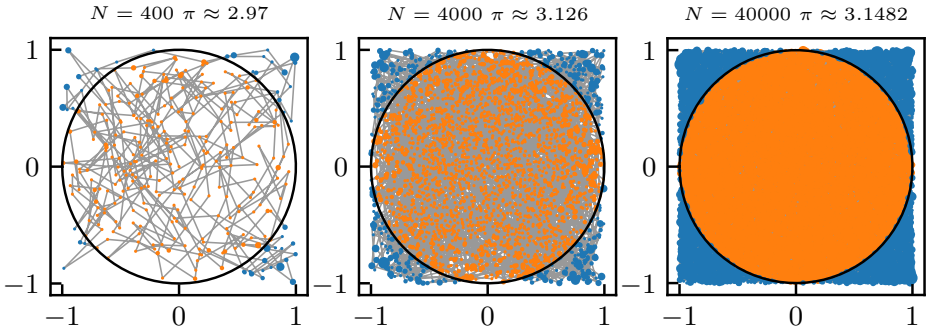

Figure A.2.: Markov Chain Monte Carlo estimation of $\pi = 3.14159\ldots$. Paths are shown as a solid line (grey) while the size of each point (blue for *misses*, orange for *hits*) is proportional to the number of times each point is sampled.

area. In these cases the step is *rejected* and the current standing position is counted again as a hit or a miss depending if it was inside or outside the circle. Examples estimations of π are shown in Fig. A.2.

The general problem these methods are called to solve is the determination of the expectation value of an observable $O(\mathbf{x})$ on a probability distribution $\pi(\mathbf{x})$. Here, for simplicity we consider $\mathbf{x}$ to be an n-dimensional vector, i.e. $\mathbf{x} \in \mathbb{R}^n$. The expectation value of the observable O is defined as

$$\langle O \rangle = \frac{\int \cdots \int O(\mathbf{x})\, \pi(\mathbf{x})\, \mathrm{d}^n\mathbf{x}}{\int \cdots \int \pi(\mathbf{x}) \mathrm{d}^n\mathbf{x}}. \tag{A.2}$$

In Monte Carlo methods such an expectation value is computed as the average over randomly sampled positions $\mathbf{x}_i$ over the probability distribution π:

$$\langle O \rangle = \lim_{m\to\infty} \sum_{i=1}^{m} O(\mathbf{x}_i). \tag{A.3}$$

The difference between direct sampling and Markov Chain Monte Carlo methods consists in how the set of samples $\{\mathbf{x}_i\}$ is generated. The first case consists in the direct generation of the samples from the probability distribution π while the latter consist in the creation of a Markov Chain having π as an equilibrium distribution. In general we can define a Markov chain on a discrete set of states S as a succession $X_1, X_2, X_3, \cdots \in S$ for which subsequent transitions $X_t \to X_{t+1}$ are statistically independent, i.e. the state X_{t+1}

depends only on the state preceding state X_t and not on the others. In order for a Markov Chain to have π as limiting equilibrium distribution it needs to satisfy two conditions:

- *Ergodicity*: any configuration $x \in S$ must be reachable from any other through a finite number of updates, in formulas

$$\forall x, y \in S \, \exists n > 0 \, : \, p^n_{x \to y} > 0 \tag{A.4}$$

  given $p^n_{x \to y}$ the probability of reaching the state y in n steps, starting from the state x.

- *Balance*:

$$\forall y \in S, \quad \sum_{x \in S} \pi(x) p_{x \to y} = \pi(y) \tag{A.5}$$

  where we have used the notation $p_{x \to y} \equiv p^1_{x \to y}$

Sometimes it is useful to impose a stronger condition other than the balance:

- *Detailed Balance*:

$$\forall x, y \in S \quad \pi(x) p_{x \to y} = \pi(y) p_{y \to x} \tag{A.6}$$

It can be shown[2] that, if a Markov Chain satisfies these conditions, then the time averages on the stochastic process will tend, as the length of the chain goes to infinity, to averages on the equilibrium distribution π.

Metropolis-Hastings algorithm In order to design a Markov Chain which satisfies these conditions, we can make use of the procedure known as the *Metropolis-Hastings* algorithm [171, 172]. This technique consists in designing a Markov Chain whose transition probabilities $p_{x \to y}$ can be split in two contributions: a *proposal probability* $g_{x \to y}$, i.e. the probability of proposing the state y given the state x, and an *acceptance ratio* $a(y, x)$, i.e. the probability to

[2] See e.g., Ref.[170]

accept the proposed state y. Accepting or rejecting a proposed transition or update $x \to y$ with probability

$$a(y, x) = \min\left(1, \frac{\pi(y) g_{y\to x}}{\pi(x) g_{x\to y}}\right) \tag{A.7}$$

automatically satisfies the detailed balance condition Eq. (A.6), and ultimately ensures, if the set of updates is ergodic, that π is the limiting distribution of the defined Markov process. In the next section Appendix A.2 the Metropolis-Hasting algorithm will constitute the basis on which the methods presented are built.

Markov Chain Monte Carlo methods are widely used in classical and quantum[3] statistical physics where one is usually interested in the computation of the expectation value of thermodynamic observables

$$\langle O \rangle = \frac{1}{\mathcal{Z}} \mathrm{Tr}\left[O \mathrm{e}^{-\beta H}\right] \qquad \mathcal{Z} = \mathrm{Tr}\left[\mathrm{e}^{-\beta H}\right] \tag{A.8}$$

where $\beta = 1/k_B T$ is the inverse temperature, k_B the Boltzmann constant, H is the Hamiltonian of the system of interest, and $\mathcal{Z}$ is the partition function.

In the following section we will introduce the Quantum Monte Carlo method that has been used to obtain many of the results presented in this thesis.

A.2 Path Integral Monte Carlo methods

The path integral Monte Carlo (PIMC) methods are a class of quantum Monte Carlo algorithms based on a *worldline* graphical representation of the partition function $\mathcal{Z}$. Without loss of generality we consider the Hamiltonian H for a system of interacting bosonic particles. This Hamiltonian can be written as a sum of a diagonal part H_0 and an off-diagonal part H_1

$$H = H_0 + H_1. \tag{A.9}$$

The starting point of the PIMC method is the decomposition of the Boltzmann factor as

$$\begin{aligned} \mathrm{e}^{-\beta H} &= \mathrm{e}^{-\beta H_0} + \\ &- \int_0^\beta \mathrm{d}t_1 \, \mathrm{e}^{-(\beta - t_1)H_0} H_1 \mathrm{e}^{-t_1 H_0} + \\ &+ \int_0^\beta \mathrm{d}t_2 \int_0^{t_2} \mathrm{d}t_1 \, \mathrm{e}^{-(\beta - t_2)H_0} H_1 \mathrm{e}^{-(t_2 - t_1)H_0} H_1 \mathrm{e}^{-t_1 H_0} - \ldots \end{aligned} \tag{A.10}$$

which in turns leads to the following expansion for the partition function

$$\begin{aligned} \mathcal{Z} = \mathrm{Tr}\left[\mathrm{e}^{-\beta H}\right] = \sum_i \underbrace{\left\langle i \middle| \mathrm{e}^{-\beta H_0} \middle| i \right\rangle}_{\text{weight}} + \\ - \sum_i \sum_{i'} \int_0^\beta \mathrm{d}t_1 \, \underbrace{\left\langle i \middle| \mathrm{e}^{-(\beta - t_1)H_0} \middle| i' \right\rangle \left\langle i' \middle| H_1 \mathrm{e}^{-t_1 H_0} \middle| i \right\rangle}_{\text{weight}} + \\ + \sum_i \sum_{i'} \sum_{i''} \ldots . \end{aligned} \tag{A.11}$$

To simplify the notation we will refer to a given sequence of n states $\{|i_1\rangle, |i_2\rangle, \ldots, |i_n\rangle\}$ and a corresponding set of times $\{t_1, \ldots, t_n\}$ as a *configuration* C_n of *order* n and to the quantity

$$W(C_n) = W(i_1, \ldots i_n, t_1, \ldots, t_n) = \left\langle i_1 \middle| \mathrm{e}^{-(\beta - t_n)H_0} \middle| i_n \right\rangle \left\langle i_n \middle| H_1 \mathrm{e}^{-(t_n - t_{n-1})H_0} \middle| i_{n-1} \right\rangle \ldots \tag{A.12}$$

as its *weight*. From these definitions it follows that the expansion of the partition function Eq. (A.11) can be seen as a sum of weights over all the possible configurations.

$$\mathcal{Z} = \sum_{n=0}^{\infty} \sum_{C_n} W(C_n). \tag{A.13}$$

A natural way to graphically represent configurations is shown in Fig. A.3 and can be easily understood by using an Extended Bose-Hubbard model as an example. The corresponding Hamiltonian decomposes as

$$H = \underbrace{\sum_{i<j} V_{ij} n_i n_j + \sum_i U_i \frac{n_i(n_i - 1)}{2}}_{H_0} - \underbrace{\sum_{i<j} t_{ij} \left(b_i^\dagger b_j + \mathrm{H.c.} \right)}_{-H_1} \tag{A.14}$$

where $b_i^\dagger$ (b_i) is the creation (annihilation) operator for bosonic particle on site i, $n_i = b_i^\dagger b_i$, t_{ij} are the hopping amplitudes, and V_{ij} and U_i are the interaction strengths.

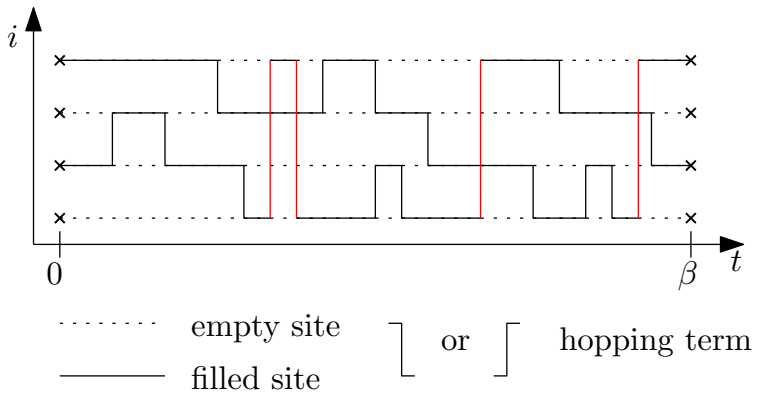

Figure A.3.: Graphical representation of a single configuration on a one dimensional lattice of 4 sites. i indicates the different lattice sites and t the imaginary time. Red vertical lines represent hopping of particles which wraps around the system.

In this case it is easy to see that the exponential terms of the form e^{-tH_0} can be interpreted as time evolution operators in *imaginary time* $t = \imath\tau$ between different states $|i\rangle$ (solid horizontal lines in Fig. A.3) while each H_1 term corresponds to the hopping of particles between different sites happening at the times $0 < t_1 < \cdots < t_n < \beta$ (vertical lines in Fig. A.3). Each continuous solid line in Fig. A.3 referred to as *worldlines* and represents the path a particle in imaginary time.

As a result of the expansion Eq. (A.13) of the partition function, the thermodynamic expectation value $\langle O \rangle$ of an observable O can be computed as

$$\langle O \rangle = \frac{1}{\mathcal{Z}} \mathrm{Tr}\left[O e^{-\beta H} \right] = \frac{1}{\mathcal{Z}} \sum_{n=0}^{\infty} \sum_{C_n} \langle O \rangle_{C_n} W(C_n) \tag{A.15}$$

where $\langle O \rangle_{C_n}$ is the imaginary-time average of the operator O for a configuration C_n.

As we have seen, Eq. (A.15) can be efficiently computed via Monte Carlo methods by sampling configurations C_n from the distribution $W(C_n)/\mathcal{Z}$. In particular, different algorithms of this class perform this sampling by implementing a Markov Chain.

Since we assume periodic boundaries on the space and imaginary time axes, configurations that *wind* across these boundaries are physical config-

urations that need to be sampled. The same is true, due to the bosonic nature of the worldlines, for particle exchanges between the states at the imaginary time boundaries. As an example the configuration in Fig. A.3 has winding number $w = 2$ given by the number of times worldlines wrap around the periodic boundaries. Since these features of the PIMC configurations are linked to the presence of superfluidity in the system, it is of crucial importance to be able to efficiently sample configurations with exchanges and different winding numbers.

A.2.1 Worm Algorithm

Introduced by Prokof'ev, Svistunov, and Tupitsyn in Ref. [5] the so-called *worm algorithm* is a scheme of performing updates of PIMC configurations. This algorithm turns out to be numerically exact[3] for bosonic systems on lattice geometries.

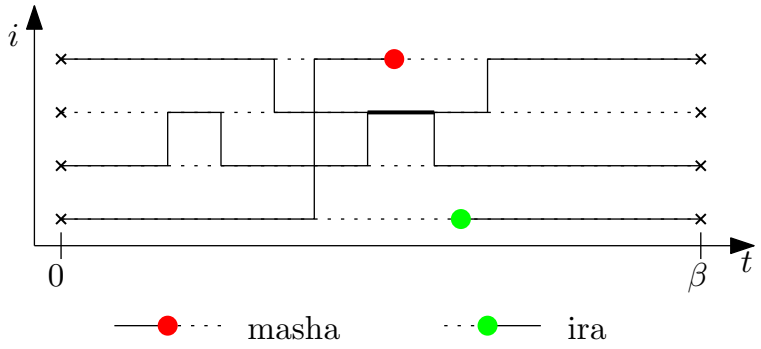

Figure A.4.: Graphical representation of an extended configuration which include the discontinuities named *Ira* (green) and *Masha* (red).

The updates that compose the worm algorithm are schematically shown in Figs. A.5(a) to A.5(d). This algorithm takes advantage of sampling in an extended space of configurations given by

$$\mathcal{G} = \mathrm{Tr}\left\{\mathcal{T}\left(b_i^\dagger(t_\mathbf{M}) b_j(t_\mathbf{I}) \mathrm{e}^{-\beta H}\right)\right\} \tag{A.16}$$

where $\mathcal{T}$ denotes the time-ordered product in imaginary time, while the cre-

[3] The uncertainity on the estimated expectation values is given only by the stochastic error due to finite sampling, which is known to decrease as $1/\sqrt{m}$ with the number m of samples.

ation and annihilation operators $b_i^\dagger(t_{\mathbf{M}})$ and $b_j(t_{\mathbf{I}})$, correspond to two discontinuities referred to as *Masha* and *Ira* respectively (see Fig. A.4).

The main working principle of the worm algorithm is to exploit the presence of the two discontinuities with updates defined in the extended space $\mathcal{G}$ in order to sample more efficiently different configurations in the $\mathcal{Z}$ space, connecting the two different sectors with a specific update. Schematically the update scheme of the worm algorithm can be summarized in few steps:

- Starting from a configuration without worldlines we try to perform the *open* update shown in Fig. A.5(a) until it is accepted. This update connects between configurations in the $\mathcal{Z}$ sector and configurations in the $\mathcal{G}$ sector.

- While the two discontinuities are present in the configuration updates defined in the $\mathcal{G}$ sector are proposed and carried out if accepted. These updates include moving heads in imaginary time (see Fig. A.5(b)), creating and deleting hopping terms while moving heads in space (see Figs. A.5(c) and A.5(d)), and removing (closing) the two discontinuities (see Fig. A.5(a)).

- If it is chosen to delete the pair of discontinuities, we transition from the $\mathcal{G}$ sector to $\mathcal{Z}$ sector. Here we can measure the expectation value of the desired observables (see Appendix A.2.2) and then start the procedure again.

A.2.2 Observables

In this subsection we list the different kind of observables which can be directly measured in PIMC methods.

Density The expectation value of diagonal operators such as the density n_j on a single site j can be easily computed on each configuration C_n as

$$n_j(C_n) = \frac{1}{\beta} \sum_{k=1}^{n} \left\langle i_k \middle| n_j \middle| i_k \right\rangle (t_k - t_{k-1}) \tag{A.17}$$

where we defined, for simplicity $t_{-1} = t_n$.

Energy The energy of a single configuration C_n is defined as the sum of potential energy and kinetic energy $E = \langle H \rangle = K + U$. While the kinetic energy is obtained by counting the number of hopping terms in a configuration (n for a configuration C_n), the potential energy is obtained as

$$U(C_n) = \frac{1}{\beta} \sum_{k=1}^{n} \langle i_k | H_0 | i_k \rangle (t_k - t_{k-1}) \tag{A.18}$$

Superfluid density Estimators for the superfluid density ρ_s strongly depend on the form of the hopping part of the Hamiltonian H_1 and on the dimensionality of the system. Different estimators are derived in detail in Ref. [9]. In the cases extensively studied in Chapters 1 and 2 , for two-dimensioal systems with nearest-neighbor uniform hopping of strength t, the superfluid density is defined as

$$\rho_s = \frac{1}{4t\beta} \left\langle W_x^2 + W_y^2 \right\rangle, \tag{A.19}$$

where W_x and W_y are the winding numbers along the two spatial dimensions of the system.

Correlation functions Density-density correlation functions of the form $S_{ij} = \left\langle n_i n_j \right\rangle$ have the estimator, given a single configuration C_n

$$S_{ij}(C_n) = \frac{1}{\beta} \sum_{k=0}^{n-1} \langle i_k | n_i | i_k \rangle \left\langle i_k \middle| n_j \middle| i_k \right\rangle (t_k - t_{k-1}) \tag{A.20}$$

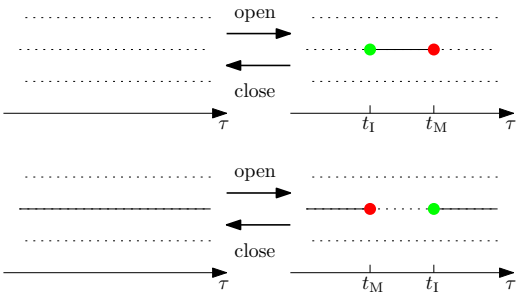

(**a**) Examples of worm pair creation and deletion in the worm algorithm.

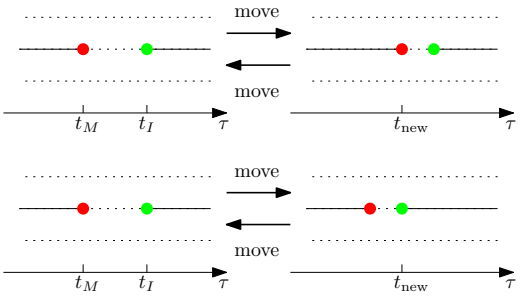

(**b**) Examples of time shifting of the two discontinuities to the new time t_k.

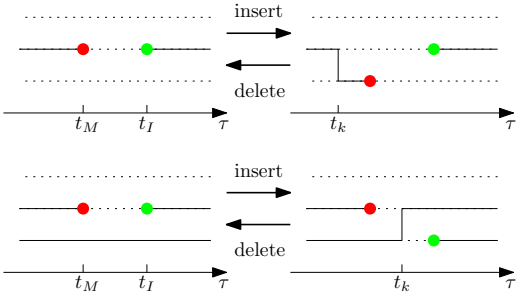

(**c**) Examples of kink creation and deletion on the left (at time t_k) of the moving head. Both heads don't change their time position.

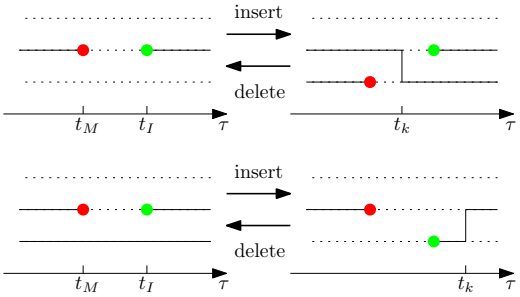

(**d**) Example of kink creation and deletion on the right (at time t_k) of the moving head. Both heads don't change their time position.

Figure A.5.: Example updates of the worm algorithm. Black arrow between configurations on the left and on the right name each each update and its inverse. In panels (b) to (d) top panels show updates involving *Masha* while bottom panels show updates involving *Ira*.

Green's function While measuring the single particle Green's function may be difficult in the majority of PIMC update schemes, in context of the worm algorithm this observable can be easily accessed. In this scheme the single particle Green's function in imaginary time is measured by evaluating the expectation value

$$G(i,j,t_1,t_2) = -\left\langle \mathcal{T}\left(b_i(t_1)b_j^\dagger(t_2)\right)\right\rangle \tag{A.21}$$

which can be easily obtained as the worm algorithm naturally samples in the extended configuration space $\mathcal{G}$.

B

Energy extensivity in quantum long-range interacting systems: effects on plasmon modes and the case $\alpha = 0$

In this chapter we extend the results obtained in Chapter 3 by showing, in Appendix B.1 that the plasmon mode of a d-dimensional system of long-range interacting fermions (or hard-core bosons) is suppressed when using the Kac prescription in the strong long-range regime $\alpha \leq d$. Also, in Appendix B.2, we solve the extreme case $\alpha = 0$ exactly using a mean-field approach showing that the system is in a free fermion phase with a charge gap $\Delta \sim (V+2\pi t)/L \to 0$ for $L \to \infty$, which is not described by the Luttinger liquid theory.

As specified in Chapter 3 this work has been carried out in collaboration with Thomas Botzung, David Hagenmuller and all the other co-authors of the publication: T. Botzung, D. Hagenmüller, G. Masella, J. Dubail, N. Defenu, A. Trombettoni, and G. Pupillo. "Effects of Energy Extensivity on the Quantum Phases of Long-Range Interacting Systems". Submitted to: Phys. Rev. Lett. *(2019). arXiv: 1909.12105, and it is also subject of T. Botzung's Ph. D. Thesis (Strasbourg, December 2019).*

B.1 Effect of energy extensivity on plasmon modes

B.1.1 One-dimensional Luttinger liquid

We consider a one-dimensional system of length L containing N fermions interacting via the long-range potential

$$V^{\alpha}(x) = \frac{V}{\left(x^2 + a^2\right)^{\alpha/2}} \qquad 0 < \alpha \leq 1. \tag{B.1}$$

Here, a denotes a short-distance cutoff that can be identified with, e.g., the lattice spacing. In the vicinity of the Fermi level, the low-energy Hamiltonian can be decomposed into the contributions of left (L) and right (R) movers as

$$H = \sum_{k} \sum_{r=\mathrm{L,R}} \hbar v_{\mathrm{F}} \left(\eta_r k - k_{\mathrm{F}}\right) c^{\dagger}_{r,k} c_{r,k} + \frac{1}{2} \int \mathrm{d}x \mathrm{d}x' \rho(x) V^{\alpha}(x - x') \rho(x'), \tag{B.2}$$

where v_{F} is the Fermi velocity, k_{F} the Fermi wave vector, $\eta_{\mathrm{R}} = +1$, $\eta_{\mathrm{L}} = -1$, and $\rho(x) = \sum_{r=\mathrm{L,R}} \rho_r(x)$ with $\rho_r(x) = \frac{1}{L} \sum_{k,q} e^{iqx} c^{\dagger}_{r,k+q} c_{r,k}$. Bosonization assumes that the low-energy properties of the Hamiltonian Eq. (B.2) are governed by the long-wavelength fluctuations of the density $\rho(x)$. Using the standard techniques described in Ref. [163], H can be approximately written (for $L \to \infty$) in the quadratic form

$$H = \frac{1}{2\pi} \sum_{q} u(q) K(q) \pi^2 \Pi(q) \Pi(-q) + \frac{u(q)}{K(q)} q^2 \phi(q) \phi(-q), \tag{B.3}$$

where $u(q)$ denotes the velocity of the excitations and $K(q)$ is the Luttinger parameter governing the decay of correlations at long distances. The latter satisfy the relations

$$u(q) K(q) = v_{\mathrm{F}} \tag{B.4}$$

$$\frac{u(q)}{K(q)} = v_{\mathrm{F}} \left[1 + \frac{V^{(\alpha)}(q)}{\pi v_{\mathrm{F}}}\right]. \tag{B.5}$$

The Fourier transform of the interaction potential reads

$$V^{\alpha}(q) = \int \mathrm{d}x \, V^{\alpha}(x) e^{-iqx} = V \frac{2\sqrt{\pi}}{\Gamma\left(\frac{\alpha}{2}\right) 2^{\frac{\alpha-1}{2}}} \left(\frac{|q|}{a}\right)^{\frac{\alpha-1}{2}} \mathcal{K}_{\frac{\alpha-1}{2}}(a|q|), \tag{B.6}$$

and the two fields $\Pi(q) = \int \mathrm{d}x\, \Pi(x) e^{-iqx}$ and $\phi(q) = \int \mathrm{d}x\, \phi(x) e^{-iqx}$ are the Fourier transforms of the canonically conjugate fields $\Pi(x) = \frac{1}{\pi} \div \theta(x)$ and $\phi(x)$ with

$$\phi(x) = -(N_\mathrm{R} + N_\mathrm{L}) \frac{\pi x}{L} - \frac{\mathrm{i}\pi}{L} \sum_{q \neq 0} \frac{1}{q} e^{-\beta|q|/2 - \mathrm{i}qx} \left(\rho_\mathrm{R}(q) + \rho_\mathrm{L}(q)\right) \tag{B.7}$$

$$\theta(x) = (N_\mathrm{R} - N_\mathrm{L}) \frac{\pi x}{L} + \frac{\mathrm{i}\pi}{L} \sum_{q \neq 0} \frac{1}{q} e^{-\beta|q|/2 - \mathrm{i}qx} \left(\rho_\mathrm{R}(q) - \rho_\mathrm{L}(q)\right). \tag{B.8}$$

Here, β is a (small) cutoff regularizing the theory, $N_r = \sum_k c^\dagger_{r,k} c_{r,k} - \langle c^\dagger_{r,k} c_{r,k} \rangle$, and $\rho_r(q) = \sum_k c^\dagger_{r,k+q} c_{r,k}$. The plasmon dispersion relation follows from Eq. (B.4) and reads

$$\omega(q) = u(q)|q| = v_\mathrm{F}|q| \sqrt{1 + \frac{V^{(\alpha)}(q)}{\pi v_\mathrm{F}}}. \tag{B.9}$$

The potential Eq. (B.6) exhibits a long-wavelength divergence ($q \to 0$), namely $V^\alpha(q) \sim |q|^{\alpha - 1}$ for $0 < \alpha < 1$ and $V^\alpha(q) \sim \log|q|$ for $\alpha = 1$. In the latter case, Eq. (B.9) provides the 1D plasmon dispersion $\omega(q) \sim |q|\sqrt{\log|q|}$ stemming from Coulomb interactions [144]. When rescaling the interaction potential by the Kac's factor $\Lambda_\alpha(L) = L^{1-\alpha}$ for $0 \leq \alpha < 1$ and $\Lambda_\alpha(L) = \log(L)$ for $\alpha = 1$, it is easy to check that the long-wavelength divergence of the potential is removed by considering the limit $q = \frac{2\pi}{L} \to 0$. As a consequence, one recovers the sound wave dispersion relation $\omega(q) \sim |q|$ of a metal with short-range interactions. This result is confirmed by looking at the upper bound of the excitation spectrum $\Omega(q) = E(q)/S(q)$ in the Feynman approximation [173] represented in Fig. B.1, where $E(q) = (t/L)\left[1 - \cos(q)\right] \langle \sum_i a^\dagger_i a_{i+1} + \mathrm{h.c.} \rangle$ and $S(q)$ is the structure factor defined by Eq. (3.14) .

B.1.2 Generalization to higher dimensions

This result can be easily generalized to higher dimensions $d = 2, 3$ by looking at the zeros of the dielectric function in the framework of the random phase approximation (RPA):

$$\epsilon(\mathbf{q}, \omega) = 1 - \chi(\mathbf{q}, \omega) V^\alpha(\mathbf{q}) = 0, \tag{B.10}$$

where

$$\chi(\mathbf{q}, \omega) = \frac{1}{\mathcal{V}} \sum_{\mathbf{k}} \frac{n_\mathbf{k} - n_{\mathbf{k}+\mathbf{q}}}{\hbar\omega + E_\mathbf{k} - E_{\mathbf{k}+\mathbf{q}} + \mathrm{i}\eta} \tag{B.11}$$

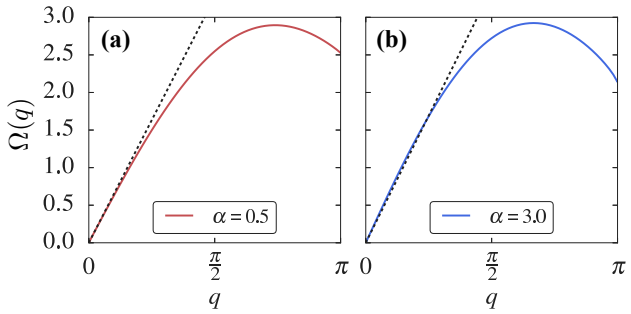

Figure B.1.: Upper bound of the excitation spectrum $\Omega(q)$ (in units of t) in the Feynman approximation (colored lines) computed at half-filling for $V = 0.5$ in the strong long-range regime $\alpha = 0.5$ panel (a), and in the short-range case $\alpha = 3$ panel (b). The dispersion relation Eq. (B.9) after Kac's rescaling, namely $\omega(q) = v_F q\sqrt{1 + V/\pi}$ for $\alpha = 0.5$ and $\omega(q) = v_F q\sqrt{1 + V/(\sqrt{\pi}\Gamma(3/2)v_F)}$ for $\alpha = 3$ is represented as a black dotted line in the long-wavelength regime $q \to 0$. The proximity of the Mott transition ($V = 2$ for $\alpha \to \infty$) in the short-range case is responsible for the more pronounced minimum at $q = \pi$ (charge density wave).

denotes the one-spin density-density response function (Lindhard function), $\mathcal{V}$ the volume, and $n_{\mathbf{k}}$ the occupation number of a state with wave vector $\mathbf{k}$ and energy $E_{\mathbf{k}} = \frac{\hbar^2|\mathbf{k}|^2}{2m}$ (m is the particle mass). For $\alpha = 1$, the Fourier transform of the Coulomb potential is

$$\begin{aligned} V^1(q) &\sim \log|q| && d = 1 \\ V^1(\mathbf{q}) &\sim \frac{1}{|\mathbf{q}|} && d = 2 \\ V^1(\mathbf{q}) &\sim \frac{1}{|\mathbf{q}|^2} && d = 3. \end{aligned} \tag{B.12}$$

In the dynamical limit $\omega \gg |\mathbf{q}|v_F$, the Lindhard function can be approximated by $\chi(\mathbf{q}, \omega) = \frac{\rho_0|\mathbf{q}|^2}{m\omega^2}$ with ρ_0 the average fermion density. Using this expression together with Eq. (B.12) into Eq. (B.10), one finds the plasmon energies

$$\omega \sim |q|\sqrt{\log|q|} \qquad d = 1 \tag{B.13}$$

$$\omega \sim \sqrt{|\mathbf{q}|} \qquad d = 2 \tag{B.14}$$

$$\omega \sim \text{cst} \qquad d = 3. \tag{B.15}$$

When using the Kac's prescription, namely dividing the potential by the factor L^{d-1}, the long-wavelength divergence ($q = \frac{2\pi}{L} \to 0$) is removed and one recovers the sound wave dispersion relation $\omega \sim |\mathbf{q}|$ for $d = 1, 2, 3$.

B.2 The extreme case $\alpha = 0$

The particular case $\alpha = 0$ can be solved exactly using a mean field approach on the Hamiltonian Eq. (3.1) . For convenience, we use fermions instead of hard-core bosons since the results are equivalent in both cases. We start from the Hamiltonian

$$H = -t \sum_{i=0}^{L-1} \left(c_i^\dagger c_{i+1} + \text{h.c.} \right) + \frac{V}{2} \sum_{i \neq j} n_i n_j, \tag{B.16}$$

where c_i ($c_i^\dagger$) annihilates (creates) a fermion on site $i = 1, \cdots, L$, and $n_i = c_i^\dagger c_i$ is the local density. Writting the density-density interaction as $n_i n_j \approx n_i \langle n_j \rangle + n_j \langle n_i \rangle - \langle n_i \rangle \langle n_j \rangle$, the mean-field Hamiltonian reads

$$H_{\text{mf}} = \sum_k \left[(N-1)\, V - 2t \cos(k) \right] c_k^\dagger c_k - \frac{N(N-1)\, V}{2}, \tag{B.17}$$

with $N = L/2$ the number of fermions (at half-filling), and $c_k = \frac{1}{\sqrt{L}} \sum_{j=0}^{L-1} c_j e^{-2i\pi kj/L}$. The energy of the ground state for, e.g., N even, is derived from Eq. (B.17) with anti-periodic boundary conditions as

$$E_0(N) = \frac{N(N-1)\, V}{2} - 2t \sum_{k=-L/4}^{L/4-1} \cos\left[\frac{2\pi k}{L} + \left(\frac{\pi}{L} \right) \right] = \frac{N(N-1)\, V}{2} - 2t \csc\left(\frac{\pi}{L} \right). \tag{B.18}$$

One then has to consider periodic boundary conditions for $N \pm 1$ fermions, which leads to

$$\begin{aligned} E_0(N+1) &= \frac{(N+1)\, NV}{2} - 2t \sum_{k=-L/4}^{L/4} \cos\left(\frac{2\pi k}{L} \right) \\ &= \frac{(N+1)\, NV}{2} - 2t \cot\left(\frac{\pi}{L} \right) \end{aligned} \tag{B.19}$$

$$\begin{aligned} E_0(N-1) &= \frac{(N-1)\,(N-2)\, V}{2} - 2t \sum_{k=-L/4+1}^{L/4-1} \cos\left(\frac{2\pi k}{L} \right) \\ &= \frac{(N-1)\,(N-2)\, V}{2} - 2t \cot\left(\frac{\pi}{L} \right). \end{aligned} \tag{B.20}$$

The charge gap thus reads $\Delta \equiv E_0(N+1) + E_0(N-1) - 2E_0(N) = V + 4t \tan\left(\frac{\pi}{2L} \right)$, and becomes $\Delta \sim (V + 2\pi t)/L \to 0$ for $L \to \infty$ when using the

Kac's prescription $V \to V/L$. The Luttinger parameters u/K and uK can be related to the first derivative of the single-particle charge gap as $\frac{\partial \Delta}{\partial(1/L)} = \pi \frac{u}{K}$, and to the charge stiffness [163] as

$$D = \pi L \left| \frac{\partial^2 E_0(N, \Phi)}{\partial \Phi^2} \right|_{\Phi=0} = uK. \tag{B.21}$$

Here, $\Phi = 2\pi\phi/\phi_0$ denotes a flux threading the (circular) chain in units of the flux quantum $\phi_0 = h/e$. This flux can be taken into account by multiplying the hopping energy by an Aharonov-Bohm phase phase $e^{\pm i\Phi/L}$ as

$$H(\Phi) = -t \sum_{i=0}^{L-1} \left(e^{i\Phi/L} c_i^\dagger c_{i+1} + \text{h.c.} \right) + \frac{V}{2} \sum_{i \neq j} n_i n_j. \tag{B.22}$$

The energy of the Hartree-Fock ground state is derived as

$$E_0(N, \Phi) = \frac{N(N-1)V}{2} - 2t \csc\left(\frac{\pi}{L}\right) \cos\left(\frac{\Phi}{L}\right), \tag{B.23}$$

which provides $D = 2t = v_F$ for $L \to \infty$. The Luttinger parameters extracted from the charge gap and from the charge stiffness thus read

$$uK = v_F \tag{B.24}$$

$$\frac{u}{K} = v_F \left[1 + \frac{V}{\pi v_F} \right], \tag{B.25}$$

and coincide exactly with the analytic prediction Eq. (3.11) . Since the mean-field Hamiltonian Eq. (B.17) corresponds to that of free fermions up to a constant shift $\propto V$, it is straightforward to calculate the Luttinger parameter K from the single-particle correlation function

$$\langle c_i^\dagger c_j \rangle = \frac{1}{L} \sum_k e^{ik(i-j)} n_k = \frac{1}{2i\pi} \frac{e^{ik_F(i-j)}}{i-j} \sim (i-j)^{-1}, \tag{B.26}$$

and from the long-wavelength limit of the static structure factor

$$\begin{aligned} S(q) &\equiv \frac{1}{L} \sum_{i,j} e^{iq(i-j)} \left(\left\langle n_i n_j \right\rangle - \langle n_i \rangle \left\langle n_j \right\rangle \right) = \\ &= \frac{1}{L} \sum_{k,k'} \left(\left\langle c_k^\dagger c_{k-q} c_{k'}^\dagger c_{k'+q} \right\rangle - \left\langle c_k^\dagger c_{k-q} \right\rangle \left\langle c_{k'}^\dagger c_{k'+q} \right\rangle \right) \to_{q \to 0} \frac{1}{L}. \end{aligned} \tag{B.27}$$

Note that the only non-vanishing contribution to the last equation stems from the term $\propto \langle c_k^\dagger c_{k'+q} \rangle \langle c_{k-q} c_{k'}^\dagger \rangle$, which is finite only at the two edges of the Fermi

sea where $n_k = 1/2$. Comparing Eqs. (B.26) and (B.27) to the predictions $\langle c_i^\dagger c_j \rangle \sim (i-j)^{-\frac{K+(1/K)}{2}}$ (for fermions) and $K = LS(q \to 0)$ of the Luttinger liquid theory, we thus find $K = 1$ for all V in disagreement with the result $K = 1/\sqrt{1 + V/(\pi v_{\mathrm{F}})}$ obtained from Eq. (B.24). This suggests a breakdown of the Luttinger liquid theory in the extreme case $\alpha = 0$.

C

Extended-range interactions with Rydberg atoms

Excited atoms, with high principal quantum number n are known as Rydberg atoms. The main peculiar properties of Rydberg atoms have been described in many books and reviews (see, e.g. [174]) but here we are interested in the large polarizability $\sim n^7$ which ultimately leads to strong interactions between such atoms, and long lifetimes scaling as n^3 which makes them ideal for exploring many-body physics. In absence of external electric field the interactions between Rydberg atoms is of *van der Waals* type $\sim C_6/r^6$ [175, 176], where the characteristic coupling constant C_6 scales as $\sim n^{11}$.

The large number of application of Rydberg atoms in the fields of quantum simulation [177, 178, 179, 180], or quantum computing [181], relies on an interesting phenomenon occurring when optically exciting multiple atoms from their ground state $|g\rangle$ to an excited Rydberg state $|e\rangle$. If two atoms are in their Rydberg states (e.g. $|ee\rangle$) they interact via van der Waals forces and the energy levels shift with respect to the non interacting case (i.e., for very large distance $r \to \infty$ between the two atoms). When the interaction energy becomes large enough (i.e., for small r) the laser used to drive the excitation becomes off-resonant with the transition coupling the singly with the doubly excited state (e.g., $|ge\rangle \to |ee\rangle$) and only one excitation is allowed in the system [see, Fig. C.1]. This phenomenon is known as *dipole blockade* or as *Rydberg*

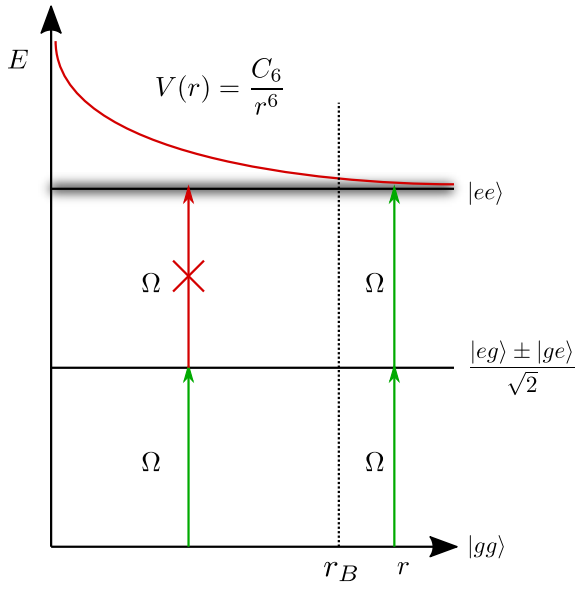

Figure C.1.: Representation of the dipole blockade: due to the shift cause by the (*van der Waals*) interaction between two Rydberg-excited atoms, the formation of a doubly excited pair is forbidden. The blockade effect extends within a blockade radius, that depends on the parameters of the excitation process.

blockade in the case of Rydberg atoms [181, 182, 183, 184, 175]. A minimal distance at which two excitation can be created with a resonant laser radiation can be defined as a function of the parameters of the excitation process, namely the Rabi frequency Ω and reads

$$r_b = \left(\frac{|C_6|}{\Omega}\right)^{\frac{1}{6}} \tag{C.1}$$

In the case of *far off-resonant* regime, where the excitation laser radiation is detuned by $\Delta \gg \Omega$, atoms can be engineered in a weak admixture of the ground state and the excited Rydberg state. These so called *Rydberg-dressed* states, which can be written as

$$|g\rangle + \alpha\,|e\rangle \qquad \alpha = \frac{\Omega}{2\Delta} \tag{C.2}$$

have different properties with respect to the Rydberg excited states $|e\rangle$, e.g., a longer lifetime ($\tau_{\text{Dressed}}/\tau_{\text{Rydberg}} \sim \alpha^{-2}$). Here we are interested in the peculiar shape of the interaction between Rydberg dressed atoms. It can be shown

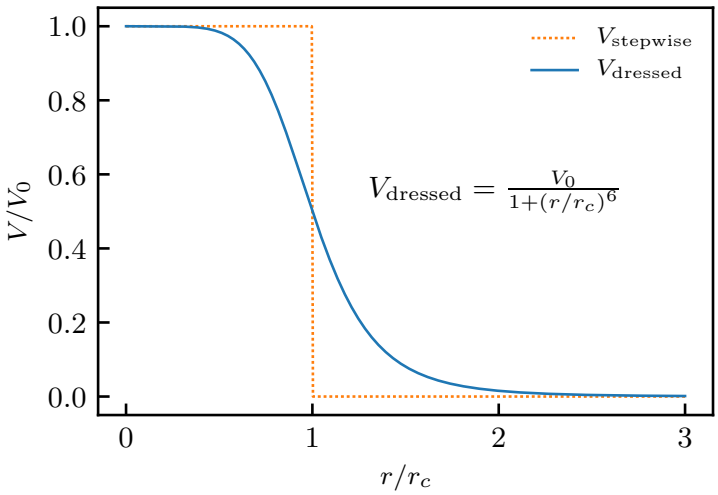

Figure C.2.: Interaction potential between Rydberg-dressed atoms as a function of the distance r.

[71, 114, 73] that the potential between two Rydberg-dressed atoms takes the form

$$V_{dd}(r) = \frac{V_0}{1 + \left(\frac{r}{r_c}\right)^6} \qquad V_0 = \frac{\Omega^4}{8\Delta^3}, r_c = \left(\frac{C_6}{2|\Delta|}\right)^{\frac{1}{6}}. \tag{C.3}$$

As shown in Fig. C.2, the potential Eq. (C.3) is characterized by a flat plateau up to the distance r_c and by a tail $\sim 1/r^6$.

List of Figures

List of Tables

Abbreviations

DMRG Density Matrix Renormalization Group. 46, 49

DMRG density matrix renormalization group. x, xiii

EF état fondamental. xii–xiv, 87

ERI interaction repoussante à portée étendue (extended-range repulsive interactions. xi, xiv

HE hors d'équilibre. xii–xiv

IS supersolide isotrope (isotropic supersolid). xii, xiii, 87

IS isotropic supersolid. 17–21, 25–27, 37, 38, 40, 88

PIMC Monte Carlo de intégrale de chemin (path integral Monte Carlo). x, xii

PIMC path integral Monte Carlo. 67, 68, 70, 72, 74

QMC Monte Carlo quantique (Quantum Monte Carlo). x

QMC quantum Monte Carlo. 38

SC cristal à bandes (stripe crystal). xii, xiii, 87

SC stripe crystal. 17, 20, 21, 24–27, 35, 38

SF superfluide. xiii, 87

SF superfluid. 16, 19–21, 35, 37, 38

SS supersolide anisotrope à bande (anisotropic stripe supersolid). xii, xiii, 87

SS anisotropic stripe supersolid. 17–27, 35, 38, 40, 41, 88

Bibliography

[1] I. Bloch, J. Dalibard, and W. Zwerger. "Many-Body Physics with Ultracold Gases". In: *Rev. Mod. Phys.* 80.3 (July 18, 2008), pp. 885–964. DOI: 10.1103/RevModPhys.80.885.

[2] C. Gross and I. Bloch. "Quantum Simulations with Ultracold Atoms in Optical Lattices". In: *Science* 357.6355 (Sept. 8, 2017), pp. 995–1001. DOI: 10.1126/science.aal3837. pmid: 28883070.

[3] A. W. Sandvik. "Computational Studies of Quantum Spin Systems". In: *AIP Conf. Proc.* 1297.1 (Nov. 3, 2010), pp. 135–338. DOI: 10.1063/1.3518900.

[4] D. M. Ceperley. "Path Integrals in the Theory of Condensed Helium". In: *Rev. Mod. Phys.* 67.2 (Apr. 1, 1995), pp. 279–355. DOI: 10.1103/RevModPhys.67.279.

[5] N. V. Prokof'ev, B. V. Svistunov, and I. S. Tupitsyn. "Exact, Complete, and Universal Continuous-Time Worldline Monte Carlo Approach to the Statistics of Discrete Quantum Systems". In: *J. Exp. Theor. Phys.* 87.2 (Aug. 1, 1998), pp. 310–321. DOI: 10.1134/1.558661.

[6] U. Schollwöck. "The Density-Matrix Renormalization Group in the Age of Matrix Product States". In: *Ann. Phys.* January 2011 Special Issue 326.1 (Jan. 1, 2011), pp. 96–192. DOI: 10.1016/j.aop.2010.09.012.

[7] M. Boninsegni and N. V. Prokof'ev. "Colloquium: Supersolids: What and Where Are They?" In: *Rev. Mod. Phys.* 84.2 (May 11, 2012), pp. 759–776. DOI: 10.1103/RevModPhys.84.759.

[8] L. Tanzi et al. "Observation of a Dipolar Quantum Gas with Metastable Supersolid Properties". In: *Phys. Rev. Lett.* 122.13 (Apr. 3, 2019), p. 130405. DOI: 10.1103/PhysRevLett.122.130405.

[9] V. G. Rousseau. "Superfluid Density in Continuous and Discrete Spaces: Avoiding Misconceptions". In: *Phys. Rev. B* 90.13 (Oct. 1, 2014), p. 134503. DOI: 10.1103/PhysRevB.90.134503.

[10] A. Angelone, F. Mezzacapo, and G. Pupillo. "Superglass Phase of Interaction-Blockaded Gases on a Triangular Lattice". In: *Phys. Rev. Lett.* 116.13 (Apr. 1, 2016), p. 135303. DOI: 10.1103/PhysRevLett.116.135303.

[11] A. Macia et al. "Excitations and Stripe Phase Formation in a Two-Dimensional Dipolar Bose Gas with Tilted Polarization". In: *Phys. Rev. Lett.* 109.23 (Dec. 5, 2012), p. 235307. DOI: 10.1103/PhysRevLett.109.235307.

[12] R. Bombin, J. Boronat, and F. Mazzanti. "Dipolar Bose Supersolid Stripes". In: *Phys. Rev. Lett.* 119.25 (Dec. 20, 2017), p. 250402. DOI: 10.1103/PhysRevLett.119.250402.

[13] G. G. Batrouni and R. T. Scalettar. "Phase Separation in Supersolids". In: *Phys. Rev. Lett.* 84.7 (Feb. 14, 2000), pp. 1599–1602. DOI: 10.1103/PhysRevLett.84.1599.

[14] A. Bianconi, D. Innocenti, and G. Campi. "Superstripes and Superconductivity in Complex Granular Matter". In: *J. Supercond. Nov. Magn.* 26.8 (Aug. 1, 2013), pp. 2585–2588. DOI: 10.1007/s10948-013-2229-x.

[15] M. Kac, G. E. Uhlenbeck, and P. C. Hemmer. "On the van Der Waals Theory of the Vapor-Liquid Equilibrium. I. Discussion of a One-Dimensional Model". In: *J. Math. Phys.* 4.2 (Feb. 1, 1963), pp. 216–228. DOI: 10.1063/1.1703946.

[16] S. Capponi, D. Poilblanc, and T. Giamarchi. "Effects of Long-Range Electronic Interactions on a One-Dimensional Electron System". In: *Phys. Rev. B* 61.20 (May 15, 2000), pp. 13410–13417. DOI: 10.1103/PhysRevB.61.13410.

[17] G. Masella et al. “Supersolid Stripe Crystal from Finite-Range Interactions on a Lattice”. In: *Phys. Rev. Lett.* 123.4 (July 26, 2019), p. 045301. DOI: 10.1103/PhysRevLett.123.045301.

[18] A. Angelone et al. “Non-Equilibrium Scenarios in Cluster-Forming Quantum Lattice Models”. Submitted to: *Phys. Rev.A* (2019). arXiv: 1606.04267.

[19] T. Botzung et al. “Effects of Energy Extensivity on the Quantum Phases of Long-Range Interacting Systems”. Submitted to: *Phys. Rev. Lett.* (2019). arXiv: 1909.12105.

[20] M. Mizoguchi et al. “Ultrafast Creation of Overlapping Rydberg Electrons in an Atomic BEC and Mott-Insulator Lattice”. Submitted to: *Science* (2019). arXiv: 1910.05292.

[21] P. W. Anderson. “More Is Different”. In: *Science* 177.4047 (Aug. 4, 1972), pp. 393–396. DOI: 10.1126/science.177.4047.393. pmid: 17796623.

[22] J. Bardeen, L. N. Cooper, and J. R. Schrieffer. “Theory of Superconductivity”. In: *Phys. Rev.* 108.5 (Dec. 1, 1957), pp. 1175–1204. DOI: 10.1103/PhysRev.108.1175.

[23] A. J. Leggett. “Superfluidity”. In: *Rev. Mod. Phys.* 71.2 (Mar. 1, 1999), S318–S323. DOI: 10.1103/RevModPhys.71.S318.

[24] J. F. Annett. *Superconductivity, Superfluids and Condensates*. Oxford Master Series in Physics. Oxford, New York: Oxford University Press, Mar. 25, 2004. 200 pp.

[25] B. V. Svistunov, E. Babaev, and N. V. Prokof’ev. *Superfluid States of Matter*. 1st. CRC Press, Apr. 15, 2015.

[26] F. London. *Superfluids*. Wiley, 1950. 184 pp.

[27] R. P. Feynman. “Superfluidity and Superconductivity”. In: *Rev. Mod. Phys.* 29.2 (Apr. 1, 1957), pp. 205–212. DOI: 10.1103/RevModPhys.29.205.

[28] E. L. Andronikashvili. “Investigation of the Viscosity of the Normal Component of Helium II”. In: *J. Exp. Theor. Phys.* 18 (1948), p. 429.

[29] A. J. Leggett. *Quantum Liquids: Bose Condensation and Cooper Pairing in Condensed-Matter Systems*. Oxford Graduate Texts. Oxford, New York: Oxford University Press, Sept. 28, 2006. 408 pp.

[30] A. F. Andreev and I. M. Lifshitz. "Quantum Theory of Defects in Crystals". In: *Soviet Phys JETP* 29.6 (1969), p. 2057.

[31] G. V. Chester. "Speculations on Bose-Einstein Condensation and Quantum Crystals". In: *Phys. Rev. A* 2.1 (July 1, 1970), pp. 256–258. DOI: 10.1103/PhysRevA.2.256.

[32] J. M. Goodkind. "Interaction of First and Second Sound in Solid ${\mathrm{4}}\mathr
Properties of a Possible Bose Condensate". In: *Phys. Rev. Lett.* 89.9 (Aug. 9, 2002), p. 095301. DOI: 10.1103/PhysRevLett.89.095301.

[33] E. Kim and M. H. W. Chan. "Probable Observation of a Supersolid Helium Phase". In: *Nature* 427.6971 (Jan. 2004), pp. 225–227. DOI: 10.1038/nature02220.

[34] E. Kim and M. H. W. Chan. "Observation of Superflow in Solid Helium". In: *Science* 305.5692 (Sept. 24, 2004), pp. 1941–1944. DOI: 10.1126/science.1101501. pmid: 15345778.

[35] M. Boninsegni, N. Prokof'ev, and B. Svistunov. "Superglass Phase of ^{4}He". In: *Phys. Rev. Lett.* 96.10 (Mar. 16, 2006), p. 105301. DOI: 10.1103/PhysRevLett.96.105301.

[36] B. K. Clark and D. M. Ceperley. "Off-Diagonal Long-Range Order in Solid ${4}\mathrm{He}$". In: *Phys. Rev. Lett.* 96.10 (Mar. 16, 2006), p. 105302. DOI: 10.1103/PhysRevLett.96.105302.

[37] R. Rota and J. Boronat. "Path Integral Monte Carlo Calculation of Momentum Distribution in Solid 4He". In: *J Low Temp Phys* 162.3 (Feb. 1, 2011), pp. 146–153. DOI: 10.1007/s10909-010-0249-5.

[38] D. E. Galli and L. Reatto. "Solid 4He and the Supersolid Phase: From Theoretical Speculation to the Discovery of a New State of Matter? –A Review of the Past and Present Status of Research–". In: *J. Phys. Soc. Jpn.* 77.11 (Nov. 10, 2008), p. 111010. DOI: 10.1143/JPSJ.77.111010.

[39] M. Boninsegni, N. V. Prokof'ev, and B. V. Svistunov. "Worm Algorithm and Diagrammatic Monte Carlo: A New Approach to Continuous-Space Path Integral Monte Carlo Simulations". In: *Phys. Rev. E* 74.3 (Sept. 1, 2006), p. 036701. DOI: 10.1103/PhysRevE.74.036701.

[40] J. Day and J. Beamish. "Low-Temperature Shear Modulus Changes in Solid 4 He and Connection to Supersolidity". In: *Nature* 450.7171 (Dec. 2007), pp. 853–856. DOI: 10.1038/nature06383.

[41] D. Y. Kim and M. H. W. Chan. "Absence of Supersolidity in Solid Helium in Porous Vycor Glass". In: *Phys. Rev. Lett.* 109.15 (Oct. 8, 2012), p. 155301. DOI: 10.1103/PhysRevLett.109.155301.

[42] M. H. Anderson et al. "Observation of Bose-Einstein Condensation in a Dilute Atomic Vapor". In: *Science* 269.5221 (July 14, 1995), pp. 198–201. DOI: 10.1126/science.269.5221.198. pmid: 17789847.

[43] *The Nobel Prize in Physics 2001*. URL: https://www.nobelprize.org/prizes/physics/2001/cornell/lecture/ (visited on 10/22/2019).

[44] C. Chin et al. "Feshbach Resonances in Ultracold Gases". In: *Rev. Mod. Phys.* 82.2 (Apr. 29, 2010), pp. 1225–1286. DOI: 10.1103/RevModPhys.82.1225.

[45] P. O. Fedichev et al. "Influence of Nearly Resonant Light on the Scattering Length in Low-Temperature Atomic Gases". In: *Phys. Rev. Lett.* 77.14 (Sept. 30, 1996), pp. 2913–2916. DOI: 10.1103/PhysRevLett.77.2913.

[46] N. Sándor et al. "Rydberg Optical Feshbach Resonances in Cold Gases". In: *Phys. Rev. A* 96.3 (Sept. 28, 2017), p. 032719. DOI: 10.1103/PhysRevA.96.032719.

[47] O. Thomas et al. "Experimental Realization of a Rydberg Optical Feshbach Resonance in a Quantum Many-Body System". In: *Nature Communications* 9.1 (June 8, 2018), p. 2238. DOI: 10.1038/s41467-018-04684-w.

[48] T. Lahaye et al. "The Physics of Dipolar Bosonic Quantum Gases". In: *Rep. Prog. Phys.* 72.12 (2009), p. 126401. DOI: 10.1088/0034-4885/72/12/126401.

[49] M. Schmitt et al. "Self-Bound Droplets of a Dilute Magnetic Quantum Liquid". In: *Nature* 539.7628 (Nov. 2016), pp. 259–262. DOI: 10.1038/nature20126.

[50] L. Chomaz et al. "Observation of Roton Mode Population in a Dipolar Quantum Gas". In: *Nature Physics* 14.5 (May 2018), pp. 442–446. DOI: 10.1038/s41567-018-0054-7.

[51] V. D. Vaidya et al. "Tunable-Range, Photon-Mediated Atomic Interactions in Multimode Cavity QED". In: *Phys. Rev. X* 8.1 (Jan. 8, 2018), p. 011002. DOI: 10.1103/PhysRevX.8.011002.

[52] S. Lepoutre et al. "Collective Spin Modes of a Trapped Quantum Ferrofluid". In: *Phys. Rev. Lett.* 121.1 (July 5, 2018), p. 013201. DOI: 10.1103/PhysRevLett.121.013201.

[53] E. Lucioni et al. "Dysprosium Dipolar Bose-Einstein Condensate with Broad Feshbach Resonances". In: *Phys. Rev. A* 97.6 (June 29, 2018), 060701(R). DOI: 10.1103/PhysRevA.97.060701.

[54] L. D. Carr et al. "Cold and Ultracold Molecules: Science, Technology and Applications". In: *New J. Phys.* 11.5 (2009), p. 055049. DOI: 10.1088/1367-2630/11/5/055049.

[55] D. S. Jin and J. Ye. "Introduction to Ultracold Molecules: New Frontiers in Quantum and Chemical Physics". In: *Chem. Rev.* 112.9 (Sept. 12, 2012), pp. 4801–4802. DOI: 10.1021/cr300342x.

[56] M. Saffman, T. G. Walker, and K. Mølmer. "Quantum Information with Rydberg Atoms". In: *Rev. Mod. Phys.* 82.3 (Aug. 18, 2010), pp. 2313–2363. DOI: 10.1103/RevModPhys.82.2313.

[57] R. Löw et al. "An experimental and theoretical guide to strongly interacting Rydberg gases". In: *J. Phys. B: At. Mol. Opt. Phys.* 45.11 (2012), p. 113001. DOI: 10.1088/0953-4075/45/11/113001.

[58] M. Marinescu and L. You. "Controlling Atom-Atom Interaction at Ultralow Temperatures by Dc Electric Fields". In: *Phys. Rev. Lett.* 81.21 (Nov. 23, 1998), pp. 4596–4599. DOI: 10.1103/PhysRevLett.81.4596.

[59] S. Yi and L. You. "Trapped Atomic Condensates with Anisotropic Interactions". In: *Phys. Rev. A* 61.4 (Mar. 13, 2000), p. 041604. DOI: 10.1103/PhysRevA.61.041604.

[60] S. Yi and L. You. "Trapped Condensates of Atoms with Dipole Interactions". In: *Phys. Rev. A* 63.5 (Apr. 18, 2001), p. 053607. DOI: 10.1103/PhysRevA.63.053607.

[61] J. W. Britton et al. "Engineered two-dimensional Ising interactions in a trapped-ion quantum simulator with hundreds of spins". In: *Nature* 484.7395 (Apr. 2012), pp. 489–492. DOI: 10.1038/nature10981.

[62] A. Bermudez, T. Schaetz, and M. B. Plenio. "Dissipation-Assisted Quantum Information Processing with Trapped Ions". In: *Phys. Rev. Lett.* 110.11 (Mar. 14, 2013), p. 110502. DOI: 10.1103/PhysRevLett.110.110502.

[63] P. Richerme et al. "Non-Local Propagation of Correlations in Quantum Systems with Long-Range Interactions". In: *Nature* 511.7508 (July 2014), pp. 198–201. DOI: 10.1038/nature13450.

[64] P. Jurcevic et al. "Quasiparticle Engineering and Entanglement Propagation in a Quantum Many-Body System". In: *Nature* 511.7508 (July 2014), pp. 202–205. DOI: 10.1038/nature13461.

[65] S. John and J. Wang. "Quantum Electrodynamics near a Photonic Band Gap: Photon Bound States and Dressed Atoms". In: *Phys. Rev. Lett.* 64.20 (May 14, 1990), pp. 2418–2421. DOI: 10.1103/PhysRevLett.64.2418.

[66] C. Schneider, D. Porras, and T. Schaetz. "Experimental Quantum Simulations of Many-Body Physics with Trapped Ions". In: *Rep. Prog. Phys.* 75.2 (2012), p. 024401. DOI: 10.1088/0034-4885/75/2/024401.

[67] E. Shahmoon and G. Kurizki. "Nonradiative Interaction and Entanglement between Distant Atoms". In: *Phys. Rev. A* 87.3 (Mar. 25, 2013), p. 033831. DOI: 10.1103/PhysRevA.87.033831.

[68] H. Ritsch et al. "Cold Atoms in Cavity-Generated Dynamical Optical Potentials". In: *Rev. Mod. Phys.* 85.2 (Apr. 2, 2013), pp. 553–601. DOI: 10.1103/RevModPhys.85.553.

[69] Y. Tang et al. "Thermalization near Integrability in a Dipolar Quantum Newton's Cradle". In: *Phys. Rev. X* 8.2 (May 2, 2018), p. 021030. DOI: 10.1103/PhysRevX.8.021030.

[70] J. S. Douglas et al. "Quantum Many-Body Models with Cold Atoms Coupled to Photonic Crystals". In: *Nature Photonics* 9.5 (May 2015), pp. 326–331. DOI: 10.1038/nphoton.2015.57.

[71] N. Henkel, R. Nath, and T. Pohl. "Three-Dimensional Roton Excitations and Supersolid Formation in Rydberg-Excited Bose-Einstein Condensates". In: *Phys. Rev. Lett.* 104.19 (May 11, 2010), p. 195302. DOI: 10.1103/PhysRevLett.104.195302.

[72] G. Pupillo et al. "Strongly Correlated Gases of Rydberg-Dressed Atoms: Quantum and Classical Dynamics". In: *Phys. Rev. Lett.* 104.22 (June 1, 2010), p. 223002. DOI: 10.1103/PhysRevLett.104.223002.

[73] J. E. Johnson and S. L. Rolston. "Interactions between Rydberg-Dressed Atoms". In: *Phys. Rev. A* 82.3 (Sept. 14, 2010), p. 033412. DOI: 10.1103/PhysRevA.82.033412.

[74] Y.-Y. Jau et al. "Entangling atomic spins with a Rydberg-dressed spin-flip blockade". In: *Nature Physics* 12.1 (Jan. 2016), pp. 71–74. DOI: 10.1038/nphys3487.

[75] J. Zeiher et al. "Many-Body Interferometry of a Rydberg-Dressed Spin Lattice". In: *Nature Physics* 12.12 (Dec. 2016), pp. 1095–1099. DOI: 10.1038/nphys3835.

[76] M. A. Baranov. "Theoretical Progress in Many-Body Physics with Ultracold Dipolar Gases". In: *Physics Reports* 464.3 (Aug. 1, 2008), pp. 71–111. DOI: 10.1016/j.physrep.2008.04.007.

[77] M. A. Baranov et al. "Condensed Matter Theory of Dipolar Quantum Gases". In: *Chem. Rev.* 112.9 (Sept. 12, 2012), pp. 5012–5061. DOI: 10.1021/cr2003568.

[78] D. H. J. O'Dell, S. Giovanazzi, and G. Kurizki. "Rotons in Gaseous Bose-Einstein Condensates Irradiated by a Laser". In: *Phys. Rev. Lett.* 90.11 (Mar. 17, 2003), p. 110402. DOI: 10.1103/PhysRevLett.90.110402.

[79] L. Santos, G. V. Shlyapnikov, and M. Lewenstein. "Roton-Maxon Spectrum and Stability of Trapped Dipolar Bose-Einstein Condensates". In: *Phys. Rev. Lett.* 90.25 (June 27, 2003), p. 250403. DOI: 10.1103/PhysRevLett.90.250403.

[80] D. Baillie et al. "Self-Bound Dipolar Droplet: A Localized Matter Wave in Free Space". In: *Phys. Rev. A* 94.2 (Aug. 11, 2016), 021602(R). DOI: 10.1103/PhysRevA.94.021602.

[81] D. Baillie, R. M. Wilson, and P. B. Blakie. "Collective Excitations of Self-Bound Droplets of a Dipolar Quantum Fluid". In: *Phys. Rev. Lett.* 119.25 (Dec. 22, 2017), p. 255302. DOI: 10.1103/PhysRevLett.119.255302.

[82] K.-T. Xi and H. Saito. "Droplet Formation in a Bose-Einstein Condensate with Strong Dipole-Dipole Interaction". In: *Phys. Rev. A* 93.1 (Jan. 15, 2016), p. 011604. DOI: 10.1103/PhysRevA.93.011604.

[83] B. Capogrosso-Sansone et al. "Quantum Phases of Cold Polar Molecules in 2D Optical Lattices". In: *Phys. Rev. Lett.* 104.12 (Mar. 25, 2010), p. 125301. DOI: 10.1103/PhysRevLett.104.125301.

[84] L. Pollet et al. "Supersolid Phase with Cold Polar Molecules on a Triangular Lattice". In: *Phys. Rev. Lett.* 104.12 (Mar. 25, 2010), p. 125302. DOI: 10.1103/PhysRevLett.104.125302.

[85] C. Trefzger et al. "Ultracold Dipolar Gases in Optical Lattices". In: *J. Phys. B: At. Mol. Opt. Phys.* 44.19 (2011), p. 193001. DOI: 10.1088/0953-4075/44/19/193001.

[86] N. Henkel et al. "Supersolid Vortex Crystals in Rydberg-Dressed Bose-Einstein Condensates". In: *Phys. Rev. Lett.* 108.26 (June 26, 2012), p. 265301. DOI: 10.1103/PhysRevLett.108.265301.

[87] F. Cinti et al. "Supersolid Droplet Crystal in a Dipole-Blockaded Gas". In: *Phys. Rev. Lett.* 105.13 (Sept. 21, 2010), p. 135301. DOI: 10.1103/PhysRevLett.105.135301.

[88] F. Cinti et al. "Defect-Induced Supersolidity with Soft-Core Bosons". In: *Nature Communications* 5 (Feb. 4, 2014), p. 3235. DOI: 10.1038/ncomms4235.

[89] M. Boninsegni and N. Prokof'ev. "Supersolid Phase of Hard-Core Bosons on a Triangular Lattice". In: *Phys. Rev. Lett.* 95.23 (Nov. 28, 2005), p. 237204. DOI: 10.1103/PhysRevLett.95.237204.

[90] J.-R. Li et al. "A Stripe Phase with Supersolid Properties in Spin–Orbit-Coupled Bose–Einstein Condensates". In: *Nature* 543.7643 (Mar. 2017), pp. 91–94. DOI: 10.1038/nature21431.

[91] A. Morales et al. "Coupling Two Order Parameters in a Quantum Gas". In: (Nov. 21, 2017). arXiv: 1711.07988 [cond-mat, physics:quant-ph].

[92] L. Tanzi et al. "Supersolid Symmetry Breaking from Compressional Oscillations in a Dipolar Quantum Gas". In: *Nature* 574.7778 (Oct. 2019), pp. 382–385. DOI: 10.1038/s41586-019-1568-6.

[93] L. Chomaz et al. "Long-Lived and Transient Supersolid Behaviors in Dipolar Quantum Gases". In: *Phys. Rev. X* 9.2 (Apr. 19, 2019), p. 021012. DOI: 10.1103/PhysRevX.9.021012.

[94] F. Böttcher et al. "Transient Supersolid Properties in an Array of Dipolar Quantum Droplets". In: *Phys. Rev. X* 9.1 (Mar. 22, 2019), p. 011051. DOI: 10.1103/PhysRevX.9.011051.

[95] A. Campa et al. *Physics of Long-Range Interacting Systems*. Oxford, New York: Oxford University Press, Aug. 28, 2014. 432 pp.

[96] M. Kastner. "Nonequivalence of Ensembles for Long-Range Quantum Spin Systems in Optical Lattices". In: *Phys. Rev. Lett.* 104.24 (June 16, 2010), p. 240403. DOI: 10.1103/PhysRevLett.104.240403.

[97] M. Kastner. "Diverging Equilibration Times in Long-Range Quantum Spin Models". In: *Phys. Rev. Lett.* 106.13 (Mar. 29, 2011), p. 130601. DOI: 10.1103/PhysRevLett.106.130601.

[98] Y. Tang et al. "Tuning the Dipole-Dipole Interaction in a Quantum Gas with a Rotating Magnetic Field". In: *Phys. Rev. Lett.* 120.23 (June 4, 2018), p. 230401. DOI: 10.1103/PhysRevLett.120.230401.

[99] C. Menotti, C. Trefzger, and M. Lewenstein. "Metastable States of a Gas of Dipolar Bosons in a 2D Optical Lattice". In: *Phys. Rev. Lett.* 98.23 (June 6, 2007), p. 235301. DOI: 10.1103/PhysRevLett.98.235301.

[100] C. Trefzger, C. Menotti, and M. Lewenstein. "Ultracold Dipolar Gas in an Optical Lattice: The Fate of Metastable States". In: *Phys. Rev. A* 78.4 (Oct. 7, 2008), p. 043604. DOI: 10.1103/PhysRevA.78.043604.

[101] P. Bak and R. Bruinsma. "One-Dimensional Ising Model and the Complete Devil's Staircase". In: *Phys. Rev. Lett.* 49.4 (July 26, 1982), pp. 249–251. DOI: 10.1103/PhysRevLett.49.249.

[102] F. J. Burnell et al. "Devil's Staircases and Supersolids in a One-Dimensional Dipolar Bose Gas". In: *Phys. Rev. B* 80.17 (Nov. 19, 2009), p. 174519. DOI: 10.1103/PhysRevB.80.174519.

[103] Y. Li et al. "Superstripes and the Excitation Spectrum of a Spin-Orbit-Coupled Bose-Einstein Condensate". In: *Phys. Rev. Lett.* 110.23 (June 7, 2013), p. 235302. DOI: 10.1103/PhysRevLett.110.235302.

[104] W. Cong-Jun, I. Mondragon-Shem, and Z. Xiang-Fa. "Unconventional Bose—Einstein Condensations from Spin-Orbit Coupling". In: *Chinese Phys. Lett.* 28.9 (2011), p. 097102. DOI: 10.1088/0256-307X/28/9/097102.

[105] T.-L. Ho and S. Zhang. "Bose-Einstein Condensates with Spin-Orbit Interaction". In: *Phys. Rev. Lett.* 107.15 (Oct. 6, 2011), p. 150403. DOI: 10.1103/PhysRevLett.107.150403.

[106] C. Wang et al. "Spin-Orbit Coupled Spinor Bose-Einstein Condensates". In: *Phys. Rev. Lett.* 105.16 (Oct. 13, 2010), p. 160403. DOI: 10.1103/PhysRevLett.105.160403.

[107] H. Kadau et al. "Observing the Rosensweig Instability of a Quantum Ferrofluid". In: *Nature* 530.7589 (Feb. 2016), pp. 194–197. DOI: 10.1038/nature16485.

[108] I. Ferrier-Barbut et al. "Observation of Quantum Droplets in a Strongly Dipolar Bose Gas". In: *Phys. Rev. Lett.* 116.21 (May 23, 2016), p. 215301. DOI: 10.1103/PhysRevLett.116.215301.

[109] L. Chomaz et al. "Quantum-Fluctuation-Driven Crossover from a Dilute Bose-Einstein Condensate to a Macrodroplet in a Dipolar Quantum Fluid". In: *Phys. Rev. X* 6.4 (Nov. 22, 2016), p. 041039. DOI: 10.1103/PhysRevX.6.041039.

[110] F. Wächtler and L. Santos. "Quantum Filaments in Dipolar Bose-Einstein Condensates". In: *Phys. Rev. A* 93.6 (June 24, 2016), 061603(R). DOI: 10.1103/PhysRevA.93.061603.

[111] B. M. Mladek et al. "Formation of Polymorphic Cluster Phases for a Class of Models of Purely Repulsive Soft Spheres". In: *Phys. Rev. Lett.* 96.4 (Jan. 30, 2006), p. 045701. DOI: 10.1103/PhysRevLett.96.045701.

[112] D. A. Lenz et al. "Microscopically Resolved Simulations Prove the Existence of Soft Cluster Crystals". In: *Phys. Rev. Lett.* 109.22 (Nov. 27, 2012), p. 228301. DOI: 10.1103/PhysRevLett.109.228301.

[113] F. Sciortino and E. Zaccarelli. "Computational Materials Science: Soft Heaps and Clumpy Crystals". In: *Nature* 493.7430 (Jan. 2013), pp. 30–31. DOI: 10.1038/493030a.

[114] J. Honer et al. “Collective Many-Body Interaction in Rydberg Dressed Atoms”. In: *Phys. Rev. Lett.* 105.16 (Oct. 15, 2010), p. 160404. DOI: 10.1103/PhysRevLett.105.160404.

[115] M. Mattioli et al. “Cluster Luttinger Liquids of Rydberg-Dressed Atoms in Optical Lattices”. In: *Phys. Rev. Lett.* 111.16 (Oct. 16, 2013), p. 165302. DOI: 10.1103/PhysRevLett.111.165302.

[116] M. Dalmonte et al. “Cluster Luttinger Liquids and Emergent Supersymmetric Conformal Critical Points in the One-Dimensional Soft-Shoulder Hubbard Model”. In: *Phys. Rev. B* 92.4 (July 7, 2015), p. 045106. DOI: 10.1103/PhysRevB.92.045106.

[117] N. D. Mermin and H. Wagner. “Absence of Ferromagnetism or Antiferromagnetism in One- or Two-Dimensional Isotropic Heisenberg Models”. In: *Phys. Rev. Lett.* 17.22 (Nov. 28, 1966), pp. 1133–1136. DOI: 10.1103/PhysRevLett.17.1133.

[118] A. Gelfert and W. Nolting. “The Absence of Finite-Temperature Phase Transitions in Low-Dimensional Many-Body Models: A Survey and New Results”. In: *J. Phys.: Condens. Matter* 13.27 (June 22, 2001), R505. DOI: 10.1088/0953-8984/13/27/201.

[119] A. W. Glaetzle et al. “Designing Frustrated Quantum Magnets with Laser-Dressed Rydberg Atoms”. In: *Phys. Rev. Lett.* 114.17 (Apr. 28, 2015), p. 173002. DOI: 10.1103/PhysRevLett.114.173002.

[120] R. M. W. van Bijnen and T. Pohl. “Quantum Magnetism and Topological Ordering via Rydberg Dressing near Förster Resonances”. In: *Phys. Rev. Lett.* 114.24 (June 17, 2015), p. 243002. DOI: 10.1103/PhysRevLett.114.243002.

[121] H. Schempp et al. “Correlated Exciton Transport in Rydberg-Dressed-Atom Spin Chains”. In: *Phys. Rev. Lett.* 115.9 (Aug. 26, 2015), p. 093002. DOI: 10.1103/PhysRevLett.115.093002.

[122] T. Boulier et al. "Spontaneous Avalanche Dephasing in Large Rydberg Ensembles". In: *Phys. Rev. A* 96.5 (Nov. 13, 2017), p. 053409. DOI: 10.1103/PhysRevA.96.053409.

[123] R. Nandkishore and D. A. Huse. "Many-Body Localization and Thermalization in Quantum Statistical Mechanics". In: *Annual Review of Condensed Matter Physics* 6.1 (2015), pp. 15–38. DOI: 10.1146/annurev-conmatphys-031214-014726.

[124] X.-L. Qi and S.-C. Zhang. "The Quantum Spin Hall Effect and Topological Insulators". In: *Physics Today* 63.1 (Dec. 31, 2009), pp. 33–38. DOI: 10.1063/1.3293411.

[125] S. F. Edwards and P. W. Anderson. "Theory of Spin Glasses". In: *J. Phys. F: Met. Phys.* 5.5 (May 1975), pp. 965–974. DOI: 10.1088/0305-4608/5/5/017.

[126] K. Binder and A. P. Young. "Spin Glasses: Experimental Facts, Theoretical Concepts, and Open Questions". In: *Rev. Mod. Phys.* 58.4 (Oct. 1, 1986), pp. 801–976. DOI: 10.1103/RevModPhys.58.801.

[127] H. Bernien et al. "Probing Many-Body Dynamics on a 51-Atom Quantum Simulator". In: *Nature* 551.7682 (Nov. 2017), pp. 579–584. DOI: 10.1038/nature24622.

[128] S. de Léséleuc et al. "Experimental Realization of a Symmetry Protected Topological Phase of Interacting Bosons with Rydberg Atoms". In: *Science* 365.6455 (Aug. 23, 2019), pp. 775–780. DOI: 10.1126/science.aav9105. arXiv: 1810.13286.

[129] R. Díaz-Méndez et al. "Monodisperse Cluster Crystals: Classical and Quantum Dynamics". In: *Phys. Rev. E* 92.5 (Nov. 9, 2015), p. 052307. DOI: 10.1103/PhysRevE.92.052307.

[130] R. Díaz-Méndez et al. "Glass Transitions in Monodisperse Cluster-Forming Ensembles: Vortex Matter in Type-1.5 Superconductors". In: *Phys. Rev. Lett.* 118.6 (Feb. 8, 2017), p. 067001. DOI: 10.1103/PhysRevLett.118.067001.

[131] R. Díaz-Méndez et al. “Phase-Change Switching in 2D via Soft Interactions”. In: *Soft Matter* 15.3 (Jan. 16, 2019), pp. 355–358. DOI: 10.1039/C8SM01738G.

[132] M. Motta et al. “Dynamical Structure Factor of One-Dimensional Hard Rods”. In: *Phys. Rev. A* 94.4 (Oct. 13, 2016), p. 043627. DOI: 10.1103/PhysRevA.94.043627.

[133] M. Teruzzi, D. E. Galli, and G. Bertaina. “Microscopic Study of Static and Dynamical Properties of Dilute One-Dimensional Soft Bosons”. In: *J Low Temp Phys* 187.5 (June 1, 2017), pp. 719–726. DOI: 10.1007/s10909-016-1736-0.

[134] G. Schmid et al. “Finite-Temperature Phase Diagram of Hard-Core Bosons in Two Dimensions”. In: *Phys. Rev. Lett.* 88.16 (Apr. 9, 2002), p. 167208. DOI: 10.1103/PhysRevLett.88.167208.

[135] F. Hébert et al. “Quantum Phase Transitions in the Two-Dimensional Hardcore Boson Model”. In: *Phys. Rev. B* 65.1 (Dec. 5, 2001), p. 014513. DOI: 10.1103/PhysRevB.65.014513.

[136] K. H. Fischer and J. A. Hertz. *Spin Glasses by K. H. Fischer*. May 1991. DOI: 10.1017/CBO9780511628771. URL: /core/books/spin-glasses/8513DA3DC0EE8370FF6E0AC5248825DF (visited on 10/13/2019).

[137] G. Carleo, M. Tarzia, and F. Zamponi. “Bose-Einstein Condensation in Quantum Glasses”. In: *Phys. Rev. Lett.* 103.21 (Nov. 18, 2009), p. 215302. DOI: 10.1103/PhysRevLett.103.215302.

[138] D. Ruelle. “Classical Statistical Mechanics of a System Af Particles”. In: *Helvetica Physica Acta* 36 (1963), p. 183.

[139] T. Dauxois et al. “Dynamics and Thermodynamics of Systems with Long-Range Interactions: An Introduction”. In: *Dynamics and Thermodynamics of Systems with Long-Range Interactions*. Ed. by T. Dauxois et al. Lecture Notes in Physics. Berlin, Heidelberg: Springer Berlin Heidelberg, 2002, pp. 1–19. DOI: 10.1007/3-540-45835-2_1.

[140] D. Mukamel. "Statistical Mechanics of Systems with Long Range Interactions". In: *AIP Conference Proceedings* 970.1 (Jan. 11, 2008), pp. 22–38. DOI: 10.1063/1.2839123.

[141] J. Barré, D. Mukamel, and S. Ruffo. "Inequivalence of Ensembles in a System with Long-Range Interactions". In: *Phys. Rev. Lett.* 87.3 (June 29, 2001), p. 030601. DOI: 10.1103/PhysRevLett.87.030601.

[142] A. Campa, T. Dauxois, and S. Ruffo. "Statistical Mechanics and Dynamics of Solvable Models with Long-Range Interactions". In: *Physics Reports* 480.3 (Sept. 1, 2009), pp. 57–159. DOI: 10.1016/j.physrep.2009.07.001.

[143] Y. Levin et al. "Nonequilibrium Statistical Mechanics of Systems with Long-Range Interactions". In: *Physics Reports*. Nonequilibrium Statistical Mechanics of Systems with Long-Range Interactions 535.1 (Feb. 1, 2014), pp. 1–60. DOI: 10.1016/j.physrep.2013.10.001.

[144] H. J. Schulz. "Wigner Crystal in One Dimension". In: *Phys. Rev. Lett.* 71.12 (Sept. 20, 1993), pp. 1864–1867. DOI: 10.1103/PhysRevLett.71.1864.

[145] D. W. Wang, A. J. Millis, and S. Das Sarma. "Coulomb Luttinger Liquid". In: *Phys. Rev. B* 64.19 (Oct. 15, 2001), p. 193307. DOI: 10.1103/PhysRevB.64.193307.

[146] G. Fano et al. "Unscreened Coulomb Repulsion in the One-Dimensional Electron Gas". In: *Phys. Rev. B* 60.23 (Dec. 15, 1999), pp. 15654–15659. DOI: 10.1103/PhysRevB.60.15654.

[147] M. Casula, S. Sorella, and G. Senatore. "Ground State Properties of the One-Dimensional Coulomb Gas Using the Lattice Regularized Diffusion Monte Carlo Method". In: *Phys. Rev. B* 74.24 (Dec. 22, 2006), p. 245427. DOI: 10.1103/PhysRevB.74.245427.

[148] G. E. Astrakharchik and M. D. Girardeau. "Exact Ground-State Properties of a One-Dimensional Coulomb Gas". In: *Phys. Rev. B* 83.15 (Apr. 15, 2011), p. 153303. DOI: 10.1103/PhysRevB.83.153303.

[149] R. M. Lee and N. D. Drummond. "Ground-state properties of the one-dimensional electron liquid". In: *Phys. Rev. B* 83.24 (June 22, 2011), p. 245114. DOI: 10.1103/PhysRevB.83.245114.

[150] D. Poilblanc et al. "Insulator-Metal Transition in One Dimension Induced by Long-Range Electronic Interactions". In: *Phys. Rev. B* 56.4 (July 15, 1997), R1645–R1649. DOI: 10.1103/PhysRevB.56.R1645.

[151] B. Valenzuela, S. Fratini, and D. Baeriswyl. "Charge and Spin Order in One-Dimensional Electron Systems with Long-Range Coulomb Interactions". In: *Phys. Rev. B* 68.4 (July 29, 2003), p. 045112. DOI: 10.1103/PhysRevB.68.045112.

[152] Z.-H. Li. "Ground States of Long-Range Interacting Fermions in One Spatial Dimension". In: *J. Phys.: Condens. Matter* 31.25 (Apr. 2019), p. 255601. DOI: 10.1088/1361-648X/ab0fcf.

[153] S. A. Cannas and F. A. Tamarit. "Long-Range Interactions and Nonextensivity in Ferromagnetic Spin Models". In: *Phys. Rev. B* 54.18 (Nov. 1, 1996), R12661–R12664. DOI: 10.1103/PhysRevB.54.R12661.

[154] F. Tamarit and C. Anteneodo. "Rotators with Long-Range Interactions: Connection with the Mean-Field Approximation". In: *Phys. Rev. Lett.* 84.2 (Jan. 10, 2000), pp. 208–211. DOI: 10.1103/PhysRevLett.84.208.

[155] T. Dauxois et al. "The Hamiltonian Mean Field Model: From Dynamics to Statistical Mechanics and Back". In: *Dynamics and Thermodynamics of Systems with Long-Range Interactions*. Ed. by T. Dauxois et al. Lecture Notes in Physics. Berlin, Heidelberg: Springer Berlin Heidelberg, 2002, pp. 458–487. DOI: 10.1007/3-540-45835-2_16.

[156] A. Campa, A. Giansanti, and D. Moroni. "Canonical Solution of Classical Magnetic Models with Long-Range Couplings". In: *J. Phys. A: Math. Gen.* 36.25 (June 2003), pp. 6897–6921. DOI: 10.1088/0305-4470/36/25/301.

[157] M. Kastner and O. Schnetz. "On the Mean-Field Spherical Model". In: *J Stat Phys* 122.6 (Mar. 1, 2006), pp. 1195–1214. DOI: 10.1007/s10955-005-8031-9.

[158] C. Anteneodo and C. Tsallis. "Breakdown of Exponential Sensitivity to Initial Conditions: Role of the Range of Interactions". In: *Phys. Rev. Lett.* 80.24 (June 15, 1998), pp. 5313–5316. DOI: 10.1103/PhysRevLett.80.5313.

[159] C. Anteneodo. "Nonextensive Scaling in a Long-Range Hamiltonian System". In: *Physica A: Statistical Mechanics and its Applications*. Proceedings of the VIII Latin American Workshop on Nonlinear Phenomena 342.1 (Oct. 15, 2004), pp. 112–118. DOI: 10.1016/j.physa.2004.04.066.

[160] T. Holstein and H. Primakoff. "Field Dependence of the Intrinsic Domain Magnetization of a Ferromagnet". In: *Phys. Rev.* 58.12 (Dec. 15, 1940), pp. 1098–1113. DOI: 10.1103/PhysRev.58.1098.

[161] B. Fauseweh, J. Stolze, and G. S. Uhrig. "Finite-Temperature Line Shapes of Hard-Core Bosons in Quantum Magnets: A Diagrammatic Approach Tested in One Dimension". In: *Phys. Rev. B* 90.2 (July 28, 2014), p. 024428. DOI: 10.1103/PhysRevB.90.024428.

[162] In: *mbox{ITensor Library}* (*version 2.0.11*) *http://itensor.org* ().

[163] T. Giamarchi. *Quantum Physics in One Dimension*. Oxford University Press, Dec. 18, 2003.

[164] P. Schmitteckert and R. Werner. "Charge-Density-Wave Instabilities Driven by Multiple Umklapp Scattering". In: *Phys. Rev. B* 69.19 (May 28, 2004), p. 195115. DOI: 10.1103/PhysRevB.69.195115.

[165] F. Franchini. *An Introduction to Integrable Techniques for One-Dimensional Quantum Systems*. Lecture Notes in Physics. Springer International Publishing, 2017.

[166] M. A. Cazalilla. "Bosonizing One-Dimensional Cold Atomic Gases". In: *J. Phys. B: At. Mol. Opt. Phys.* 37.7 (Mar. 2004), S1–S47. DOI: 10.1088/0953-4075/37/7/051.

[167] W. Kohn. "Theory of the Insulating State". In: *Phys. Rev.* 133 (1A Jan. 6, 1964), A171–A181. DOI: 10.1103/PhysRev.133.A171.

[168] I. S. Tupitsyn and N. V. Prokof'ev. "Stability of Dirac Liquids with Strong Coulomb Interaction". In: *Phys. Rev. Lett.* 118.2 (Jan. 12, 2017), p. 026403. DOI: 10.1103/PhysRevLett.118.026403.

[169] S. Schütz and G. Morigi. "Prethermalization of Atoms Due to Photon-Mediated Long-Range Interactions". In: *Phys. Rev. Lett.* 113.20 (Nov. 14, 2014), p. 203002. DOI: 10.1103/PhysRevLett.113.203002.

[170] J. G. Kemeny and J. L. Snell. *Finite Markov Chains: With a New Appendix "Generalization of a Fundamental Matrix"*. Undergraduate Texts in Mathematics. New York: Springer-Verlag, 1976.

[171] N. Metropolis et al. "Equation of State Calculations by Fast Computing Machines". In: *The Journal of Chemical Physics* 21.6 (June 1, 1953), pp. 1087–1092. DOI: 10.1063/1.1699114.

[172] W. K. Hastings. "Monte Carlo Sampling Methods Using Markov Chains and Their Applications". In: *Biometrika* 57.1 (Apr. 1, 1970), pp. 97–109. DOI: 10.1093/biomet/57.1.97.

[173] G. G. Batrouni et al. "Dynamic Response of Trapped Ultracold Bosons on Optical Lattices". In: *Phys. Rev. A* 72.3 (Sept. 14, 2005), p. 031601. DOI: 10.1103/PhysRevA.72.031601.

[174] T. F. Gallagher. *Rydberg Atoms*. Sept. 1994. DOI: 10.1017/CBO9780511524530.

[175] D. Comparat and P. Pillet. "Dipole Blockade in a Cold Rydberg Atomic Sample [Invited]". In: *J. Opt. Soc. Am. B, JOSAB* 27.6 (June 1, 2010), A208–A232. DOI: 10.1364/JOSAB.27.00A208.

[176] R. Faoro et al. "Van Der Waals Explosion of Cold Rydberg Clusters". In: *Phys. Rev. A* 93.3 (Mar. 14, 2016), p. 030701. DOI: 10.1103/PhysRevA.93.030701.

[177] H. Weimer et al. "Digital Quantum Simulation with Rydberg Atoms". In: *Quantum Inf Process* 10.6 (Sept. 24, 2011), p. 885. DOI: 10.1007/s11128-011-0303-5.

[178] S. Whitlock, A. W. Glaetzle, and P. Hannaford. "Simulating Quantum Spin Models Using Rydberg-Excited Atomic Ensembles in Magnetic Microtrap Arrays". In: *J. Phys. B: At. Mol. Opt. Phys.* 50.7 (Mar. 2017), p. 074001. DOI: 10.1088/1361-6455/aa6149.

[179] S. Helmrich et al. "Signatures of Self-Organised Criticality in an Ultracold Atomic Gas". In: (Feb. 27, 2019). arXiv: 1806.09931 [cond-mat, physics:physics, physics:quant-ph].

[180] T. M. Wintermantel et al. "Unitary and Non-Unitary Quantum Cellular Automata with Rydberg Arrays". In: (Sept. 23, 2019). arXiv: 1909.10193 [cond-mat, physics:physics, physics:quant-ph].

[181] D. Jaksch et al. "Fast Quantum Gates for Neutral Atoms". In: *Phys. Rev. Lett.* 85.10 (Sept. 4, 2000), pp. 2208–2211. DOI: 10.1103/PhysRevLett.85.2208.

[182] M. D. Lukin et al. "Dipole Blockade and Quantum Information Processing in Mesoscopic Atomic Ensembles". In: *Phys. Rev. Lett.* 87.3 (June 26, 2001), p. 037901. DOI: 10.1103/PhysRevLett.87.037901.

[183] D. Tong et al. "Local Blockade of Rydberg Excitation in an Ultracold Gas". In: *Phys. Rev. Lett.* 93.6 (Aug. 3, 2004), p. 063001. DOI: 10.1103/PhysRevLett.93.063001.

[184] K. Singer et al. "Suppression of Excitation and Spectral Broadening Induced by Interactions in a Cold Gas of Rydberg Atoms". In: *Phys. Rev. Lett.* 93.16 (Oct. 13, 2004), p. 163001. DOI: 10.1103/PhysRevLett.93.163001.